

Formulation and Characterization of the Metal-Organic Compound UiO-66

*Master's thesis in Materials Science and
Nanotechnology*

Daniel Wolseop Lee



Department of Chemistry and Department of Physics

Faculty of Mathematics and Natural Sciences

University of Oslo

2016

Acknowledgements

This thesis is a result of experimental work performed at the Department of Chemistry, University of Oslo and at SINTEF Materials and Chemistry in Oslo from August 2014 to July 2016 under the supervision of Professor Unni Olsbye and Senior Research Scientist Carlos Adolfo Grande. I would like to express my gratitude to both my supervisors for offering an interesting topic. Also, I would like to thank all members of the catalysis group and people who helped me in the laboratories in SINTEF for providing new ideas and a friendly learning environment.

Table of Contents

Acknowledgements	2
Abbreviations	6
Abstract	8
Scope	9
1. Introduction	10
1.1. Metal-Organic Frameworks	10
1.1.1. Definition	10
1.1.2. Historical Background.....	10
1.1.3. Designing the MOFs	13
1.1.4. Drawbacks	14
1.1.5. Zr-based MOFs	15
1.1.6. Application	17
1.2. Formulation	18
1.2.1. Previous Work.....	18
1.2.2. Encapsulation	19
1.2.3. Alginate properties	19
1.2.4. Ergun Equation and Pressure Drop	23
1.2.5. Varying the Size of Beads	24
2. Experimental Methods	26
2.1. Formulation	26
2.1.1. Reagents Used in this work.....	26
2.1.2. Method	28
2.1.3. Gelation	30
2.1.4. Washing.....	30
2.1.5. Drying.....	31
2.1.6. Activation	31
2.2. Compression Test.....	32
2.3. Powder X-ray Diffraction.....	33
2.3.1. Basic Description of the Technique	33
2.3.2. Purpose of Usage in this Thesis	35

2.3.3. Experimental Methods	35
2.4. Analysis of adsorption/desorption isotherms	36
2.4.1. Nitrogen Adsorption Isotherms	37
2.4.2. CO ₂ Sorption Measurements	44
2.5. Thermogravimetric Analysis – Differential Scanning Calorimetry (TGA-DSC).....	45
2.5.1. Basic Description of the Technique	45
2.5.2. Purpose of Usage in this Thesis	46
2.5.3. Measurement Method.....	46
2.6. Scanning Electron Microscopy	47
2.6.1. Basic Description of the Technique	47
2.6.2. Measurement Method.....	49
2.6.3. Elemental Analysis (<i>via</i> Energy Dispersive X-ray Spectroscopy, EDX)	50
2.7. Fourier Transform Infrared (FTIR) Spectroscopy techniques	50
2.7.1. Basic Description of the Technique	50
2.7.2. Measurement Method.....	51
2.8. Optical microscopy	52
3. Results and Discussion.....	53
3.1. Effect of Different Types of Alginates.....	53
3.2. Effect of Alginate Concentration	59
3.3. Effect of Calcium Ion Concentration	68
3.4. Effect of Gelation Time.....	73
3.5. Effect of Activation Temperature and Time	76
3.6. Effect of Size of Beads.....	83
3.7. Effect of Multivalent Cations and pH	86
3.8. Results From The Optimally Formulated Beads.....	97
4. Conclusion.....	99
5. Suggestions for Further Work	100
6. References	101
7. Appendices	105
7.1. Detailed Synthesis of UiO-66 (SH-55)	106
7.2. Calculation of the decrease in N ₂ isotherms.....	107
7.3. Calculation of Ca:Zr ratio	107

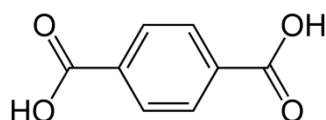
7.4. The amount of calcium ions needed in the gelation.....	108
7.5. EDX.....	110
7.5.1. EDX on samples with various washing times.....	110
7.5.2. EDX on samples with varying gelation time	118
7.6. Calculation of Isosteric Heat of Adsorption.....	125
7.7. Sample Overview	126
7.8. Viscosity Measurement of Alginates	127

Abbreviations

a.u.: Arbitrary unit

BET theory: Brunauer-Emmett-Teller Theory. Explains the physical adsorption of gas molecules (adsorptives) on a solid surface material (adsorbent).

BDC: Benzene-1,4-dicarboxylic acid (IUPAC name). Terephthalic acid (common name).



BSE: Back-scattered electron

CAS: Chemical Abstracts Service

EDX: Energy-dispersive X-ray (EDX) spectroscopy. An analytical technique used for elemental analysis or chemical characterization of a sample.

FEG: Field emission gun

FTIR: Fourier transform infrared (FTIR) spectroscopy. An analytical technique used to identify the functional groups present in a molecule

HKUST: Hong Kong University of Science and Technology.

IUPAC: International Union of Pure and Applied Chemistry

MOF: Metal-Organic Framework.

PXRD: Powder X-ray Diffraction. An analytical technique used to identify the crystalline phase of the sample.

SBU: Secondary Building Unit. Inorganic metal oxide entities inside MOFs.

SE: Secondary electron

SEM: Scanning Electron Microscopy. An analytical technique used to investigate the surface of the sample.

TGA: Thermogravimetric Analysis. An analytical technique used to observe the thermal behavior of the sample.

UiO: Universitet i Oslo (eng. university of Oslo).

Zr-MOF: MOFs involving zirconium-based SBUs

Abstract

This project is a part of a large effort in the Catalysis section at the Department of Chemistry, UiO, aimed at commercializing the UiO-66 series of metal organic framework (MOF) materials. The aim of this project was to advance the knowledge about how to formulate metal-organic framework materials without losing their single site characteristics. UiO-66, a Zr-based MOF with benzenedicarboxylic acid linkers, was used as a starting material.

UiO-66 MOF was formulated using alginates, a technique first reported by researchers at SINTEF in 2014.⁴ This technique was adapted to UiO-66 and was optimized.

Resulting formulated MOF beads were tested for crushing strength test, BET-surface area, nitrogen sorption isotherm, CO₂ uptake, PXRD and FTIR. Data obtained from formulated beads are very similar to that of unformulated powder material; the formulation did not cause noticeable damage on the MOF material.

Scope

Metal-Organic Frameworks (MOFs), a material class which has gained tremendous interest due to its properties and the ease of designing (more in Section **1.1.3**), may have interesting applications such as catalysis, gas storage, gas separation, drug delivery amongst other areas.⁵ In 2008, the catalysis section at University of Oslo published UiO-66, the first zirconium-based MOF reported, which exhibits exceptional chemical, thermal and mechanical stability compared to other known MOFs.⁶⁻⁷

The group focuses on the application of UiO-MOFs, putting its effort on up-scale and formulation of UiO-MOFs. Both UiO-66 and UiO-67 show promising results in selective separation of methane and carbon dioxide at high pressures although the statement was based on powder form of these materials.² In order for MOFs to see practical applications at industrial scale, the powder must be transformed into a solid shaped body.

The synthesis and structural studies of MOFs has been well documented. However, shaping and formulation of MOFs is far less studied although this step is crucial for its possible applications in catalysis and gas separation at an industrial scale. Processes involving fluid-bed or fixed-bed reactor or container require the transformation of fluffy powders into solid materials having small size distributions. Shaping by compression, palletization and extrusion, the conventional methods using high pressure for shaping other powder materials such as zeolites, might infringe more structural damages to most of known MOFs due to their fragile nature.⁸ These methods may cause significant reduction in porosity, surface area, chemical stability or functionality in MOFs as described briefly in Section **1.1.4.2**.

The primary aims of this work are the following:

- 1) To develop a method to formulate the materials without any significant reduction in material's properties.
- 2) To learn characterization methods and use them to characterize the unformulated / formulated material.

In depth explanations of methods used for this work can be found in **Section 1.2** and **Section 2**.

1. Introduction

1.1. Metal-Organic Frameworks

1.1.1. Definition

According to IUPAC,⁹ A metal-organic framework (MOF) is a coordination network where metal ions or metal cluster complexes bonded to organic ligands extending in 2 or 3 dimensions yielding a framework. This framework contains potential voids.

The organics ligands in MOFs are called *linkers* and metal clusters are called *secondary building units* (SBUs). **Figure 1** illustrates a hierarchical terminology used by IUPAC.

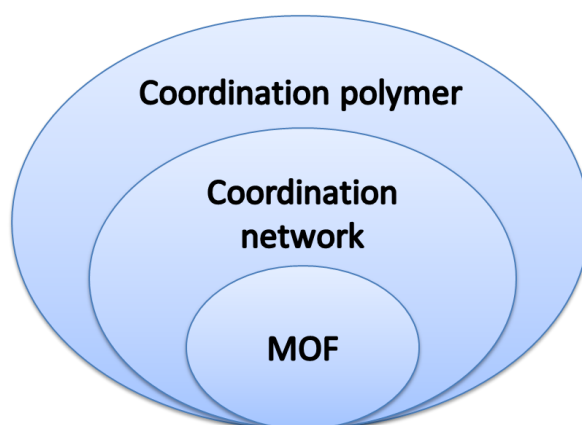


Figure 1: A hierarchical terminology. A coordination polymer is the most general term, and does not need to be crystalline whereas coordination network is a coordination compound extending, through repeating coordination entities in 1, 2 or 3 dimensions.

1.1.2. Historical Background

Chemical compounds that met the structural criteria defined by IUPAC above were known¹⁰ long before the name “metal-organic framework” appeared in the literature for the first time by Yaghi et al. in 1995.¹¹ The early MOFs such as $[\text{Cu}(\text{adiponitrile})_2] \cdot \text{NO}_3$ and $[\text{Cu}(\text{bipy})_2] \cdot \text{PF}_6$ were built up of individual metal ions (Cu^+ in this case) bridged by organic linkers with multiple neutral, mono-dentate ligating moieties. The resulting MOFs were cationic and this required non-coordinating anions (NO_3^- and PF_6^- for $[\text{Cu}(\text{adiponitrile})_2]^+$

and $[\text{Cu}(\text{bipy})_2]^+$, respectively) in the voids for charge balance. Such compounds are regarded as clathrate-type MOFs, however, which are not categorized as “porous” compounds (thus the word “potential” in the definition of MOFs).

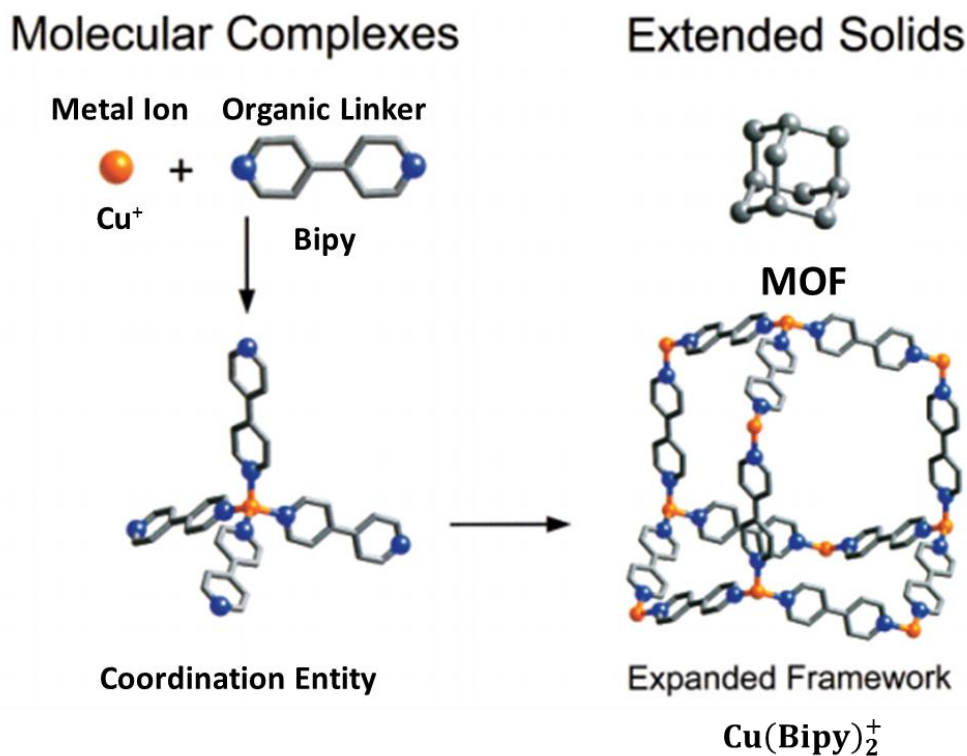


Figure 2. An example of the assembly of an early MOF. M, orange; C, grey; N, blue. All hydrogen atoms and anions (PF_6^-) have been omitted for clarity. Illustration is taken from the literature by Eddaoudi *et al.*¹²

Figure 2 illustrates the assembly of an early MOF.¹³ The copolymerization of Cu^+ ions with organic 4,4'-bipyridine linkers gives a flexible metal-bipyridine structure with expanded diamond topology. The majority of the space is empty, and this empty space in the materials is called *pores* or *voids*. In reality, these pores inside a material are occupied by guest molecules (typically charge balancing anions in the early MOFs or the solvent used in the synthesis) which must be removed in order to fully exploit the material's porosity.

Porosity means “the quality or state of being a porous entity, which has many small holes that allow water, air, and so on, to pass through.”¹⁴ Among many researchers, there has been a misconception that the materials with guest molecules in their voids are porous materials. The early MOFs were a good example. “porosity” was demonstrated by Kondo *et al.* ($\{[\text{M}_2(4,4' - \text{bpy})_3(\text{NO}_3)_4] \cdot x\text{H}_2\text{O}\}_n$, $\text{M} = \text{Co}, \text{Ni}, \text{Zn}$)¹⁵ in 1997 and Yaghi *et al.* ($\text{MOF-2}, \text{Zn}(\text{BDC})$)¹⁶ in 1998. Both materials only possess a modest porosity (calculated Langmuir

apparent surface area of $270 \text{ m}^2\text{g}^{-1}$ for MOF-2), but they were strong enough to withstand the solvent removal and activation. These materials were tested for gas sorption experiments under ambient conditions. Reversible gas storage properties were identified and the Porous Coordination Polymers (CPCs) attracted wide attention as new porous materials. The development in design and synthesis of MOF has experienced a rapid expansion since MOF-2 in 1998.

Shortly after, a new type of MOF made up of Zn_4O clusters bridged by organic BDC linkers ($\text{Zn}_4\text{O}(\text{BDC})_3$ later called MOF-5 (sometimes called IRMOF-1)) was published by Li *et al.* in 1999.¹⁷ MOF-5 showed an exceptionally high surface area (*ca.* $3,000 \text{ m}^2\text{g}^{-1}$)¹⁸, breaking the previous record holder (zeolite Y, $904 \text{ m}^2\text{g}^{-1}$)¹⁹ at that time. The discovery of MOF-5 was ground breaking as the compound was created in an entirely predictable way based upon the symmetry of its components.²⁰ This work suggested that it was possible to engineer microporous structures and tailor cavities and channels in a precise manner, resulting in a boom in MOF research.

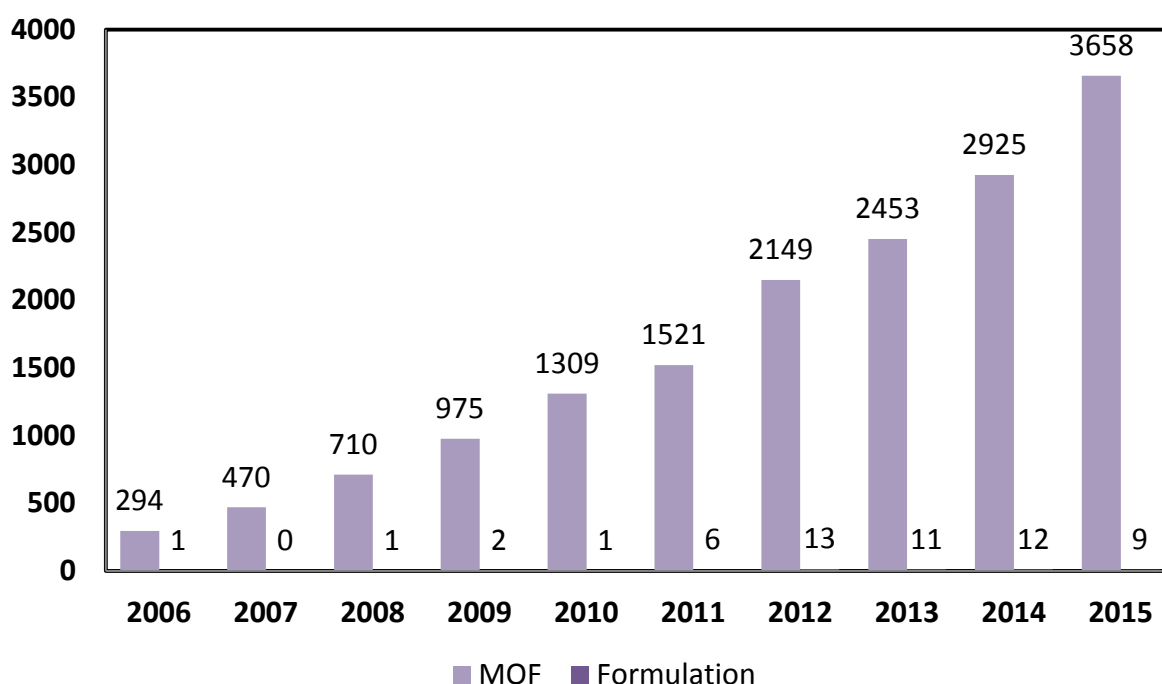


Figure 3. Number of MOF publications found using search word “Metal-organic framework” (duplicate results removed) during last 10 years according to SciFinder. Note that the numbers are approximate; the graph is meant to give an idea of how the activity in MOF research has expanded in recent years. Number of publications related to the formulation of MOF powders are also shown.

1.1.3. Designing the MOFs

MOFs differ from their inorganic counterpart, zeolites, due to their diverse structures and functionalities, by having virtually infinite number of organic linkers and various types of SBUs as their building blocks. The choice of SBUs and organic linkers can dictate the framework topology (affecting pore size and shape) and influence the overall chemical functionality of the framework^{21,22}, thus greatly affect the uptake properties and host-guest interactions within the framework.²³

On top of that, it is possible to tune the physical and chemical properties of MOFs even further by functionalizing the pores and cavities. This can be achieved either by chemically modifying the organic linkers or SBUs by incorporation of functional groups after MOFs have been synthesized. This process is called **postsynthetic modification** (PSM) which is a highly useful tool for preparing topologically identical but functionally (chemical and physical properties) diverse MOF frameworks.²⁴

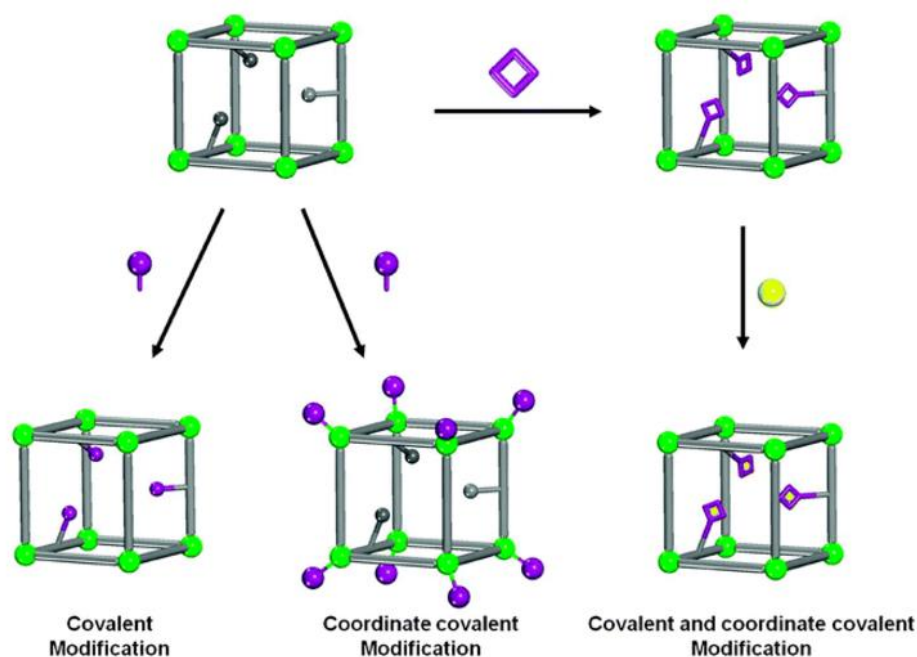


Figure 4. Simple illustration of PSM strategies. Chemical modification of linkers (left), SBUs (middle), and a combination of PSM strategies (right). Green: SBU, purple and yellow: functional groups.²⁵

1.1.4. Drawbacks

Although MOFs possess interesting physical and chemical properties, there are main challenges that MOFs have to overcome prior to any practical applications. Cost and stability issue are two main hurdles for the time being, thus will be described in more detail in this section.

1.1.4.1. Cost

Generally, MOFs are expensive due to the cost of its organic linkers. Many reported synthesis route for MOFs also include high temperature and high pressure with toxic and expensive organic solvents (direct solvothermal synthesis). The PSM methods used to improve the stability of MOFs (e.g., improved water stability of MOF-5)²⁶ decrease the microporous surface area and/or the functionality. Most of them are labor and resource expensive as well.

However, the cost issue could be solved by developing new green and cost/energy-efficient synthesis methods, and when a profitable niche market where MOFs are superior to other materials, especially zeolites, is established. Possible applications will be described in **section 1.1.6.**

1.1.4.2. Stability

Compared to zeolites that are already in industrial use, most early MOFs are less stable chemically, thermally, hydrothermally and mechanically. In recent years, it has been a significant improvement in enhancing the stability of MOFs, and there are many MOFs that are chemically and (hydro)thermally stable today^{6, 27-28}. Depending on the application envisaged, different types of stabilities are important. For instance, chemical and (hydro)thermal stabilities are important for gas separation²⁹, and catalytic processes in which high temperature, varying pH and high humidity are present³⁰. Mechanical stability is much of importance for any practical use. However, most MOFs are not suitable to bear mechanical loadings that are common in industrial processing (e.g., hydrostatic compressions in high pressure gas loading) and applications (e.g., pelletizing). MOFs that are thermally and chemically stable do not necessarily be mechanically stable; they suffer from partial pore collapse or amorphization even under modest mechanical stress³¹⁻³³.

In order for MOFs to be commercialized, all of the stability issues must be overcome. There are very few candidates to date, with zirconium (Zr(IV)) based MOFs (Zr-MOFs) being one of the most investigated MOFs (especially UiO-66 and its derivatives) due to its exceptional chemical, (hydro)thermal and mechanical stability.^{6-7, 34-36}

1.1.5. Zr-based MOFs

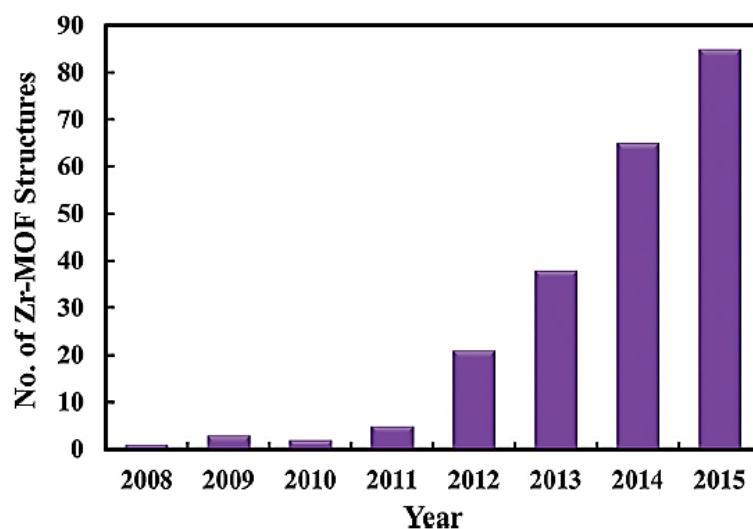


Figure 5 The year-by-year increase of reported Zr-MOFs in the last eight years (by SciFinder). The graph is copied from *Zr-based metal-organic frameworks: design, synthesis, structure, and applications*.³⁵

The weak point of MOFs typically lies in the lability of metal-linker bonds. Generally, MOFs with SBUs consisted of Zn^{2+} transition metal ions are not stable due to their d^{10} electron configuration according to the ligand field theory.³⁴ A better stability of MOFs with SBUs containing Cu^{2+} with d^9 configuration can be explained by the same theory.

The lability of MOFs can be decreased (thus increasing the chemical stability) by using high-valence metal ions given that all the coordination environments are equal to those consisted of lower-valence ones. This is a result of stronger electrostatic interaction between the metal ion and the organic linkers. In 2008, a group of researchers from University of Oslo (Universitetet i Oslo, UiO) introduced UiO-66; world's first zirconium-based MOF (Zr-MOF).⁶ The exceptional stability of Zr-MOFs is attributable to not only its high charge (Zr^{4+}), but its high charge density. UiO-66 possesses 12-coordinated SBUs. **Figure 6** shows two possible forms of SBUs of UiO-66. Zr^{4+} ions interact strongly with carboxylate ligands; making it less vulnerable to ligand substitution.³⁷ Higher degree of coordination means that

the MOFs suffer proportionally less disconnection if ligand substitution or loss of ligands was to occur. Each SBU in UiO-MOFs can interact with up to 12 ligands; highest coordination number reported so far, thus are exceptionally stable in that manner.

It should be noted, however, that the high coordination number that caused increased chemical stability of Zr-MOFs also makes it difficult to obtain high-quality single crystals for single crystal XRD (which is more precise than PXRD) purposes, producing only microcrystalline powders.³⁴ For both research and industrial application purposes, accurate characterization of properties of MOFs is essential.

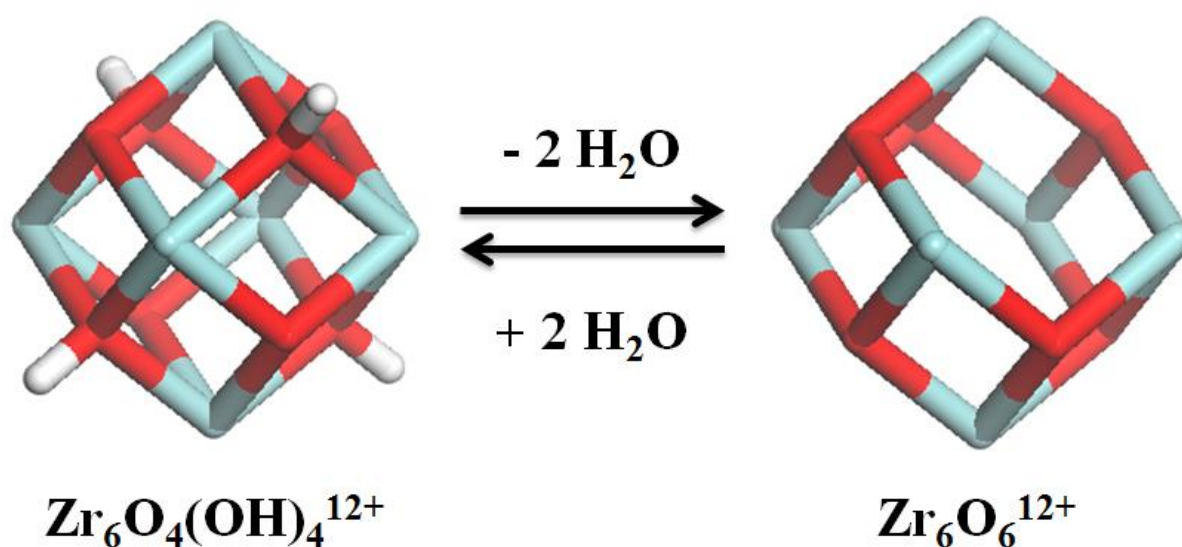


Figure 6 Dehydroxylation of SBU in UiO-MOFs. Zirconium, oxygen and hydrogen are shown in cyan, red and white, respectively.

It is known that the transition from the hydrated form into the dehydrated form takes place in the temperature range of ca. 200 – 325 °C. These two forms of UiO-66 are expected to be slightly different in the structure, thus might affect the adsorption property.³⁸

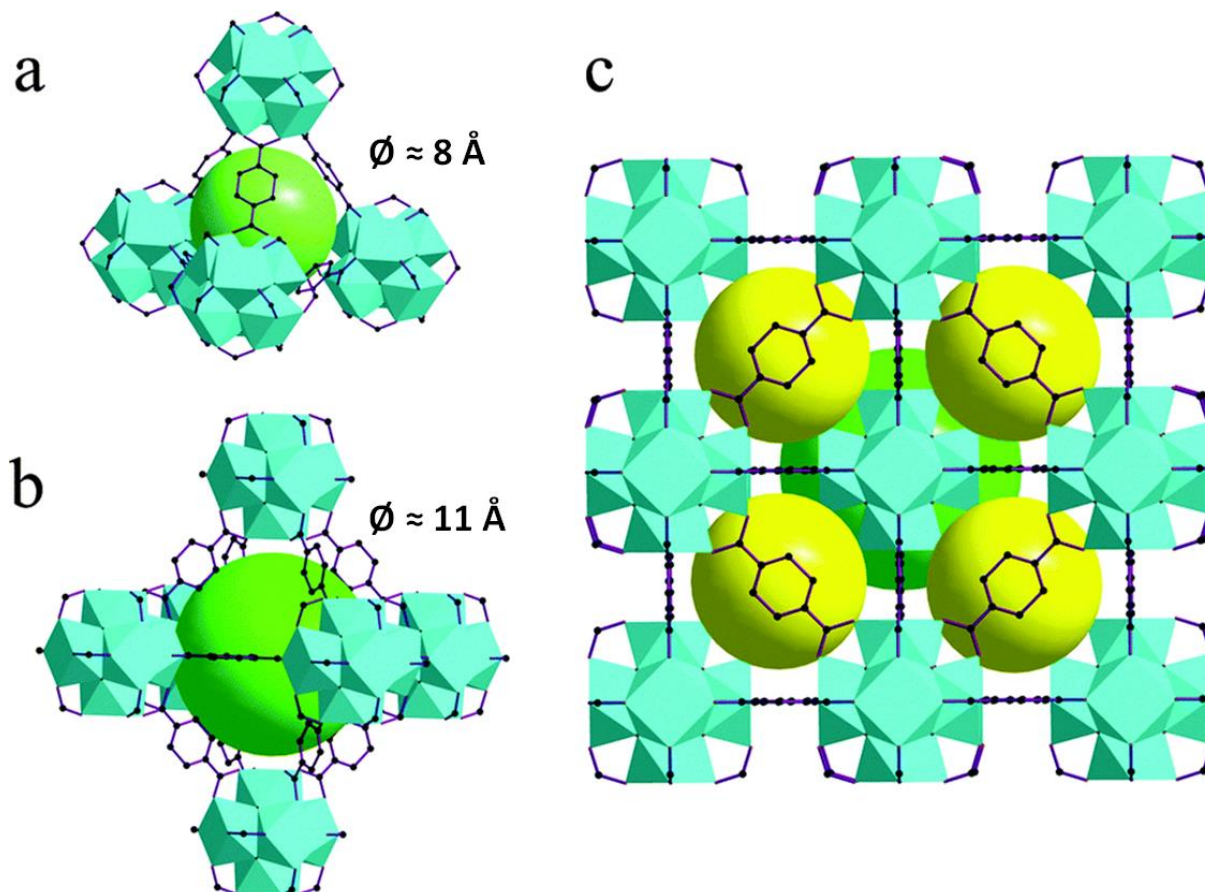


Figure 7: Illustration of the UiO-66 structure: (a) tetrahedral cavity; (b) octahedral cavity; (c) packing of the two types of cavities (tetrahedral and octahedral cavity in yellow and green, respectively). The approximate diameters for the tetrahedral cavity and the octahedral cavity are 8 Å and 11 Å, respectively. Zirconium and carbon atoms are in cyan polyhedral and blue, respectively. Hydrogens are omitted for clarity. This illustration is a modified version of the one from *Zr-based metal-organic frameworks: design, synthesis, structure, and applications*.³⁵

1.1.6. Application

Given the fact that MOFs (and its physical and chemical properties) can be easily tuned and modified as briefly described in **Section 1.1.3**, MOFs might be potentially interesting for various applications. Two most commonly proposed potential applications are gas adsorption applications such as gas storage¹⁸ and/or gas separation³⁹ due to its high porosity and surface area. Global warming is the biggest threat to living organisms on earth. Thus, there has been a lot of effort to utilize MOFs to capture carbon dioxide. MOFs that selectively adsorb CO₂ over the other components have been proposed in the literature.⁴⁰⁻⁴¹

Another potential application is to use MOFs as a catalyst. As like zeolite materials, MOFs have a highly ordered structure; they possess a narrow size distribution of

pores/cavities and channels.³⁰ Recently, Li et al. reported a strategy of combining a Brønsted acid MOF framework with Lewis acid centers to afford a Lewis acid@Brønsted acid MOF with high catalytic activity.⁴² They demonstrated that MIL-101-Cr-SO₃H·Al(III), with Al(III) as Lewis acid centers, outperformed two benchmark zeolite catalysts (H-Beta and HMOR) on the benzylation of aromatic hydrocarbons with benzyl alcohol.

However, there have not been any viable, cost-efficient and long-lasting MOFs in use at an industrial scale yet. Further development of MOFs remains as a challenging field of chemistry.

1.2. Formulation

1.2.1. Previous Work

Shaping and formulation of MOFs have been rarely studied in the literature as shown in **Figure 3**. Traditionally, most MOF powders were shaped by compression. This way of shaping induced irreversible amorphization and results in significant loss of internal surface area and, in most cases, loss of catalytic activity per unit mass. Küsgens *et al.* reported the first monolith MOF in 2010.⁴³ The group synthesized and extruded HKUST-1 monoliths. The resulting monolithic structures had a specific surface area of 370 m²/g and showed a high mechanical stability of 320 N. The majority of experimentally determined BET surface area of HKUST-1 is around 1000 m²/g.⁴⁴ This means that the extrusion negatively affected the porosity of MOF; ca. 60 % decrease in SSA. Another way of shaping MOF powders is by using binders; which is a common technique to pelletize zeolites. Binders used for zeolites can either be removed or condensed at high temperature (calcination), but it is not suitable for MOFs since they are vulnerable to heat treatment and suffer thermal degradation.

A novel method utilizing hydrocolloids to prepare shaped spheres of MOF was developed by Spjelkavik *et al.*⁴ A slurry containing microcrystalline CPO-27-Ni particles with either alginate or chitosan solutions was added dropwise to solutions of Ca²⁺ ions and base, respectively. Both calcium ions and base act as gelling agent as described in more detail in **Section 1.2.3**. These slurry droplets precipitate quickly in contact with gelling agents.

1.2.2. Encapsulation

Encapsulation is a process where the pre-selected core material(s) is entrapped by a porous or impermeable membrane. In this work, the main aim of encapsulation is the immobilization of MOF powders. There is a number of naturally occurring substances known to form stable gels (hydrogels) in contact with a gel-inducing agent. Alginate, chitosan, and carrageenan are some of these hydrocolloid-forming polysaccharides, and they are largely used in the pharmaceutical and food industry. The properties of gels^a can be manipulated (e.g. hardness/thickness of the membrane⁴⁵, compressive⁴⁶⁻⁴⁷ and shear properties⁴⁷, and tensile properties⁴⁸).

As opposed to the food industry for which the prerequisites are high production rates and low cost, encapsulation of MOFs has more stringent criteria. Beads should be monodispersed, spherically shaped, homogeneous, and mechanically resistant without affecting the porosity of the material. The methodology should also allow the production of beads in different sizes and has a narrow size distribution.

The main methods to produce the beads can be classified into three categories; chemical, physicochemical, and mechanical processes. Hydrogel beads are produced when the polymer in the binder material (e.g. hydrocolloid polysaccharides) is cross-linked through gel-inducing agents (e.g. multivalent cations). This physicochemical method is called *ionotropic gelation*.

1.2.3. Alginate properties

Alginate has become the most widely used encapsulation matrix because it is cheap, non-toxic and biodegradable. In addition to applications mentioned earlier, calcium alginate (water insoluble alginate salt with calcium ions bonded to carboxylic functional groups in the polymer) can be used to remove heavy metals such as lead, copper, and zinc due to its ion exchange property.⁴⁹

Ion exchange can be defined as a reversible exchange of ions between a liquid and a solid without changing the structure of a solid material. This solid material is an ion exchange resin. Insoluble alginate salts act as an ion exchange resin. It is a polymer with crosslinking (chemical “bridge” between carbon chains in a polymer).

^a Alginate hydrogel is used as an example.

Physical properties of alginate depend highly on the content of the molecular structure; the average molecular weight and the ratio of guluronate (G) to mannuronate (M). G:M ratio varies depending on the natural source.⁵⁰ Three different block types are present in alginates; M-block with consecutive M residues (MMMMM), G-block with consecutive G residues (GGGGG), and alternating M and G residues (MGMGMG) (**Figure 8**).

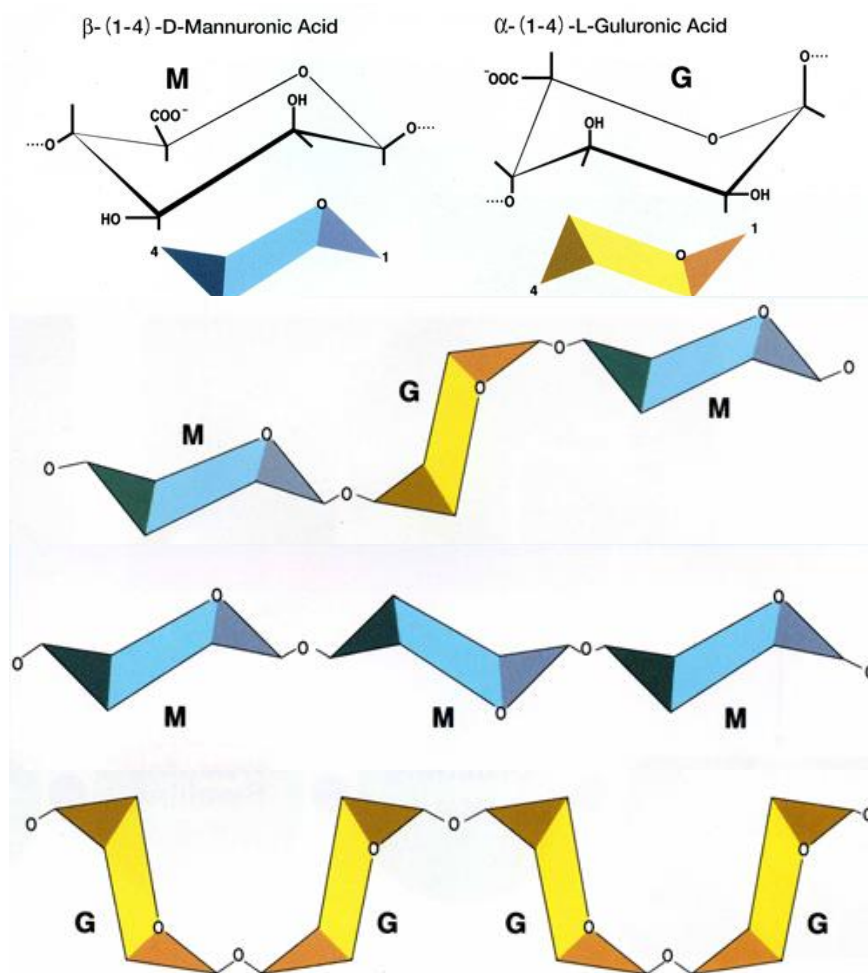


Figure 8: Two residues M and G in alginates and three different blocks types composed of M and G residues. Acquired from kimica-alginate website.¹

It is believed that only G-blocks and alternating MG-blocks participate in crosslinking. The G-blocks of the polymer form junctions with the G-blocks of adjacent polymer chains by reacting with multivalent cations (except for Mg^{2+}). In this way, G-blocks and MG-blocks form an ordered structure often illustrated by an egg-box model (**Figure 9**). The difference in

G:M ratio, sequence, G-block length and molecular weight account for the differences in resulting hydrogels.⁵¹

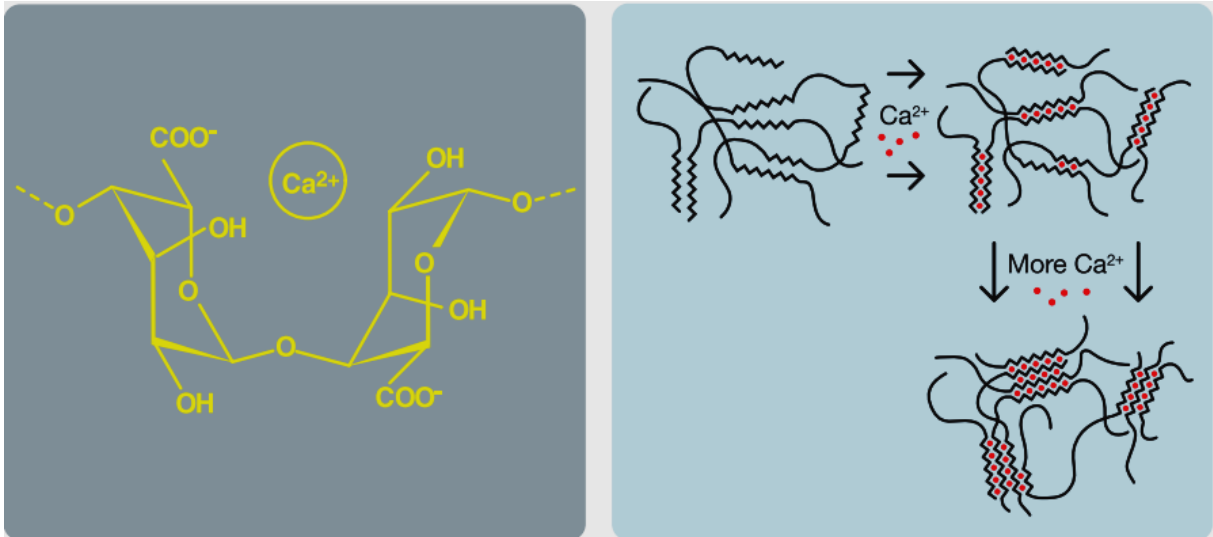


Figure 9: Calcium binding site in G-blocks (left). “Egg-box” model for alginate gel formation (right).

Alginate solution droplet undergoes several steps in the gelation bath before it becomes insoluble hydrogels (**Figure 10**). The droplet that falls freely will be deformed upon the contact with the gelation bath due to the impact. This occurs because of the surface tension of gelation bath. The droplet then sinks will form a “tail” while being detached from

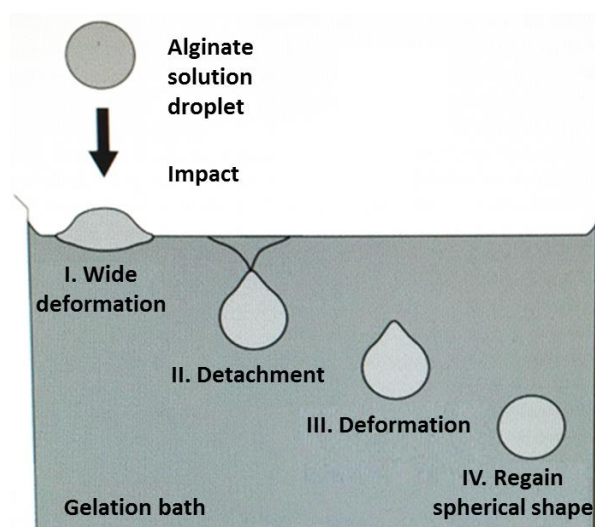


Figure 10: The first few moments in the gelation bath. This shows how the shape of a droplet changes over time. Reproduced from Lee, B.-B. et al., *Chem. Eng. Technol.*, 36(10), 1627, 2013)

the surface of bath. Before it regains its spherical shape the droplet stays deformed shortly. When the gelation occurs too fast the droplets will be gelled at this stage and become tear-shaped.

The gelation distance (or collecting distance; the distance between the tip from which the alginate solution droplet detach and the surface of gelation bath) also plays a dominant role in shape the gel beads. The gelation distance varies depending on the alginate solution viscosity (**Figure 11**). It is important to note that the alginate solution viscosity is a balance of forces so it should also depend on the properties, density and loading of MOF added to it. There is no ultimate manual for making spherical beads; the distance should be chosen carefully by “trial-and-error” method.













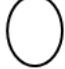
<u>Collecting distance x</u>	<u>Alginate viscosity η</u>		
	<u>$\eta < 150 \text{ mPa}\cdot\text{s}$</u>	<u>$150 \text{ mPa}\cdot\text{s} > \eta > 5000 \text{ mPa}\cdot\text{s}$</u>	<u>$\eta > 5000 \text{ mPa}\cdot\text{s}$</u>
<u>$x < 3 \text{ cm}$</u>	<u>Tear</u> 	<u>Tear</u> 	<u>Tear</u> 
	<u>Pear</u> 		
<u>$3 \text{ cm} < x < 270 \text{ cm}$</u>	<u>Pear</u> 	<u>Spherical</u> 	<u>Pear</u> 
	<u>Irregular</u> 		
<u>$x > 270 \text{ cm}$</u>	<u>Irregular</u> 	<u>Egg</u> 	<u>Spherical</u> 
		<u>Irregular</u> 	<u>Egg</u> 

Figure 11: Inter-relationship effect of the collection distance and viscosity of alginate solution on the shape of Ca-alginate beads. (Reproduced from Lee, B.-B. et al., *Chem. Eng. Technol.*, 36(10), 1627, 2013.)

1.2.4. Ergun Equation and Pressure Drop

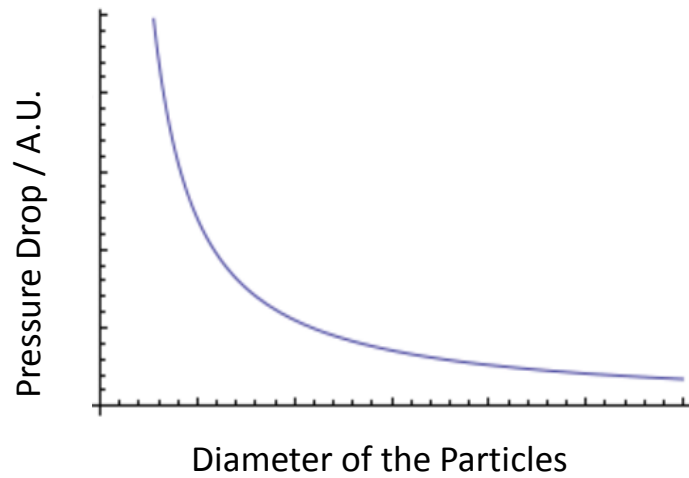


Figure 12: The relationship between the pressure drop and the particle sizes in a packed bed..

Usually, packed beds are used as catalytic reactors where a tube is filled with catalyst particles. Ideally, particles have to be small so that diffusion limitations are minimized. However, as the particles are getting smaller, the pressure drop becomes greater, as shown in **Figure 12**. Thus, the appropriate particle size should be selected. Ergun equation describes the pressure as a function of distance down the reactor. The equation is a function of the diameter of the particles in the packed bed; the pressure is inversely proportional to the diameter of the particle. Ergun equation is given by:

$$\frac{dP}{dZ} = - \frac{(1 - \emptyset)|v|}{D_p \emptyset^3 A_c} \left[\frac{150(1 - \emptyset)\mu}{D_p} + 1.75 \frac{\rho v}{A_c} \right]$$

Where

P = Pressure in the packed bed

Z = Distance down the reactor.

D_p = Diameter of the particles

\emptyset = Void fraction of the volume of the tube (volume that is not occupied by the catalyst particles.)

A_c = Cross-sectional area of the pipe

v = Volumetric flow rate.

μ = Viscosity of the gas. This is a function of temperature; $\frac{\mu}{\mu_0} = \left(\frac{T}{T_0}\right)^{0.7}$.

ρ = Mass density

The first term in brackets on right-hand side describes laminar flow and the second is from turbulent flow.

A negative sign on the right-hand side term is there because as one moves down the reactor and Z increases, the pressure decreases. The viscosity term is almost constant.

The velocity v in the second term is an absolute value so that when the flow direction in the bed is changed, the overall equation get a minus sign.

1.2.5. Varying the Size of Beads

The volume is measured when a droplet falls from a tip (capillary). When the drop falls, its size (volume) will be determined of the tip (capillary) and the surface tension. The Tate's Law measures the surface tension of a liquid. The drop "hangs" in the surface, so that:

$$F = 2\pi a\gamma$$

Where:

a is the internal radius of tip

γ is the surface tension.

There are sources of error in this equation:

- 1) The surface tension does not work completely vertically at detachment.

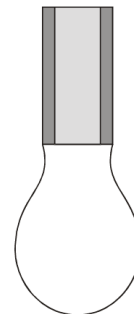


Figure 13: An illustration of a liquid droplet falling off at the tip of a pipette.

2) A part of the drop is left on the tip

General equation is then given by:

$$\gamma = \Phi \frac{F}{2\pi a} = \Phi \frac{V\rho g}{2\pi a}$$

Where:

Φ is a correction factor

V is the volume of the drop

ρ is the density of the drop

g is the gravitational acceleration

The volume of the drop is given by $\frac{4}{3}\pi r^3$, assuming it is spherical. r is the radius of the drop. Rearranging the equation above so that it describes the relationship between the radius of tip and radius of drop:

$$a = r^3 \Phi \frac{4\rho g}{3 \cdot 2\gamma} = r^3 * A$$

$$A = \Phi \frac{4\rho g}{3 \cdot 2\gamma}$$

2. Experimental Methods

2.1. Formulation

2.1.1. Reagents Used in this work

UiO-66 batch:

SH 55

This batch of UiO-66 was employed in every formulation in this thesis. Readers may refer to **Appendix 7.1** for detailed synthesis of this batch. It should be pointed out that author did not synthesize any of the materials in this work since this was out of scope.

For formulation:

5 different alginates from FMC Biopolymer were used in this work (**Table 1**). Each alginate differs from other alginates in viscosity, molecular weight and M:G ratio (refer to **Section 3.1** for more detail). All alginates were used without further purification.

Table 1: 5 different sodium alginates purchased from FMC Biopolymer.

Product Name	Chemical Name	CAS number
Protanal GP 7450	Sodium alginate	9005-38-3
Protanal GP 5450	Sodium alginate	9005-38-3
Protanal LF10/60L	Sodium alginate	9005-38-3
Protanal LF10/60	Sodium alginate	9005-38-3
Manugel GMB	Sodium alginate	9005-38-3

In **Section 3.1**, these alginates with different properties were used for the formulation in order to investigate the following:

- 1) How the M:G ratio affects the mechanical strength of the beads.
- 2) How the molecular weight affects the thermal stability of alginates.

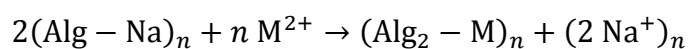
Table 2: Sources of gelling agents and their CAS numbers.

Source	CAS number
CaCl ₂ ·6 H ₂ O	7774-34-7
Ba(NO ₃) ₂	10022-31-8
CuSO ₄ ·5 H ₂ O	7758-99-8
Al(NO ₃) ₃ ·9 H ₂ O	7784-27-2
Cr(NO ₃) ₃ ·9 H ₂ O	7789-02-8
Zr(SO ₄) ₂ ·4 H ₂ O	7446-31-3
ZrOCl ₂ ·8 H ₂ O	13520-92-8
ZrO(NO ₃) ₂ ·x H ₂ O	14985-18-3

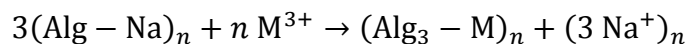
In **Section 3.7**, different kinds of salts were used (**Table 2**). These chemicals were dissolved in 50 mL distilled water. The concentration of each component was as such that the concentration of each cation (i.e. Ba²⁺, Cu²⁺, Al³⁺, Cr³⁺ and Zr⁴⁺) is the same as the concentration of Ca²⁺ ions in the gelation solution with 2 % (w/v) of CaCl₂·6 H₂O. In order to have same overall charge, the calculated weight of components was multiplied by 2/3 and by 1/2 for trivalent and tetravalent cations, respectively.

Reaction equation for gelation between sodium alginate and multivalent cations:

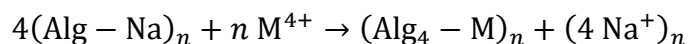
Divalent:



Trivalent:



Tetravalent:



The amount of salts was calculated according to the mol ratio according to the reaction equation above.

2.1.2. Method

A known quantity of the MOF powder (UiO-66, batch SH-55) was added to pre-measured distilled water. The MOF/water mixture was stirred 10 minutes in order to have MOF powder well dispersed in water. A known quantity of pre-selected sodium alginate powder subsequently added. **Table 3** summarizes the concentrations and types of MOF and sodium alginate used in each experiment. MOF/alginate slurry was stirred for approximately 60 minutes in order to make the slurry as homogeneous as possible. The stirred slurry was then added to the gelation bath drop by drop using a pipette tip. The typical gelation distances (described in **Section 1.2.3**) in most experiments were 3-5 cm. The gelation condition is described in **Section 2.1.3**. Gelled MOF beads were taken out from the gelation bath and washed with distilled water (see **Section 2.1.4**). Washed beads were then dried before activation (see **Section 2.1.5 and 2.1.6**, respectively). All beads were activated prior to all measurements employed in this thesis.

All formulations in this work were performed at room temperature (23 °C).

Table 3: Concentrations and types of MOF powder and sodium alginate used in each experiment.

Section	Alginate (type, conc.)	Dry MOF content
3.1	All (2 %(w/v))	90 wt%
3.2	GP7450 (0.45 – 1.8 %(w/v)) Manugel (1.5 – 2.0 %(w/v))	85 – 97.6 wt%
3.3	GP7450 (1.8 %(w/v))	85 wt%
3.4	Manugel (2 %(w/v))	90 wt%
3.5	GP7450 (1.8 %(w/v))	85 wt%
3.6	Manugel (1.5 %(w/v))	90 wt%
3.7	Manugel (1.5 – 2.0 %(w/v))	90 wt%
3.8	Manugel (2 %(w/v))	90 wt%

In **Section 3.6**, the following experimental setup was employed:

A custom-built setup was used in this work. A syringe pump (Perfusor Compact purchased from Braun) was used to pump MOF/alginate mixture at a constant rate (25.0 mL per min). Pipette tips of 4 different internal diameters (1.97 mm, 0.98 mm, 0.68 mm and 0.35 mm) were used to make droplets in different sizes.



Figure 14: Custom experimental setup used in this work. A syringe pump pumps MOF/alginate mixture at a rate of 25 mL per minute. Pipette tips with four different diameters are connected to the PVA hose. Free fall distance was ~4 cm.

20 mL of MOF/alginate mixture was prepared. DWL-10 was formulated using alginate Manugel (1.5 % (w/v)), and activated at 135 °C for 2 hours prior to crushing strength measurement, N₂ and CO₂ sorption measurement. CO₂ uptake was measured at 30 °C, and wait time was 5 minutes between each data point.

2.1.3. Gelation

The gelation bath was prepared by dissolving a known quantity of different salts in **Table 2** in distilled water. **Table 4** shows a brief overview of gelation conditions employed in this thesis. No stirring was employed during the gelation in order to eliminate the chance of physical damage that may be caused by a magnetic stirring bar. All gelation baths were prepared at room temperature (23 °C)

Table 4: Gelation conditions employed in this thesis.

Section	Salt	Salt concentration in the gelation bath	Gelation Time	pH
3.1	CaCl ₂ ·6 H ₂ O	2 % (w/v)	30 min	6.1 (at 23 °C)
3.2	CaCl ₂ ·6 H ₂ O	2 % (w/v)	30 min	6.1 (at 23 °C)
3.3	CaCl ₂ ·6 H ₂ O	0.2 - 10 % (w/v)	30 min	6.1 (at 23 °C)
3.4	CaCl ₂ ·6 H ₂ O	2 % (w/v)	3 - 840 min	6.1 (at 23 °C)
3.5	CaCl ₂ ·6 H ₂ O	2 % (w/v)	30 min	6.1 (at 23 °C)
3.6	CaCl ₂ ·6 H ₂ O	2 % (w/v)	30 min	6.1 (at 23 °C)
3.7	All	Corresponding to [Ca ²⁺] in 2 % (w/v) CaCl ₂ ·6 H ₂ O gelation bath. (See Section 2.1.1)	30 min using Ba(NO ₃) ₂ and CuSO ₄ ·5 H ₂ O. 150 min for other salts (See Section 3.7)	1.3 – 10 (at 23 °C)
3.8	CaCl ₂ ·6 H ₂ O	2 % (w/v)	30 min	6.1 (at 23 °C)

2.1.4. Washing

Each formulated beads were washed three times with distilled water to remove the excess calcium ions and chloride ions that may be present in the beads. Washing water was replaced 3 times during washing in order to speed up the washing procedure. Washing time was 10 - 15 minutes in every experiment except for **Section 3.2** where various washing times (0 – 90 minutes) were employed to investigate the effect of washing time on the performance

(i.e. crushing strength, porosity) of beads. Beads were filtered before each set of washing. Washing was performed at room temperature.

2.1.5. Drying

Washed beads were dried at 40-60 °C overnight in an air oven in order to minimize the thermal damage on the alginate in beads (discussed more in **Section 3.2**). When the beads were dried (on the surface), they were activated (See **Section 2.1.6**) prior to other measurements.

2.1.6. Activation

Prior to any measurements, beads were activated to evaporate water that may be present after drying at relatively low temperature (40 – 60 °C). Activation conditions in each experiment are shown in **Table 5**. Slight color change was observed after activating beads at 150 °C for 3 hours (**Figure 15**).

Table 5: Activation conditions in each experiment.

Section	Activation Temperature (°C)	Time (Hours)
3.1	120 – 135 (Beads) 200 (Calcium alginates)	2
3.2	150	3
3.3	150	2
3.4	135	2
3.5	120 - 150	2
3.6	135	2
3.7	135	2
3.8	135	2

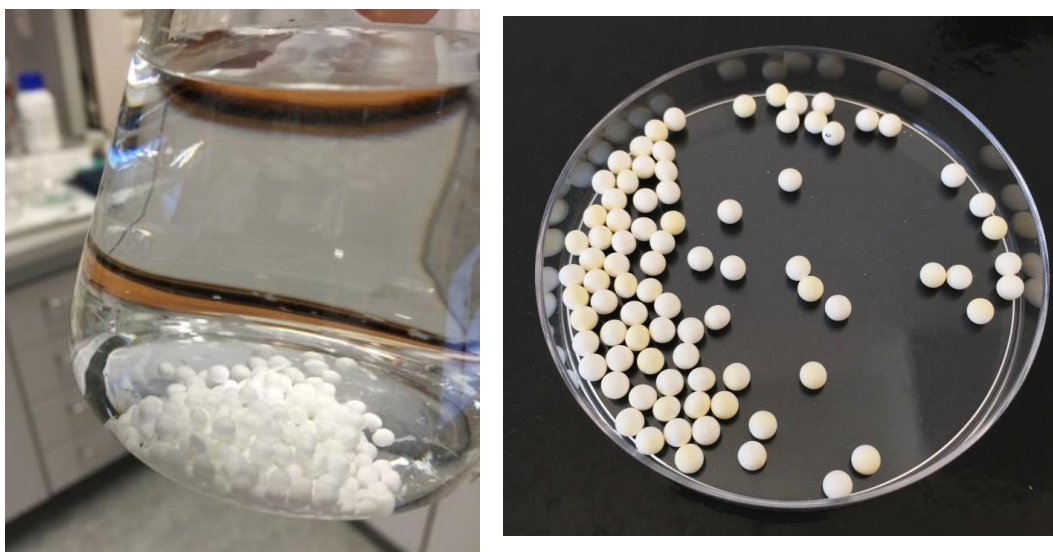


Figure 15: MOF beads in the gelation solution (left) and after activation at 150 °C for 3 hours (right)

2.2. Compression Test

3 to 5 formulated beads having similar shape and size were selected for the compression test in order to minimize the deviation in mechanical stability. The machine used was Zwick/Roell Z250 universal test machine equipped with 500 N load cell. One bead at a time was placed between the parallel compression plates. The lower compression plate was lifted at a rate of 0.2 mm per minute. Force in newton was plotted as a function of deformation of the bead in millimeter. The output data was collected using the software TestXpert II.

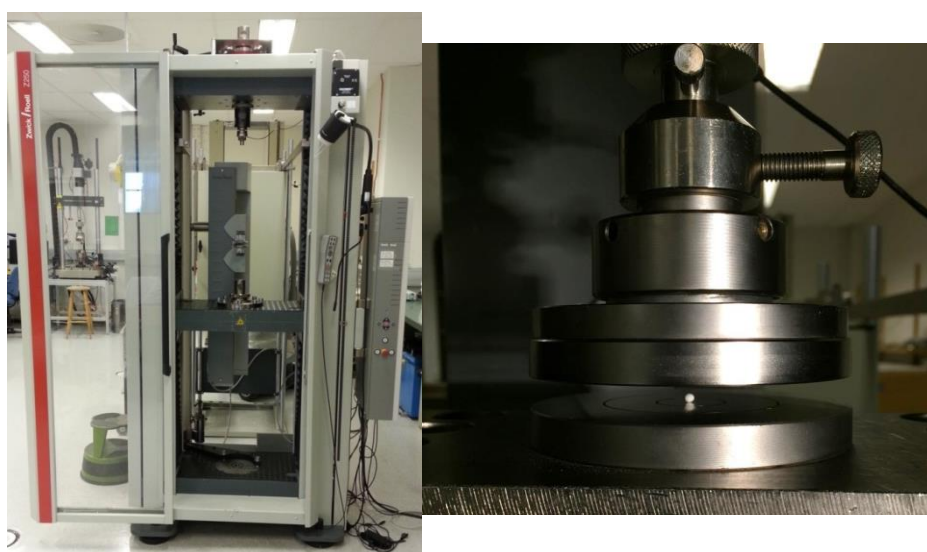


Figure 16: The universal test machine used for the compression test on the sample beads.

2.3. Powder X-ray Diffraction

2.3.1. Basic Description of the Technique

Powder X-Ray diffraction (PXRD) is a common technique for the study of crystalline materials. In a PXRD experiment, monochromatic X-rays (of wavelength λ of the order of 0.1 nm) are produced by decay of electrons excited to higher energy levels in the target (a metal target (usually copper) being bombarded with electrons in a vacuum tube). X-rays with several wavelengths are generated from different transitions. The multiple wavelengths generated in the tube are selected (thus, monochromatic) using optics.

When monochromatic X-rays are directed to the sample, the angle (θ) between the sample and the X-ray beam is varied. X-rays interact with the regular arrays of electron densities in the crystal lattice of the sample and are diffracted as they pass through. The diffracted beams form a diffraction pattern due to interference. X-rays can only reach the detector when they constructively interfere with the incident beam. This phenomenon is called Bragg's Law and is described as follows:

$$n\lambda = 2d \sin \theta$$

Where:

n is a positive integer,

d is the lattice spacing, the distance between a set of parallel crystal planes in the sample,

λ is the wavelength of the diffracted beam,

θ is the diffraction angle

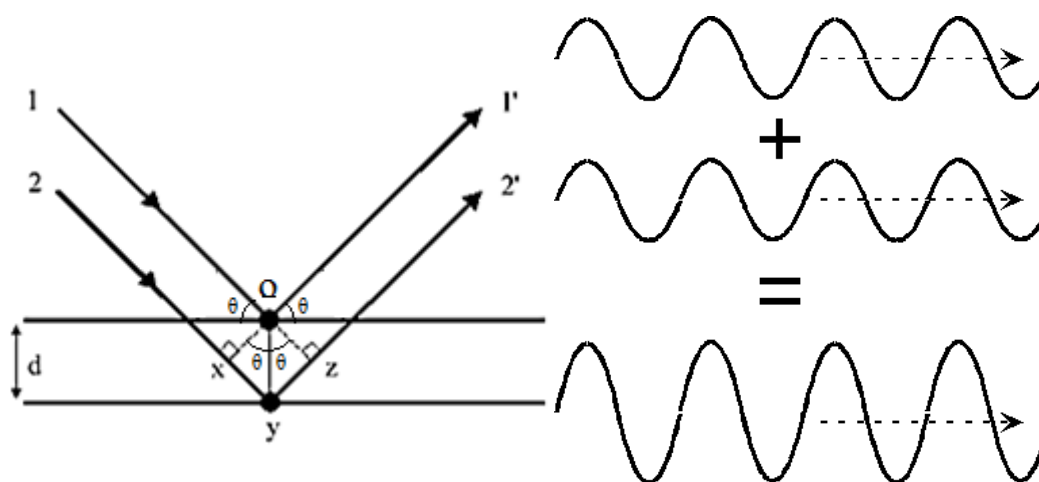


Figure 17: Illustration of Bragg diffraction by crystal planes (left). The path difference between beams 1 and 2 is $xy + xz = 2oy \sin\theta$. When Bragg's Law is satisfied, constructive interference occurs (right).

This conditional detection of X-rays gives rise to a diffractogram which is a plot of the intensities (in arbitrary units) of the diffracted beams vs their diffraction angles (2θ). Each crystalline structures have their unique “fingerprints”. One can determine the space group and cell parameters of an unknown compound by analyzing observed reflections (peaks) at 2θ values in which the Bragg's Law is satisfied in PXRD pattern. This was the case for UiO-66.⁶

UiO-66 has a face-centered cubic (fcc) unit cell. The symmetry of a fcc unit cell leads to destructive interference of certain diffraction peaks. For instance, diffraction from (200) peaks destructively interfere with (100) peaks; the Bragg's Law is not satisfied for (100) peaks, thus not observed in the diffraction pattern. This certain set of “forbidden” peaks is called the systematic absences. For fcc lattices – Miller indices (h,k,l) must either be all odd or all even (0 considered even). Some of characteristic peaks are shown in **Figure 18**.

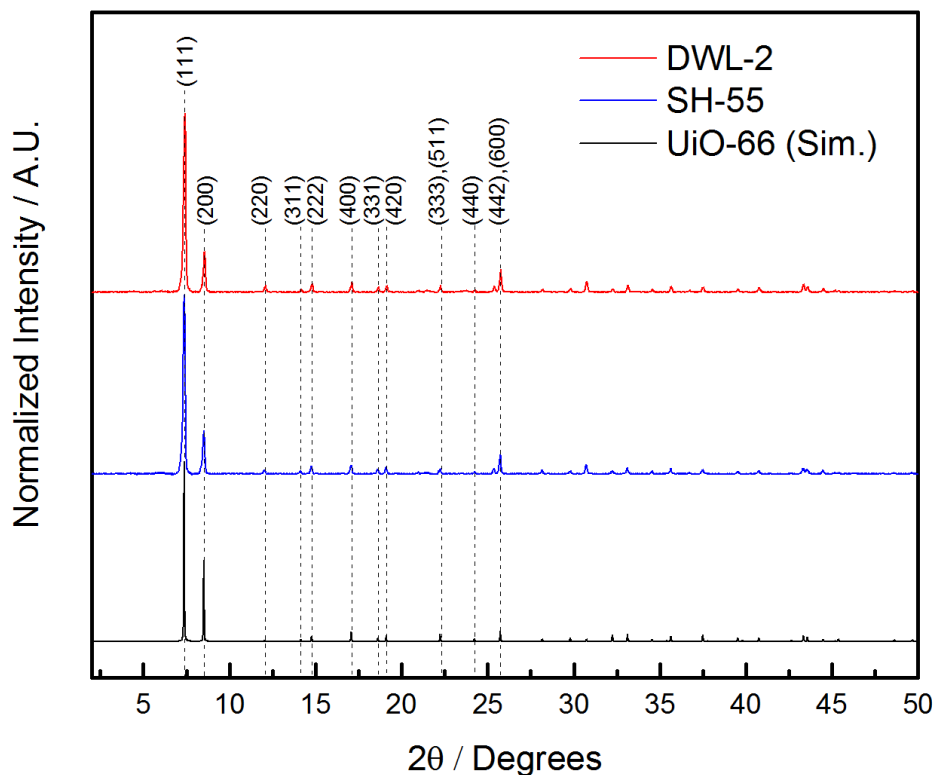


Figure 18. A simulated PXRD pattern of (Zr)UiO-66 showing its characteristic peaks. A batch (SH-55) and its formulated bead (DWL-2) are also shown for comparison.

2.3.2. Purpose of Usage in this Thesis

Powder X-ray diffraction (PXRD) was used for the following purposes:

To determine whether the desired phase (non-modified UiO-66 phase since this material was used as the starting material for the formulation) was present in the formulated products. This was achieved by comparing the experimental data of a grounded sample with the simulated one and the initial powder sample that was used.

2.3.3. Experimental Methods

Samples were prepared by grinding approximately 30 mg of formulated MOFs and dispersing them on a flat glass plate PXRD sample holder with a diameter of 2.5 cm. The holder was then covered with a piece of plastic wrap to spread, flatten and hold the sample in position for measurement. The sample must be well ground and flattened on the sample holder as the proper sample preparation is crucial in order to avoid errors such as wrong peak positions, wrong peak intensities, wrong peak shapes and broad/double peaks. The plastic

wrap is in the PXRD patterns, appearing as two broad peaks at *ca.* $2\theta=21-22^\circ$ and at $2\theta=26-27^\circ$.

PXRD patterns were collected on a Bruker D8 Discover diffractometer equipped with a focusing Ge (111) monochromator (the angle (θ) for the Ge (111) peak is 27.3°), using Cu- $K\alpha 1$ radiation ($\lambda = 1.54056 \text{ \AA}$) and a Bruker LYNXEYE detector. The PXRD data was obtained in reflectance Bragg-Brentano geometry over a 2θ range of $2-50^\circ$.

Prior to measurement, all the formulated MOF samples were ground thoroughly using a mortar and subsequently pressed using a manual hand powder press. A pressure of 1 ton was employed for 30 secs for all of the tested samples.

2.4. Analysis of adsorption/desorption isotherms

The instruments (BELSORP-mini II and BELSORP-max) employed for the sorption measurements use the volumetric theory to measure adsorption isotherms. The adsorption amount relative to the pressure can be obtained as measured data. The relationship between them is referred to as an adsorption isotherm.

In physical adsorption, adsorption isotherms can be classified as one of 6 types, as shown in **Figure 19**.

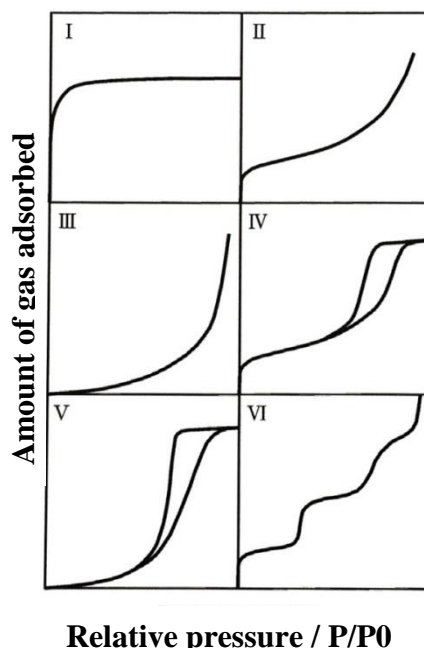


Figure 19 IUPAC classification of adsorption isotherms

Typical size of pores is classified as shown in **Table 6**.

Table 6: IUPAC classification of pores

	Pore diameter [nm]
Micropore	Up to 2
Mesopore	2 to 50
Macropore	50 or up

Adsorption isotherms are classified as shown in table 2 based on the strength of the interaction between the sample surface and adsorptive, and the existence or absence of pores. However, some actual samples do not fit into adsorption isotherm types I to IV. These may be measured as mixed types of adsorption isotherms. For example, nitrogen adsorption for a porous sample with large external surface area may generate a compound isotherm resembling types I and II, or types I and IV. To analyze an adsorption isotherm, one has to assume certain sample features, such as the pores from the shape of the isotherm.

2.4.1. Nitrogen Adsorption Isotherms

2.4.1.1. Basic Description of the Technique

Nitrogen adsorption is a common technique for the characterization of a wide range of porous materials. In a nitrogen adsorption isotherm, the total amount of nitrogen adsorbed by the material under study is measured as a function of pressure. Prior to measurement, the material must be emptied by heating under vacuum for some time so that its entire internal surface area is available for nitrogen adsorption. The temperature of heat treatment and the duration was determined based on previous experiences. After this pre-treatment, known amount of nitrogen is introduced to an air-tight glass cell (kept at constant temperature (77 K), hence “isotherm”) containing the sample. The measurement proceeds discontinuously; after each step, the system is allowed to equilibrate and the pressure in the cell is measured and compared with that in an empty reference cell in which the same amount of nitrogen gas is introduced. The software infers the volume of nitrogen which is adsorbed by the sample at each stage in the isotherm. The amount of nitrogen introduced to the sample cell increases

gradually until it reaches atmospheric pressure. Measurements are made in the reverse fashion during desorption.

The y-scale unit of the isotherms presented herein is $V_a(\text{cm}^3(\text{STP}) \text{g}^{-1})$, the volume of standard nitrogen (273.15 K, 1 bar) adsorbed per gram of sample (weighed after the pre-treatment). This is plotted against relative pressure P/P_0 ; a dimensionless quantity which describes the pressure in the sample cell as a fraction of the atmospheric pressure.

2.4.1.2. Purpose of Usage in this Thesis

Nitrogen adsorption isotherms were used to assess the porosity (thus the BET surface area) of the formulated MOF samples. Using polymer (such as alginate used in this thesis) as a binder material might block the pores of the MOF material, resulting in less BET surface area than that of MOF material. Hence, the nitrogen adsorption isotherms are useful tool to check the loss in porosity of MOF material.

The specific surface area of formulated MOFs (in this thesis, formulated UiO-66 samples) can be determined using nitrogen adsorption isotherms. The specific surface area is the total surface area of the material per unit mass (typically given in m^2g^{-1}), and is essentially a quantitative descriptor for porosity. It is often used as a simple means by which to compare porous materials. In this thesis, the specific surface area was determined by subjecting the nitrogen adsorption isotherms to linear regression in accordance with the BET model of multilayer adsorption. BET model, however, is known to overestimate the surface area of the material when compared to “real” or “geometric” values obtained by simulations [145]. Still, the method is ubiquitous in the MOF literature and is extremely useful for comparing the relative porosity of materials.

2.4.1.3. Method for Experimental Measurements

Nitrogen sorption measurements were performed on a BELSORP-mini II instrument at 77 K. In each measurement approximately 50 mg of sample was weighed into a 9.001 cm^3 sample cell. Each sample was emptied by pre-treatment at $150 \text{ }^\circ\text{C}$ under vacuum for 2 hours. The conditions for this pre-treatment were chosen based on the solvent weight loss step in the

TGA trace. Measurements were performed without exposing the emptied samples to atmosphere.

2.4.1.4. Method for Simulations

Adsorption isotherms were simulated by use of the “**Sorption Tools**” in Accelrys Materials Studio version 8.0. The “**Adsorption isotherm**” task was chosen. Simulations were performed at a temperature of 77 K using N₂ molecule as the adsorptive and a single unit cell of the hypothetical structure of interest as the adsorbent. Prior to simulation, all the molecular structure of interest was geometry optimized using “**Forcite Tools**” in the same software. The “**Geometry Optimization**” task was chosen. “Smart” algorithm was used and the quality of the calculation was set to “**Ultra-fine**” with the convergence tolerance of 2.0E-5 kcal/mol in energy, 0.001 kcal/mol/Å in force and 1.0E-5 in displacement. Maximum iterations was set to 500. Universal force field (Ultra-fine quality) was adopted. “**Use current**” setting was employed for charges. Both electrostatic forces and van der Waals forces were calculated atom based.

For the “**Adsorption isotherm**” task, the Metropolis method and COMPASS force field were adopted. Simulations were performed over a pressure range of 0.01 – 100 kPa, in which 50 fugacity steps were distributed logarithmically so that there were more data points in the steep initial portion of the isotherm. The “**Ultra-fine**” quality setting (involving 1,000,000 equilibration steps and 10,000,000 production steps) was used for all simulations. Charges were “**force field**” assigned. Electrostatic forces were calculated with the Ewald method while van der Waals forces were calculated atom based. No constraints were assigned.

Due to the statistical nature of the calculations, the isotherms (very) slightly differed when simulations were repeated.

In order to compare the simulated isotherms with the experimental data, the y-scale units of the simulated isotherms were converted from “**N₂ Molecules Per Unit Cell**” to “**V_a (cm³(STP)g⁻¹)**”, the volume of nitrogen adsorbed (STP) per gram of material:

$$V_a (\text{cm}^3(\text{STP})\text{g}^{-1}) = \frac{N_2 \text{ Molecules Per Unit Cell}}{M_{\text{Unit Cell}}} \cdot \frac{RT}{N_a P} \quad (1)$$

Where:

$M_{\text{Unit Cell}}$ is the molar mass ($\text{g}\cdot\text{mol}^{-1}$) of the contents of the unit cell from which the isotherm was simulated,

R is the gas constant ($= 8314.46 \text{ cm}^3\cdot\text{kPa}\cdot\text{K}^{-1}\cdot\text{mol}^{-1}$),

T is the standard temperature ($= 273.15 \text{ K}$),

N_a is Avogadro's number ($= 6.022 \times 10^{23} \text{ mol}^{-1}$),

P is the standard pressure ($= 100 \text{ kPa}$).

While the x-scale units were converted from *Total fugacity(kPa)* to *Relative pressure(p/p₀)*:

$$\text{Relative pressure } (p/p_0) = \frac{\text{Total Fugacity (kPa)}}{\text{Atmospheric Pressure (= 101.325 kPa)}} \quad (2)$$

After the units of the simulated isotherms were converted as described above, the BET surface area of this simulated model (and all the other samples mentioned in this thesis) was calculated *via* the method described in section 2.4.1.5.

2.4.1.5. Method for Determining the BET Surface Area

BET surface areas were calculated by applying the linearized BET equation to the N_2 adsorption isotherms, whether simulated or experimentally measured:

$$\frac{p/p_0}{V_a(1 - p/p_0)} = \frac{C - 1}{V_m C} (p/p_0) + \frac{1}{V_m C} \quad (3)$$

Where:

p and p_0 are the equilibrium and saturation pressure of the adsorbate, respectively.

V_a is the amount of gas adsorbed. In this work, the units are in $\text{cm}^3(\text{STP})^{-1}$.

V_m is the amount of gas required to form a monolayer on the adsorbent. Units are in $\text{cm}^3(\text{STP})^{-1}$.

C is BET constant

The first step in the method is to plot $\frac{p/p_0}{V_a(1-p/p_0)}$ against p/p_0 . A linear region of the resulting plot is then identified and fitted. The choice of the relative pressure (p/p_0) range for the linear fit can have severe impact on the value of the BET surface area. The most vital part of the method is thus choosing the “correct” range. The range between 0.05 and 0.3 relative pressures which initially suggested by Brunauer, Emmet and Teller is only applicable to non-porous or mesoporous materials and cannot be applied for MOFs with multimodal pore size distribution; as is the case for UiO-66 (**Figure 7**). To this end, the consistency criteria originally outlined by Rouquerol et al. were employed.⁵²

- 1) The pressure should be limited to the range in which $V_a(1 - p/p_0)$ increases continuously as a function of the relative pressure p/p_0 .
- 2) The relative pressure at which the monolayer is formed (calculated from the fit as $\frac{1}{\sqrt{C+1}}$) must be within the chosen relative pressure (p/p_0) range.
- 3) The C value obtained from the linear fit must be positive.

Upon finding a pressure range that satisfies all three criteria above, the range was fine-tuned to obtain the best linear fit (i.e. maximum R^2 value) in which the three criteria are still fulfilled.

Once such a range is chosen, the volume of the monolayer (V_m) and the BET constant (C) can be extracted from the slope $\left(\frac{C-1}{V_m C}\right)$ and intercept $\left(\frac{1}{V_m C}\right)$ of the resulting linear fit.

Finally, the BET surface area was calculated with the following equation:

$$BET\ S.A. = \frac{N_a P V_m}{RT} \cdot \sigma_0 \quad (4)$$

Where:

N_a is Avogadro's number ($= 6.022 \times 10^{23} \text{ mol}^{-1}$),

P is atmospheric pressure ($= 101.325 \text{ kPa}$).

R is the gas constant ($= 8314.46 \text{ cm}^3 \cdot \text{kPa} \cdot \text{K}^{-1} \cdot \text{mol}^{-1}$),

T is the standard temperature ($= 273.15 \text{ K}$),

σ_0 is the cross sectional area of the adsorbent ($\sigma_0 = 1.62 \times 10^{-19} \text{ m}^2$ for N_2).

2.4.1.6. Example BET Analysis

The calculation of the BET surface area of one of formulated UiO-66 sample is demonstrated as an example in.

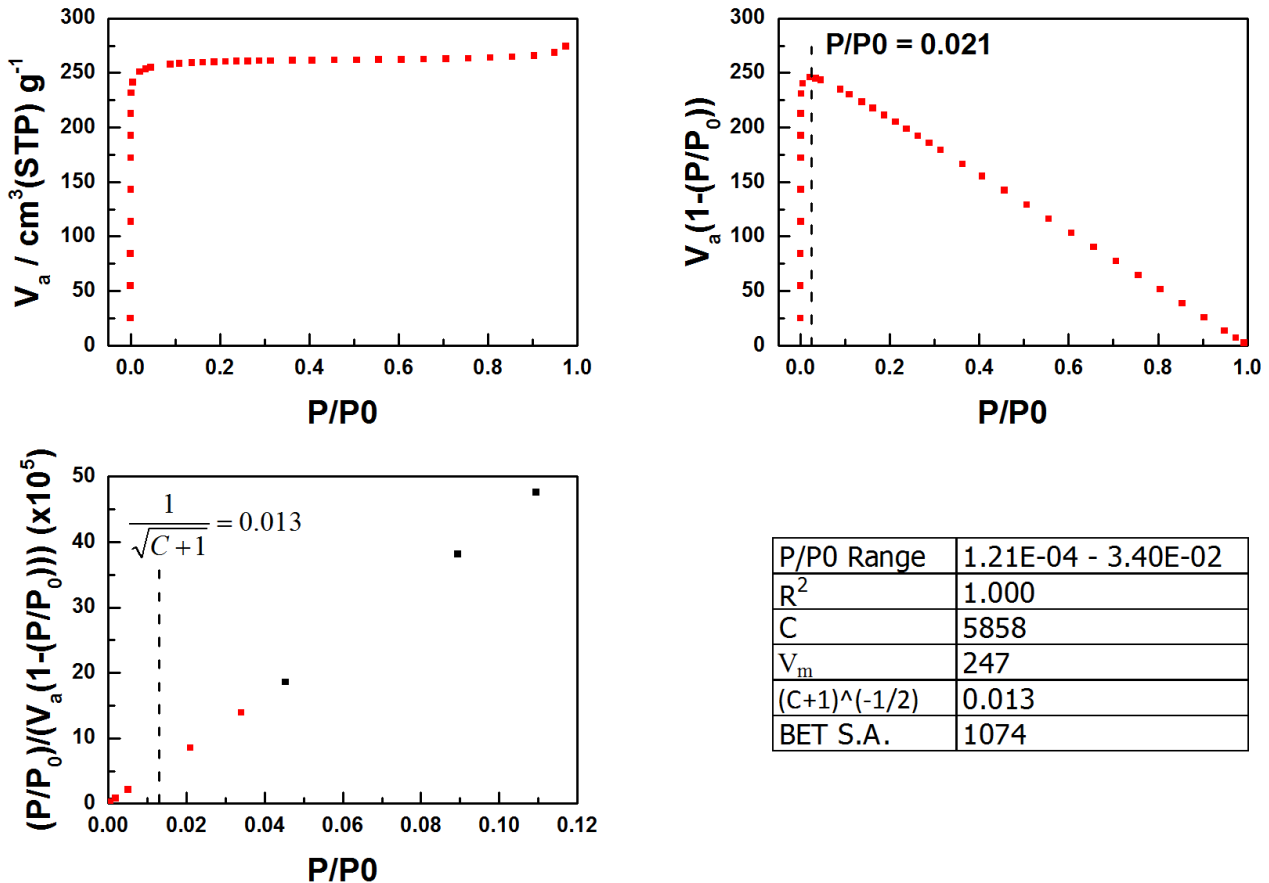


Figure 20. BET analysis of one of formulated UiO-66, DWL-2.

The nitrogen sorption isotherm (adsorption branch only) is displayed in top-left corner of the figure. The data presented in the rest of the figure is derived from this isotherm. In top-right of the figure concerns the 1st consistency criterion. Therein, one can see that $V_a(1 - (p/p_0))$ increases continuously as a function of the relative pressure P/P_0 until $P/P_0 = 0.021$, a value highlighted by the vertical dashed line in the figure. In accordance with the 1st consistency criterion, the entire P/P_0 range used for the BET analysis must be ≤ 0.021 .

Displayed in bottom-left corner of the figure is the BET plot in which the linear range was chosen. In order to maximize the correlation ($R^2 = 1.000$), only the points shown in red were included in the fit. In accordance with the 2nd consistency criterion, the value for $\frac{1}{\sqrt{C-1}}$ (=

0.013, as highlighted by the vertical dashed line) is within the chosen pressure range ($P/P_0 = 1.21 * 10^{-4} - 3.40 * 10^{-2}$).

Finally, the table in the figure provides all the information relevant to the BET analysis. In accordance with the 3rd consistency criterion, the value of the BET constant, C , is positive (= 5858).

As can be seen, the BET surface area of DWL-2 is $1074 \text{ m}^2\text{g}^{-1}$, which is slightly less than that of powder batch SH-55 ($1241 \text{ m}^2\text{g}^{-1}$). Dry MOF content in DWL-2 is 95.2 wt%. which gives; $1241 * 0.952 = 1181 \text{ m}^2\text{g}^{-1}$. The difference between measured value and calculated value is $107 \text{ m}^2\text{g}^{-1}$ or $\frac{107 \text{ m}^2\text{g}^{-1}}{1074 \text{ m}^2\text{g}^{-1}} * 100 \approx 9.7 \%$. This might be due to water content in the beads (see **Section 3.2**).

2.4.2. CO₂ Sorption Measurements

CO₂ sorption measurements were performed to assess the CO₂ capture performance of the formulated UiO-66 samples.

2.4.2.1. Method for Experimental Measurement

For low pressure CO₂ uptake measurement, CO₂ sorption isotherms were obtained by a volumetric approach using a BELSORP-max instrument over a pressure range of 0 to 100 kPa and at three different temperatures (25 °C (298.15 K), 40 °C (313.15 K) and 70 °C (343.15 K)). The measuring temperature was controlled by using an external water bath. Prior to measurement, samples were activated at 135 °C under vacuum (~2 kPa) for 180 minutes.

For high pressure CO₂ uptake measurement, CO₂ sorption isotherms were obtained by a volumetric approach using a Belsorp-VC instrument over a pressure range of 0 to 4,000 kPa and at three different temperatures (25 °C (298.15 K), 35 °C (308.15 K) and 50 °C (323.15 K)). Samples were activated at 135 °C under vacuum (~2 kPa) for 10 hours.

2.4.2.2. Isotherm fitting

Isotherm fitting was performed so that the isosteric heat of CO₂ adsorption could be determined.

The pure component CO₂ adsorption isotherms were fit to the Langmuir model over their entire pressure range (0 – 100 kPa):

$$N = N_{sat} \cdot \left(\frac{kp}{1 + kp} \right)$$

where:

p is the pressure (in 0.1 kPa) of gas (CO₂ in our case) at equilibrium with the adsorbed phase.

N is the quantity of gas adsorbed (in mmol per gram of adsorbent) at pressure p .

N_{sat} is the quantity of gas adsorbed (in mmol per gram of adsorbent) at saturation.

k is the adsorption affinity (0.1 kPa⁻¹).

2.5. Thermogravimetric Analysis – Differential Scanning Calorimetry (TGA-DSC)

2.5.1. Basic Description of the Technique

The TGA is a common technique to measure the weight of sample under investigation as a function of temperature. The sample is heated under a controlled atmosphere in a reactor at a controlled rate of heat increase. The change in weight is caused by physical process (e.g. desorption of water, endothermic) or chemical process (e.g. decomposition of the material, exothermic).

Heat flow can also be measured simultaneously, giving information of about whether the reaction is endothermic or exothermic. This technique is called DSC; differential scanning calorimetry. It is a technique in which the difference in the amount of heat required to increase the temperature of a sample and reference is measured as a function of temperature.

When the heat flow is negative (more amount of heat required to increase the temperature of a sample), the reaction is endothermic. Positive heat flow indicates the exothermic reaction.

2.5.2. Purpose of Usage in this Thesis

TGA is used to investigate the thermal stability of gelled alginate. Slow heating rate (3 °C per minute) was used in order to secure a good resolution of the data. TGA-DSC was a useful tool to determine the activation temperature for the MOF/alginate beads.

2.5.3. Measurement Method

TGA-DSC measurements were performed on Stanton Redcroft TGA-DSC, in which ca. 30 mg of sample was loaded in a Pt-crucible. Different types of calcium alginate and alginates gelled with different cations were investigated. Since the activation in this thesis is oxygen-free, samples were heated under a constant flow of N₂ (20 mL min⁻¹).

In **Section 3.1**, five different alginates from FMC biopolymer were investigated (**Table 7**). They were gelled in the gelation solution of 2 %(w/v) CaCl₂·6 H₂O. Gelation time and washing time were 30 minutes and 15 minutes, respectively. Prior to the TGA-DSC measurement, samples were dried at 40 °C in air overnight. Samples were heated from 23 °C to 200 °C at a heating rate of 3 °C per minute. The TGA instrument used in this work did not perform well at lower heating rate.

In **Section 3.7**, alginates gelled with various multivalent cations (Ca²⁺, Al³⁺ and Zr⁴⁺) were heated from 23 °C to 200 °C at a heating rate of 3 °C per minute.

2.6. Scanning Electron Microscopy

2.6.1. Basic Description of the Technique

Scanning electron microscope examines the surface of microscopic structures using a focused electron beam scanning over the surface area of interest on the sample. Large field of depth of SEM makes it possible to get three-dimensional appearances of its images. The basic schematic of SEM is illustrated in **Figure 21**. The electron gun for generation of electron beam is either thermionic or field emission type guns (FEG). FEG is used in advanced SEM systems because of its high beam brightness. An SEM optical path goes through a series of magnetic lenses; condenser lenses and an objective lens. Two condenser lenses reduce the crossover diameter of the electron beam. The objective lens focuses the electron beam as a probe with a nanometer-scale diameter. Signal electrons (BSE and SE) emitted from the specimen are detected, amplified and displayed.

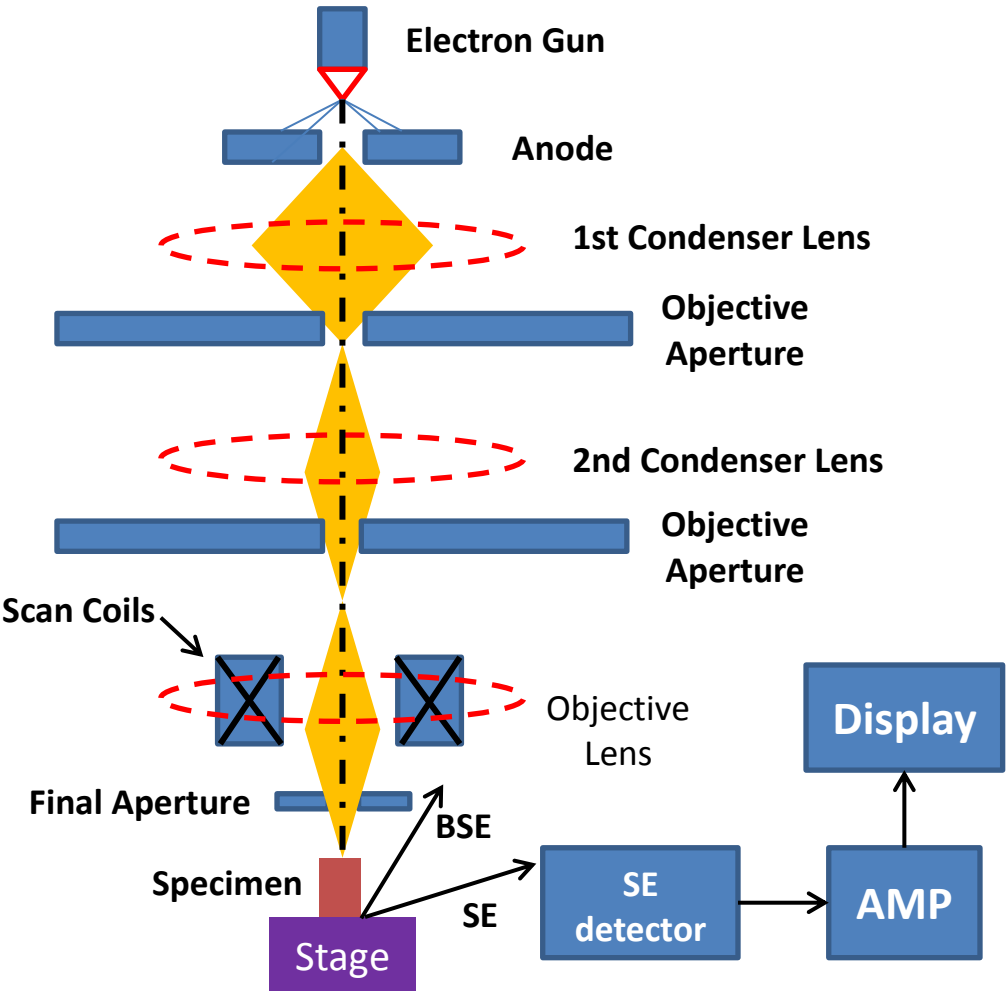


Figure 21: Structure of SEM. BSE: Back-scattered electrons, SE: Secondary electrons, AMP: Amplifier.

The resolution of SEM is determined by a cross-sectional diameter of the scanning probe d_p which is given by:

$$d_p = \left(\frac{4i_p}{\beta\pi^2\alpha_f^2} \right)^{1/2}$$

Where

i_p is the probe current

β is the beam brightness

α_f is the convergence angle of the probe.

α_f is given by:

$$\alpha_f = \frac{R_{fap}}{D_W}$$

Where

R_{fap} is the diameter of final aperture

D_W is the working distance.

The beam brightness β is proportional to acceleration voltage V_{ac} :

$$\beta \propto e V_{ac}$$

where e is the charge of electron.

Since the lower diameter of scanning probes gives better resolution of SEM, the probe current should be low, and both the beam brightness and the convergence angle should be high. Advanced SEM systems use field emission gun because it is much brighter than conventional guns.

2.6.2. Measurement Method

SEM was used to analyze the morphology of the bonded crystals in the MOF beads. Hitachi SU8230 Ultra High Resolution Cold FE-SEM was used to take all SEM images. Acceleration voltage of 1.0 kV and the probe current of 15 μA was used. A 1.5 kV deceleration voltage was applied (denoted as “-D” in all SEM images except for a) shown in **Figure 59**) in order to minimize the charging effect due to the electrically insulating property of MOF. The “landing voltage” was $2.5 - 1.5 = 1$ kV.

MOF beads were cut in half to have the surface being investigated as flat as possible. Focusing on a flat surface is easier than on a curvy surface. **Figure 22** shows how the sample was prepared for SEM and EDX.



Figure 22:MOF bead sample preparation. A bead cut in half placed on a disk plate using a carbon tape (black).

2.6.3. Elemental Analysis (via Energy Dispersive X-ray Spectroscopy, EDX)

EDX was used to determine the content of chloride, calcium and sodium content in formulated MOF beads.

Elemental analysis was performed on Hitachi SU8230 Ultra High Resolution Cold FE-SEM equipped with an Energy Dispersive X-ray Spectrometer (Quantax EDS) from Bruker. Samples were prepared by cutting them in half and placed on carbon tape (**Figure 22**). Line spectra throughout the bead were acquired with the “precise” setting at a working distance of 8.8 mm and a magnification of 30x. The accelerating voltage was set to 20 kV in order to have X-ray count rate higher than 3 kcps (kilo counts per second).

The lighter elements present in the samples (hydrogen, carbon and oxygen) cannot be reliably quantified by EDX. Hydrogen cannot be quantified because it does not have any characteristic X-rays. The characteristic X-rays of carbon and oxygen originate from transitions involving their valence electrons (i.e. those involved in their chemical bonding). It means that the analysis data associated with those elements depends on their chemical environment, resulting in unreliable quantification.

2.7. Fourier Transform Infrared (FTIR) Spectroscopy techniques

2.7.1. Basic Description of the Technique

Fourier transform infrared spectroscopy is a measurement technique that allows one to record infrared spectra. Infrared light interacts with the sample under investigation, and the interference is obtained. This is called *interferogram*. This raw data file is subsequently Fourier Transformed into an IR spectrum. Since the molecular vibrations in most cases are in the infrared region of the electromagnetic spectrum (approximately, the wavelength of between 750 nm to 1 mm), the molecular vibration data obtained using IR spectroscopy can provide useful information to identify the bond types. It is possible because functional groups give rise to characteristic bands; giving a characteristic IR-spectrum. IR spectra are given as the intensity of signal is plotted as a function of infrared wavelength (equivalently,

wavenumber). **Figure 23** shows some known wavenumber values for different types of bonds.

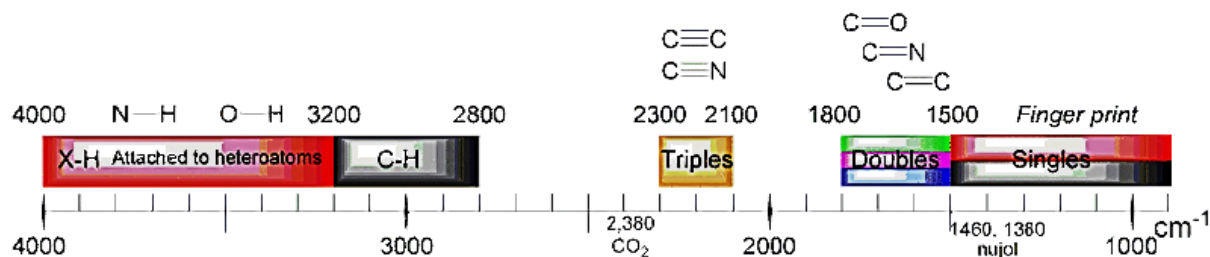


Figure 23: The positions of some of the bands from infrared spectroscopy correlation table⁵³⁻⁵⁴

There are two ways to present the spectrum peaks; transmittance and absorbance. Historically, transmittance was used for old IR-spectra due to the lack of computing power for the automatic conversion of transmittance to absorbance. Recently, IR-spectra given in absorbance have become common, and one of its advantages is that the absorbance is a logarithmic scale. This enables to detect weak signals next to very strong signals. In this work, all the IR-spectra are presented in absorbance.

2.7.2. Measurement Method

In **Section 3.5**, DWL-9-1.8%-Ca2% beads were crushed to make powder using a mortar and pestle. The powder was pressed (0.5 ton for 30 seconds) using a manual hand powder press to make a flat pellet. The pellet was placed inside a golden envelope, and it was transferred to a glass tube where it was activated. DWL-9-1.8%-Ca2% was activated in situ at three different temperatures (120 °C, 135 °C and 150 °C) for 2 hours under vacuum prior to the IR measurement. For DWL-9-1.8%-Ca2%, the data was collected from the same pellet.

Alginate GP7450 was crushed and mixed with KBr to make a pellet (with a Alg:KBr ratio of 1:10) in which the alginate was distributed as uniformly as possible.

Figure 24 shows the sample prepared for FTIR measurement.



Figure 24: Sample prepared for FTIR measurement. Crushed and pressed MOF pellet inside a golden envelope.

2.8. Optical microscopy

In **Section 3.7**, an optical microscope Leica M205 C was used to take a picture of alginate (without MOF) gelled in various conditions. Freshly gelled alginate beads were employed (before drying). Images were acquired with a magnification of 65x. Images were processed (i.e. adding a scale bar, white balance adjustment) using a software Leica Application Suite version 3.6.0.

3. Results and Discussion

3.1. Effect of Different Types of Alginates

Aim

Investigate how alginates with different properties such as molecular weight and M:G ratio differ in the mechanical and thermal stability.

Experimental

This experiment is divided into two parts:

- 1) Investigating gelled calcium alginates only (without MOF): Five different alginates used in this experiment are shown in **Table 7**. 200 mg of each sodium alginate were added to respective 10 mL distilled water. The gelation bath was prepared by dissolving 1 g $\text{CaCl}_2 \cdot 6 \text{H}_2\text{O}$ in 50 mL distilled water. Gelation time was 30 minutes. Samples were washed 3 times for 10 minutes and dried overnight in air at 40 °C prior to TGA-DSC measurement.
- 2) Compression test on beads with MOF: 5 samples were prepared. 900 mg MOF, 100 mg alginate in 5 mL distilled water were used in each sample. Each sample was gelled in the gelation bath prepared by dissolving 1 g $\text{CaCl}_2 \cdot 6 \text{H}_2\text{O}$ in 50 mL distilled water. Gelation and activation are given in **Table 8**.

Table 7: Alginates used in this experiment. The properties of alginates are given by the manufacturer.

Name	Viscosity (1%(w/v))	Molecular Weight ^b	M:G ratio
Protanal GP7450	600 – 800 mPa*s	Ca. 380 – 400 kDa	45:55
Protanal GP5450	200 – 400 mPa*s	Ca. 280 – 350 kDa	45:55
Protanal LF10/60L	40 – 60 mPa*s	Ca. 175 – 220 kDa	60:40
Protanal LF 10/60	20 – 70 mPa*s	Ca. 140 – 200 kDa	30:70
Manugel GMB	110 – 270 mPa*s	Ca. 240 – 300 kDa	40:60

^b Units given in kilodaltons; equivalent to 1000 daltons (Da). 1 Da is equivalent to 1 unified atomic unit mass (amu). $1 \text{ Da} \approx 1.66 \cdot 10^{-27}$.

Table 8: MOF bead samples prepared in this experiment.

Sample	Dry MOF content	Alginate type (conc. in MOF/water mixture)	Gelation and Activation
DWL-15-LF10/60L	SH 55 (90 %)	LF10/60L (2 % (w/v))	Gel: 2 % (w/v) CaCl ₂ , 0.5 hrs. Activated at 120 °C, 135 °C (2 hrs)
DWL-15-LF10/60		LF10/60 (2 % (w/v))	
DWL-15-Manugel		Manugel (2 % (w/v))	
DWL-15-GP5450		GP5450 (2 % (w/v))	
DWL-15-GP7450		GP7450 (2 % (w/v))	

Results

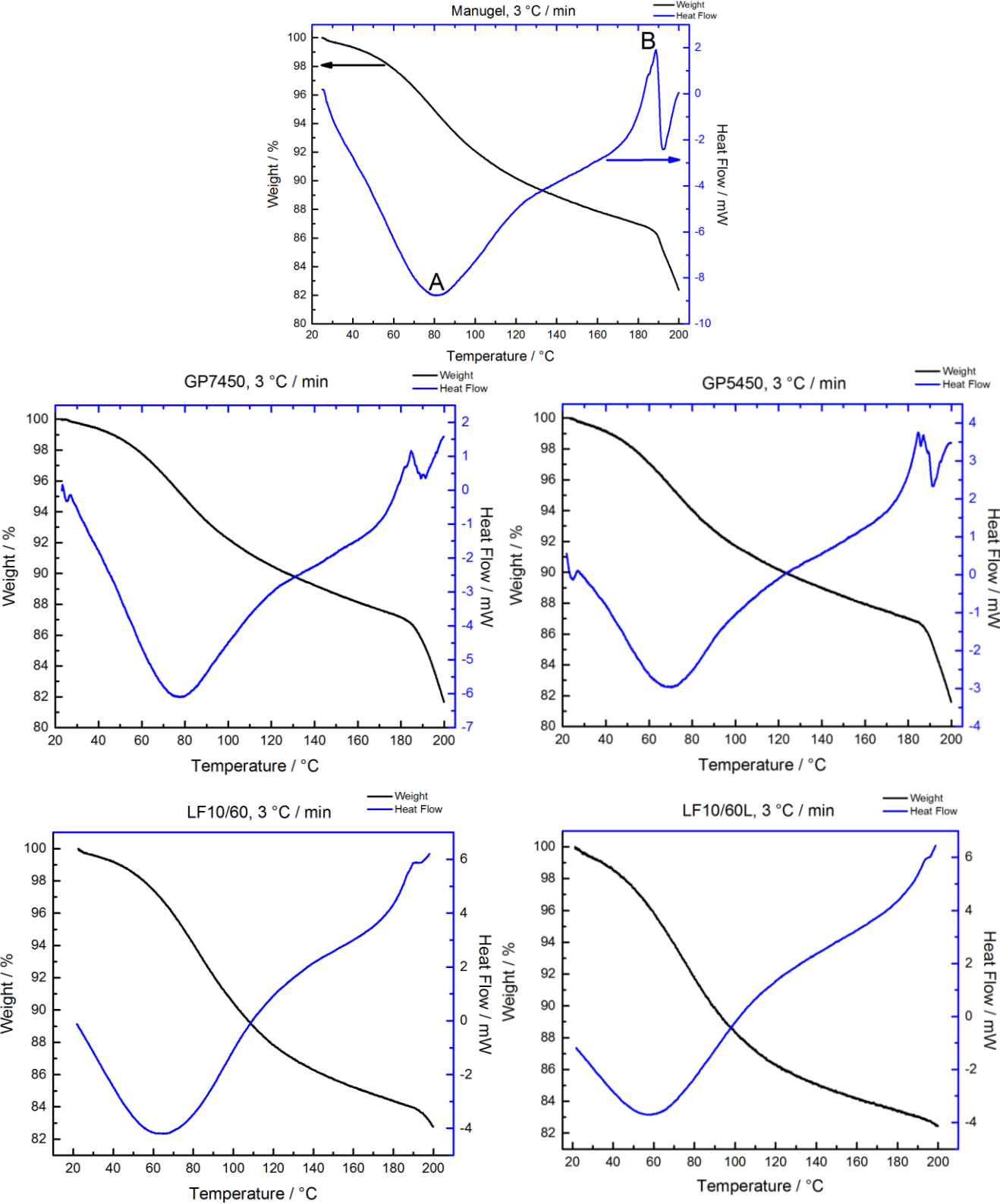


Figure 25: TGA on five different alginates gelled in the gelation solution of 2 % (w/v) $\text{CaCl}_2 \cdot 6 \text{H}_2\text{O}$. Heated from 23 °C to 200 °C at a rate of 3°C per minute. Point A in topmost figure indicates minimum heat flow and point B indicates the sudden drop in hear flow when mass of alginate decreases rapidly.

TGA-DSC was performed on the alginates. The results are shown in **Figure 25**. The weight loss pattern for GP7450, GP5450 and Manugel is similar; they lose weight gently until the temperature ~ 185 °C at which sudden weight loss occurred (point **B**). At that temperature the heat flow decreased slightly before it increased again. Sudden weight loss and slight decrease in heat flow combined may indicate the pyrolysis of a fraction of calcium alginate according to Zhang *et al.* The group reported that the first step in weight loss of Ca-alginates occurs in the temperature range 50 – 210 °C which corresponds to water desorption and the destruction of glycosidic bonds. This proposed thermal pyrolysis mechanism in early stage is shown in **Figure 26**. LF10/60 and LF10/60L, unlike three other alginates, did not show a clear, sudden decrease in heat flow. Their weight loss occurred at a relatively faster pace.

Weight losses of all alginates at three temperatures (120 °C, 135 °C and 150 °C) are summarized in **Table 9**. Point **A** in **Figure 25** indicates the least heat flow and the position of point A depends on the heat rate during the measurement. At low heat rate, position of point A shifts to left, and it shifts in the opposite direction at high heat rate. Point A in **Figure 51** (a) is positioned at lower temperature than topmost graph (both graph based on Manugel alginate) in **Figure 25**. This phenomenon is called thermal lag. It should be noted that even if there is a noticeable difference in positioning of point **A**, the point **B** is present at both heat rates.

Even though the measurement was supposed to be conducted in oxygen-free environment as described in **Section 2.5.3**, it was found that the environment contained some oxygen (approximately 6 %). This could have led to a fraction of alginate was burned at elevated temperatures. After the peak (point A; least heat flow in **Figure 25**), which can be attributed to the dehydration, exothermic reaction takes place. For GP5450, GP7450 and Manugel, the point A is at the temperature 70.3 – 80.6 °C whereas the peak occurred at lower temperatures (59.9 – 62 °C) for LF10/60 and LF10/60L.

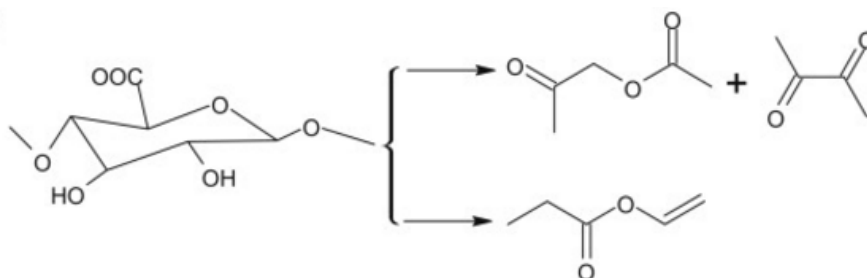


Figure 26: Proposed pyrolysis mechanisms for calcium alginate by J. Zhang et

..1 3

However, pyrolysis at relatively low temperature (up to 200 °C) might seem strange. Another explanation for this TGA-DSC data can be the restructuring of calcium alginate. This is a known phenomenon in polymers. One way to test this hypothesis is to heat the material at constant temperature and look at DSC data. This experiment was conducted in **Section 3.5**.

Table 9: TGA data on five different alginates in **Figure 25**. Weight losses at three temperatures are tabulated below. The temperature at point A is shown.

	Minimum heat flow at [°C]	% Weight loss at 120 °C	% Weight loss at 135 °C	% Weight loss at 150 °C
Manugel	80.6	9.8	10.8	11.6
GP7450	77.8	10.5	10.5	11.3
GP5450	70.3	9.8	10.7	11.5
LF10/60	62	12.2	13.4	14.3
LF10/60L	59.9	13.7	14.7	15.4

The average crushing strength of DWL-15 beads with different alginates is shown in **Figure 27**. The average crushing strength of DWL-15-LF10/60 and DWL-15-LF10/60L decreased significantly with increasing activation temperature; from 120 °C to 135 °C. Lower thermal stability of LF10/60 and LF10/60L alginates was observed in TGA-DSC data as well, and this phenomenon might be due to lower molecular weight as reported for other polymers such as PVC⁵⁵ and polycarbonates.⁵⁶

The average crushing strength of Manugel beads after activation is slightly higher than GP7450 and GP5450 with slightly higher molecular weight. That can be explained by the structural difference between them; M:G composition for Manugel is 40:60 whereas it is 45:55 for GP5450 and Gp7450. Since only G-blocks in alginate molecules are believed to participate in intermolecular crosslinking to form hydrogels, beads are stronger when formulated using alginates with higher G-block content. This phenomenon was observed from comparing DWL-15-LF10/60L beads with DWL-15-LF10/60 beads. The G-block content is much higher in alginate LF10/60 than in LF10/60L; yielding stronger beads.

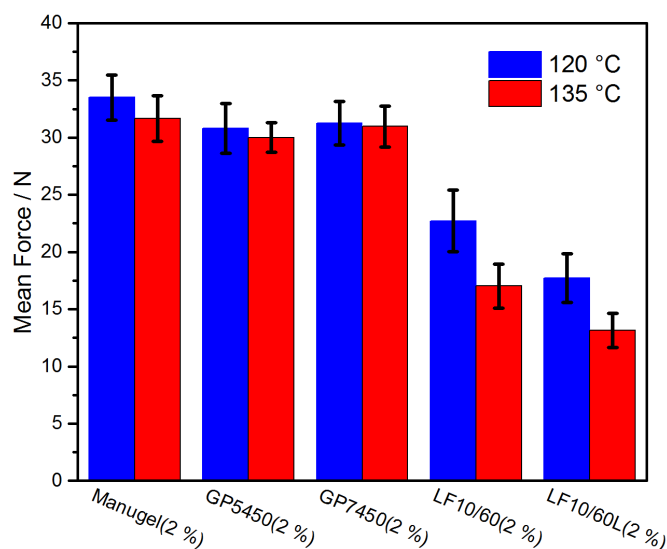


Figure 27: The average force applied on DWL-15 beads formulated using different alginates before they broke. Numbers in parenthesis corresponds to the alginate concentration. Activation temperature before the crushing strength measurement were 120 °C (blue bars) and 135 °C (red bars).

Conclusion

TGA-DSC results alone cannot determine the thermal stability of different alginates. Decrease in weight loss as well as the increase in heat flow may be associated with the following:

- 1) Partial decomposition of alginates
- 2) Restructuration of calcium alginate

Alginates with higher average molecular weight and higher G-block content is crucial for making strong beads. There seems to be a correlation between the molecular weight of alginate molecules and thermal stability. Better thermal stability allows beads to be activated at higher temperature and for longer activation time. MOF beads with Manugel alginate were slightly stronger than GP7450 and GP5450. However, GP7450's performance was best in terms of the difference in force between two temperatures employed. From this work, it can be concluded that Manugel, GP5450 and GP 7450 alginate suits better than LF10/60(L) with low molecular weight for formulation.

3.2. Effect of Alginate Concentration

Aim

Find out how the alginate concentration of the solution affects the mechanical stability of the dry beads and how the increased alginate concentration is affecting the porosity of MOF.

Experimental

The MOF powder (UiO-66, batch SH-55) was added to pre-measured (10 mL) distilled water. The solution was stirred shortly and sodium alginate powder (GP7450 and Manugel) was subsequently added. The quantity of chemicals used is tabulated in **Table 10**. MOF/alginate slurry was stirred at room temperature for approximately 60 minutes. The stirred solution was then added to the gelation bath drop by drop using a pipette tip. The gelation bath was prepared by dissolving 2 % (w/v) of $\text{CaCl}_2 \cdot 6\text{H}_2\text{O}$ in distilled water. Gelling time was 30 minutes. Beads were subsequently washed with distilled water three times for 10 minutes to remove the excess amount of calcium ions and chloride ions in the beads. Washed beads were dried at 60 °C in an air oven overnight. Dried beads were activated at 150 °C for 3 hours under vacuum in order to remove water inside the pores and crosslinked polymer network of the binder material before the measurements.

Table 10 The quantity of each substance used in producing beads in this work.

Sample	Alginate Conc. [% (w/v)]	Water [mL]	Alginate powder [mg]	MOF powder [g]	MOF content (dry) [wt%]
DWL-5	0.50	10	50	2.0	97.6
DWL-2	1.00	10	100	2.0	95.2
DWL-7	0.45	10	45	1.0	95.7
DWL-8	0.55	10	55	1.0	94.8
DWL-9-1.1%	1.11	10	111	1.0	90.0
DWL-9-1.4%	1.43	10	143	1.0	87.5
DWL-9-1.8%-Ca2%	1.80	10	180	1.0	85
DWL-16-M1.5%	1.50	10	150	1.35	90

Results and Discussion

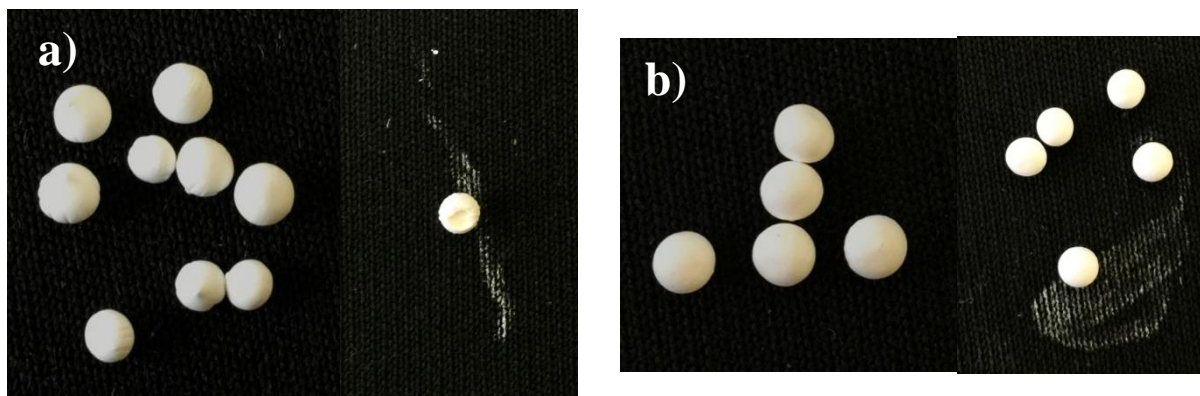


Figure 28: DWL-7 (a) and DWL-8 (b) with alginate (GP7450) concentrations of 0.45 % (w/v) and 0.55 % (w/v), respectively.

It was found that DWL-5 with alginate concentration of 0.50 % (w/v) was tear-shaped at all gelation distances. DWL-7 and -8 were made in order to determine the minimum amount of alginate needed to encapsulate the MOF material and to get spherical beads; not tear-shaped ones. With alginate GP7450, the minimum concentrations was approximately 0.45 % (w/v) to barely form a thin layer on the bead surface. However, the dried beads are tear-shaped and have wrinkles which were formed by shrinkage of beads during drying (a in **Figure 28**). When the concentration was increased to 0.55 % (w/v), the tip started to disappear and became more spherical (b in **Figure 28**). Both DWL-7 and 8 had too thin layer and this too soft; the MOF powder inside fell off upon touching like a chalk. They were easily breakable.

The strength of beads was increased proportionally to the alginate concentration as shown in **Figure 29**. Beads with higher strength (i.e. DWL-16-M2.0% in **Table 11**) were significantly less vulnerable to scratch, though not completely. One explanation for this vulnerability is that there is an upper limit of the hardness of alginates.

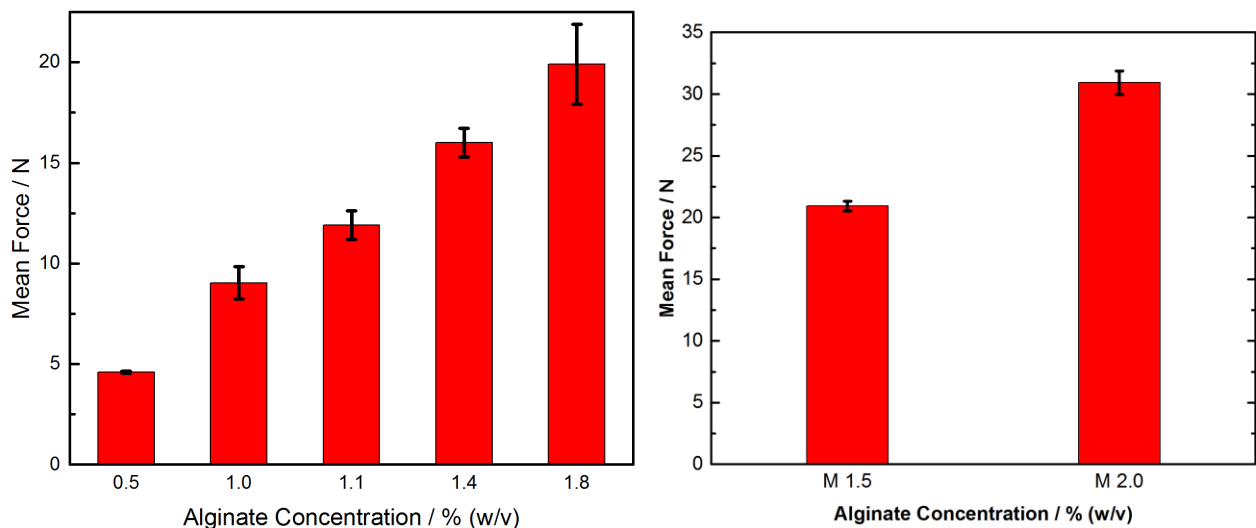


Figure 29: The mean force applied on beads with different alginate concentration to crack them. The data on the left hand side and right hand side was obtained from the beads formulated with GP7450 alginate and Manugel alginate, respectively.

Table 11: Numerical data in **Figure 29**.

	Alginate [% (w/v)]	Mean Force [N]	Mean Size [mm]
DWL-5	GP7450 (0.5)	4.60 ± 0.06	2.61
DWL-2	GP7450 (1.0)	9.03 ± 0.80	2.54
DWL-9-1.1%	GP7450 (1.1)	11.91 ± 0.71	2.75
DWL-9-1.4%	GP7450 (1.4)	16.04 ± 0.71	2.71
DWL-9-1.8%-Ca2%	GP7450 (1.8)	19.90 ± 1.98	2.77
DWL-16-M1.5%	Manugel (1.5)	16.53 ± 0.40	2.74
DWL-16-M2.0%	Manugel (2.0)	24.43 ± 0.95	2.93

The values in **Table 11** are plotted in **Figure 26**. The experimental values in this selected region suggest that there is a linear correlation between the alginate concentration and the mechanical strength.

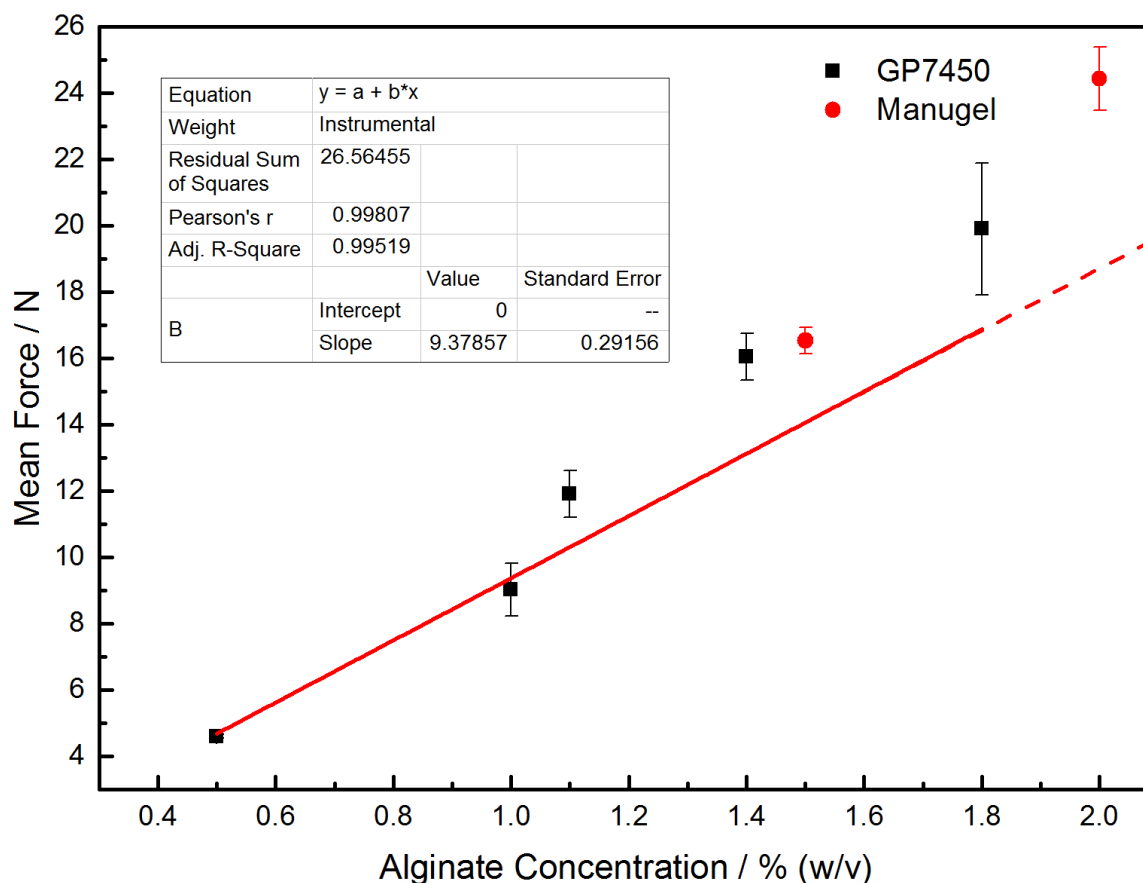


Figure 30: Mean force values plotted as a function of alginate concentration. Two different alginates used (black; GP7450, red; manugel). Linear fitting is used (for GP7450 data points) with forced interception at 0.

Except for DWL-2, other data points have greater value than linear regression line. If we take the first data point (DWL-5) as a reference point that is located on the trendline, all the other beads except for DWL-2 are stronger than what would have been if DWL-5 had higher alginate concentration. The difference is summarized in **Table 12**.

Table 12: The difference between the expected value from the linear fitting and the experimental values.

	Expected Value from the fitting [N]	Experimental Mean Force without std error [N]	Deviation
DWL-5	4.69	4.60	-1.9 %
DWL-2	9.38	9.03	-3.7 %
DWL-9-1.1%	10.32	11.91	+15.4 %
DWL-9-1.4%	13.13	16.04	+22.2 %
DWL-9-1.8%-Ca2%	16.88	19.90	+17.9 %
DWL-16-M1.5%	14.07	16.53	+17.5 %
DWL-16-M2.0%	18.76	24.43	+30.2 %

One of the possible explanations is that since the alginate is dispersed throughout the bead, the contribution from the inside, not only from the outer shell, to withstand the applied stress is greater as the total amount of alginate increases. Insoluble calcium alginate is acting like a hollow three dimensional framework throughout the bead.

Secondly, the mean size of other beads is bigger than that of DWL-5. This means that the volume of each bead is bigger; more alginate is to withstand the stress per bead as mentioned in the paragraph above. This effect was investigated further in **Section 3.6**.

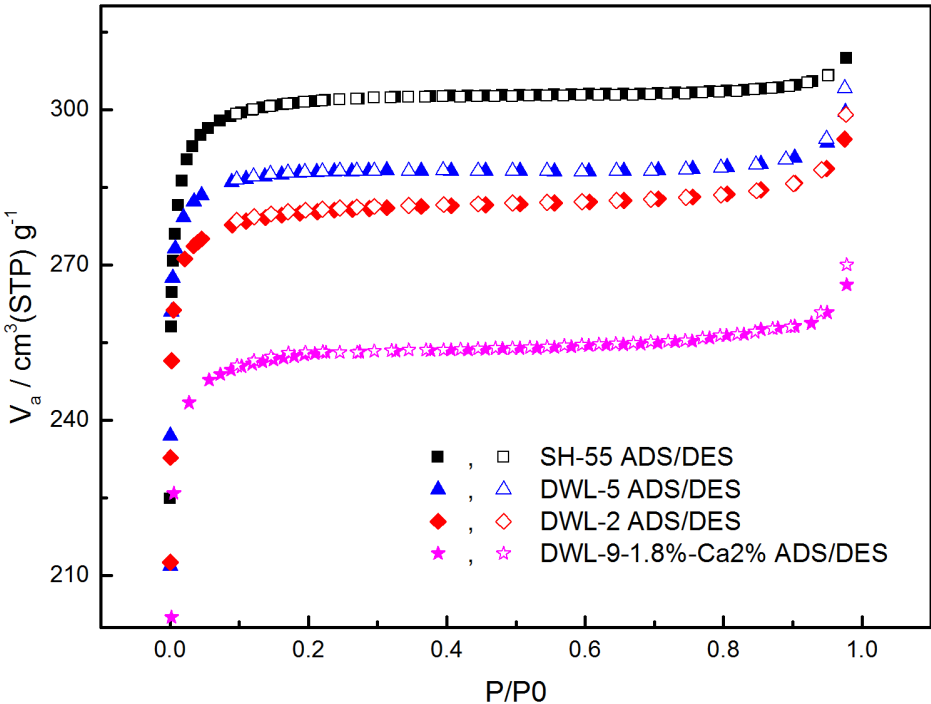


Figure 31. Adsorption/desorption isotherms of three samples. Isotherms for unformulated powder are shown as a reference value.

The volumetric N_2 uptakes at P/P_0 for SH-55 (black square), DWL-5 (blue triangle), DWL-2 (red diamond) and DWL-9-1.8%-Ca2% (purple star) in **Figure 31** are 302.77, 288.13, 281.77, and 253.90, respectively. The calculation of the decrease in nitrogen isotherms is given in **Appendix 7.2**.

Assuming that calcium alginate in the beads does not contribute to the nitrogen uptake, the theoretical nitrogen isotherms should be equal to the values of N_2 isotherm of powder

multiplied by the dry MOF content in **Table 10**. The expected values and the measured values of tested samples are summarized in **Table 13**.

Table 13: Comparison between the expected decrease in N₂ isotherms and the measured value at $p/p_0 = 0.5$.

	MOF content (dry) [wt%]	Expected decrease in N ₂ isotherms [%]	Measured decrease in N ₂ isotherms [%]	BET [m ² g ⁻¹] (Decrease %)
SH-55	100	--	--	1241 (--)
DWL-5	97.6	2.4	4.8	1191 (4.0)
DWL-2	95.2	4.8	6.9	1160 (6.5)
DWL-9-1.8%-Ca2%	85	15	16.1	1029 (17.1)

The difference between expected values and measured values does not seem to be related to the structural defects in the material since the difference is small. The decrease in BET surface area looks also reasonable. Several possible explanations account for this small

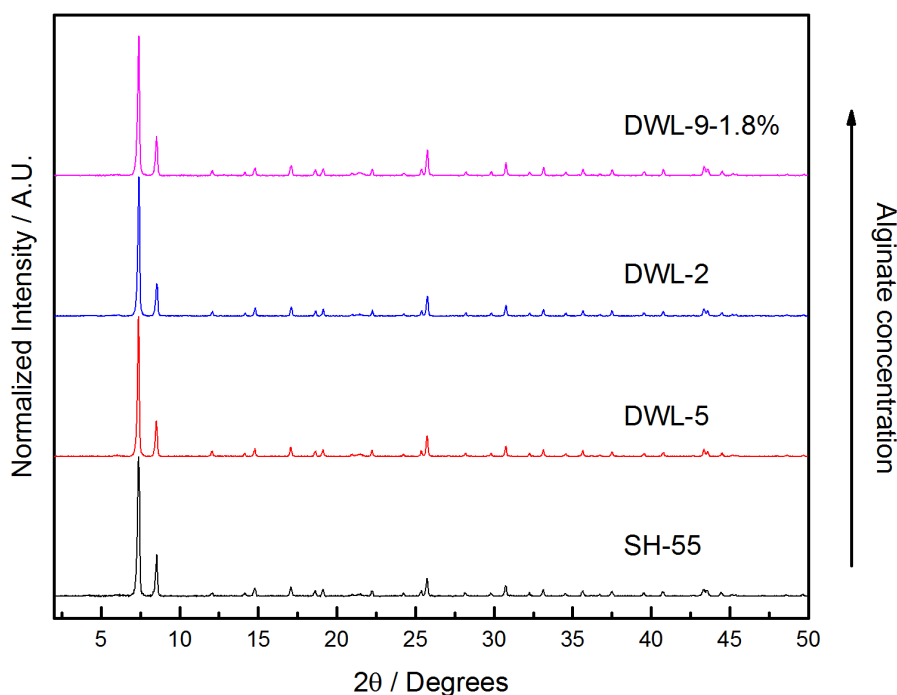


Figure 32: PXRD data of samples with varying alginate (GP7450) concentration. SH-55 (0 %), DWL-5 (0.5 %), DWL-2 (1.0 %), DWL-9-1.8%-Ca2% (1.8 %).

difference; 1) the water inside the beads or/and 2) excess amounts of calcium ions and chloride ions that had not been fully washed away during the washing procedure. EDX

analysis on the samples with various washing time (no wash, 10 minutes, 15 minutes and 90 minutes) in **Appendix 7.5.1** shows that the concentration of calcium ions and chloride ions decreased as washing time increased as summarized in **Table 14**.

Table 14: The concentration of Ca, Cl ions in beads with various washing times.

Washing time [min]	Avg. concentration of Ca / Cl –ions [at %, approximate value]	Avg. Zr concentration [at %, approximate value]	Ca:Zr ratio
0	8 / 8	85	0.0941
10	7 / 7	85	0.0824
15	6 / 6	90	0.0667
90	5.0 / 3.5	80	0.0625

This data was obtained from beads (DWL-17-gel180). The ion concentrations were much higher at the outer layer of beads that were washed for 10 minutes or not washed at all. This could mean that these accumulated ions were not washed away. This phenomenon was not observed for the beads washed longer.

A unit cell of UiO-66 consists of $Zr_{24}O_{16}(OH)_{16}BDC_{24}$. Dry MOF content was 90 wt% relative to the amount of alginate. A unit cell of sodium alginate consists of $C_6H_9NaO_7$. It is assumed that the UiO-66 was ideal without any defects and two sodium ions were replaced by one calcium ion. Ca:Zr ratios for beads decreased from 0 to 90 minutes of washing time. Calcium ions were believed to be released from the alginate beads into the surrounding solution, and it seems there is a correlation between initial calcium ion release and the water exposure time. It can be due to ion exchange with sodium ions nearby⁵⁷. Ca:Zr ratio became lower than the calculated value when beads were washed longer than 15 minutes. This may affect the crushing strength of beads since there are less “chemical bridges” between polymer chains. All the beads retained its shape after washing for 15 minutes or longer, but the crushing strength has somewhat reduced. It might be the result of the outer layer of beads, encapsulating calcium alginate shell, became thinner.

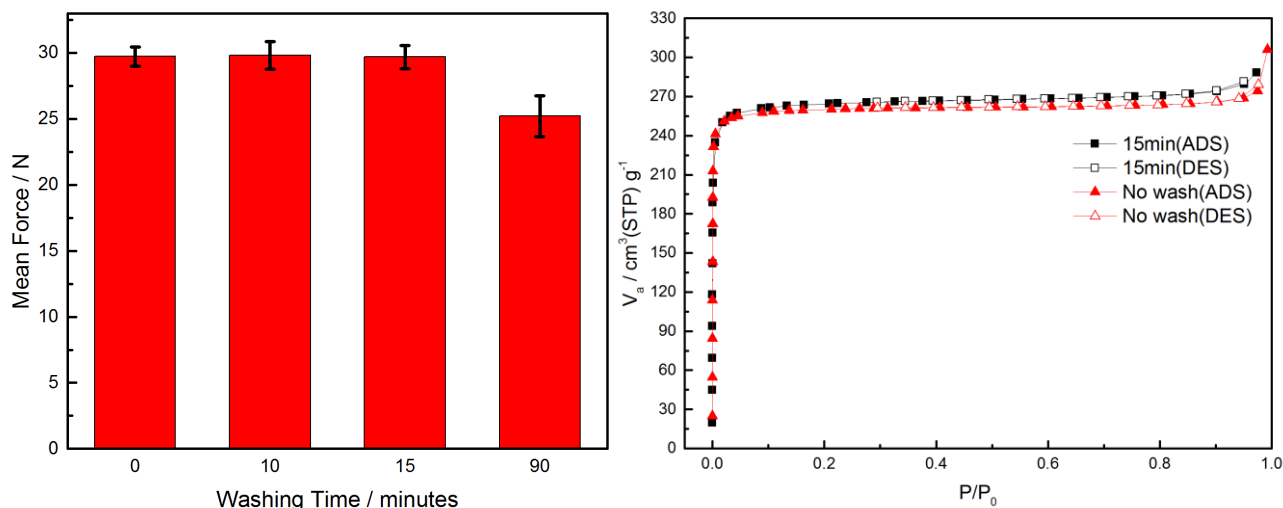


Figure 34: Average force applied before the beads were crushed plotted as a function of washing time (left) and Nitrogen sorption isotherm of unwashed and washed (15 minutes) beads.. Tested on DWL-17-Gel180 sample.

Accumulated calcium and chloride ions in the outer layer of unwashed beads did not affect the porosity as shown in **Figure 34**. It might be because of relatively small ionic sizes of Ca and Cl ions and N_2 is an inert gas. The isotherm also indicates that the excess calcium and chloride ions present in non-washed beads was not large enough affect the nitrogen isotherms (lower isotherms per unit mass).

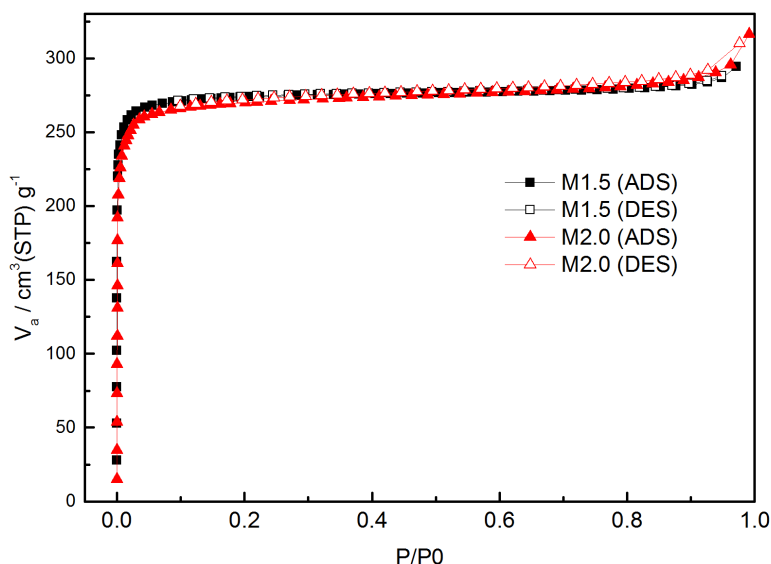


Figure 33: Nitrogen sorption isotherms for DWL-16-M1.5% and -M2.0%. Both samples have a dry MOF content of 90 wt% and were formulated with same alginate type (Manugel). Both N_2 isotherms are almost identical; an increase in alginate concentration does not affect the porosity.

Other samples were prepared; this time the dry MOF content was set to 90 wt% and only the alginate (Manugel) concentration was varied in order to confirm that the alginate does not affect the porosity. N₂ isotherms were slightly different; with higher amount of alginate, beads have less micropores and slightly more meso/macropores.

Table 15: The decrease in N₂ sorption isotherms and BET of DWL-16 samples relative to the powder.

	MOF content (dry) [wt%]	Expected decrease in N ₂ isotherms [%]	Measured decrease in N ₂ isotherms [%]	BET [m ² g ⁻¹]
SH-55	100	--	--	1241
DWL-16-M1.5%	90	10	9.4	1117
DWL-16-M2.0%	90	10	11.6	1084

Conclusion

Increasing alginate concentration (from 0.5 %(w/v) to 1.8 %(w/v) for GP7450 and from 1.5 %(w/v) to 2.0 %(w/v) for Manugel) is crucial for making strong beads. The increase in alginate concentration (in the same concentration range) did not negatively affect the MOF structure; both PXRD data and N₂ sorption measurement. However, one could not increase the alginate concentration and keep the dry MOF content at the same level simultaneously; in order to prepare a well-mixed MOF/alginate mixture, the viscosity of the mixture must be taken into account. Viscosity measurement results in **Appendix 7.8** shows that the viscosity of alginates increases quickly and thus makes it difficult to make a mixture in which alginate and MOF powder is homogeneously mixed.

The performance of non-washed beads was very similar to washed ones, though accumulation of Ca and Cl ions at the edge of beads was observed in elemental analysis shown in **Appendix 7.5.1**. It was expected that the excess amount of impurities such as Ca and Cl ions would decrease the thermal stability of beads because these ions could act as radicals and initiate the chain scission in alginate polymers at elevated temperatures. This phenomenon was not observed according to **Figure 34**. Beads that were washed longer than 15 minutes did not show the accumulation of Ca and Cl ions. Slight decrease in crushing strength was observed when the beads were washed for 90 minutes.

3.3. Effect of Calcium Ion Concentration

Aim

Investigate how the increasing concentration of Ca^{2+} ions during the gelation process contributes to the mechanical crushing strength of beads and investigate how the excess amounts of calcium ions and chloride ions influence the porosity of MOF.

Experimental

2.04 g of UiO-66 MOF powder was added to 20 mL distilled water and stirred for 20 minutes, and then 36 mg of GP7450 alginate was added while stirring. Beads were dropped into the gelation bath at a free fall distance of ~4 cm from the pipette tip to liquid surface. Experimental set-up used in this work is summarized in **Table 16**. “0.5 hrs” means the gelation time was 30 minutes. The gelation bath was prepared in different concentrations of $\text{CaCl}_2 \cdot 6\text{H}_2\text{O}$. Concentration of salt in gelation bath is given in the table. All samples were dried at 40 °C overnight in an air oven. Prior to any measurement, samples were activated at 150 °C for 2 hours in vacuum.

Table 16: Sample beads used in this experiment.

Sample	Batch (dry content)	Alginate type (concentration)	Conditions
DWL-9-1.8%-Ca0.2%			$\text{CaCl}_2 \cdot 6 \text{H}_2\text{O}$, 0.2 % (w/v), 0.5 hrs
DWL-9-1.8%-Ca0.5%			$\text{CaCl}_2 \cdot 6 \text{H}_2\text{O}$, 0.5 % (w/v), 0.5 hrs
DWL-9-1.8%-Ca1.0%	SH-55 (85 wt%)	GP7450 (1.8 % (w/v))	$\text{CaCl}_2 \cdot 6 \text{H}_2\text{O}$, 1.0 % (w/v), 0.5 hrs
DWL-9-1.8%-Ca2.0%			$\text{CaCl}_2 \cdot 6 \text{H}_2\text{O}$, 2.0 % (w/v), 0.5 hrs
DWL-9-1.8%-Ca5.0%			$\text{CaCl}_2 \cdot 6 \text{H}_2\text{O}$, 5.0 % (w/v), 0.5 hrs
DWL-9-1.8%-Ca10.0%			$\text{CaCl}_2 \cdot 6 \text{H}_2\text{O}$, 10.0 % (w/v), 0.5 hrs

Results and discussion



Figure 35: DWL-9-Ca0.2% (left), DWL-9-Ca0.5% (middle) and DWL-9-Ca2.0% (right).

The shape of beads was irregular when formulated in the gelation bath with low Ca^{2+} -ion concentration (0.2 % (w/v)) (**Figure 35**). This irregularity in shape disappeared when the calcium chloride concentration was increased up to 2.0 % (w/v). It is because the gelation kinetics was not fast enough to keep the regained shape (step IV in **Figure 10**) when the calcium ion concentration is too low. The rate of gelation was directly proportional to the concentration of calcium ions as reported.⁴⁵

When the concentration was above 5.0 % (w/v), the density of gelation bath was higher than the beads; the droplets floated on the surface before they sank as calcium ions and chloride ions in the gelation bath diffuse into the beads. It took approximately 30 seconds in the 5 % gelation bath and 150 secs in the 10 % gelation bath. This caused two main problems:

- 1) Tear-shaped beads
- 2) Low throughput

In this case, the gelation rate was so fast that some of beads formulated in the gelation bath did not have time to regain its shape after they had been deformed (step III in **Figure 10**).

As the less dense beads covered the whole surface of gelation bath and got close to each other, they formed “the neck” between them and clung to each other (**Figure 36**).



Figure 36 Tear-shaped beads of DWL-9-Ca10.0% (left). Three beads clung to each other (right).

The average applied force before breakdown on DWL-9-1.8%-CaX% beads formulated in six different gelation conditions is shown in **Figure 37**. The crushing strength of beads increased from 0.2 %(w/v) to 1.0 %(w/v) and it levels off in higher concentrations (after 1.0 %(w/v)). It was expected that the crushing strength of beads at a given gelation time would be proportional to the calcium ion concentration in the gelation process due to thicker outer layer. However, this was not observed, and it is considered to be due to low alginate concentration in each bead. Since the alginate concentration in each bead is very low, it does not need much calcium ions to saturate the anionic alginic acids (**Table 17**).

Lower crushing strength for beads formulated in low calcium chloride solution (0.2 %(w/v) and 0.5 %(w/v)) is considered to be due to the irregular shape of beads.

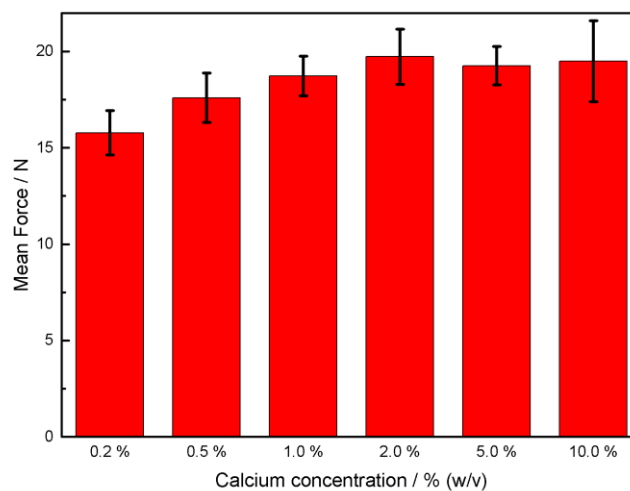


Figure 37: The mean applied force before breakdown on DWL-9 beads formulated in different calcium concentrations.

For DWL-9, the amount of calcium ions needed in the gelation is given in **Appendix 7.4**.

The ratio between the calcium concentration per bead and in the gelation bath is summarized in **Table 17**.

Table 17: Gelation bath of different concentrations of calcium ions used in this work. The ratio between the calcium concentration per bead and in the gelation bath is given. There is an excess amount of Ca^{2+} ions in every gelation baths. Visual sphericity and the average force applied on each bead are given.

CaCl₂·6 H₂O dissolved / %(w/v)	Ca²⁺ concentration [mol/L]	Ratio	Shape^c	Avg. Force [N]
0.2	9.13×10^{-3}	131.0	3	15.8
0.5	2.28×10^{-2}	327.1	2	17.6
1.0	4.56×10^{-2}	654.2	1	18.7
2.0	9.13×10^{-2}	1309.9	1	19.7
5.0	2.28×10^{-1}	3271.2	2	19.3
10.0	4.56×10^{-1}	6542.3	2	19.5

It is important to note that the calculations above assumed several things:

- 1) The volume of MOF/alginate-water mixture was constant
- 2) All the beads are perfectly spherical and has a uniform size

The ratio might vary, but the interesting thing here is that even though the initial calcium concentration in the 0.2 %(w/v) gelation bath is much higher than needed, most of beads formulated in that solution were deformed as shown in **Figure 35**. As mentioned above, the gelation kinetics was too low to keep the spherical shape at this ratio. Increasing the calcium ion concentration results in a larger concentration gradient between the inside of beads and the outside solution. This favors the diffusion of calcium ions into the core of beads at a faster rate.

^c 1: Spherical. 2: Less spherical. 3: Deformed (Non-spherical).

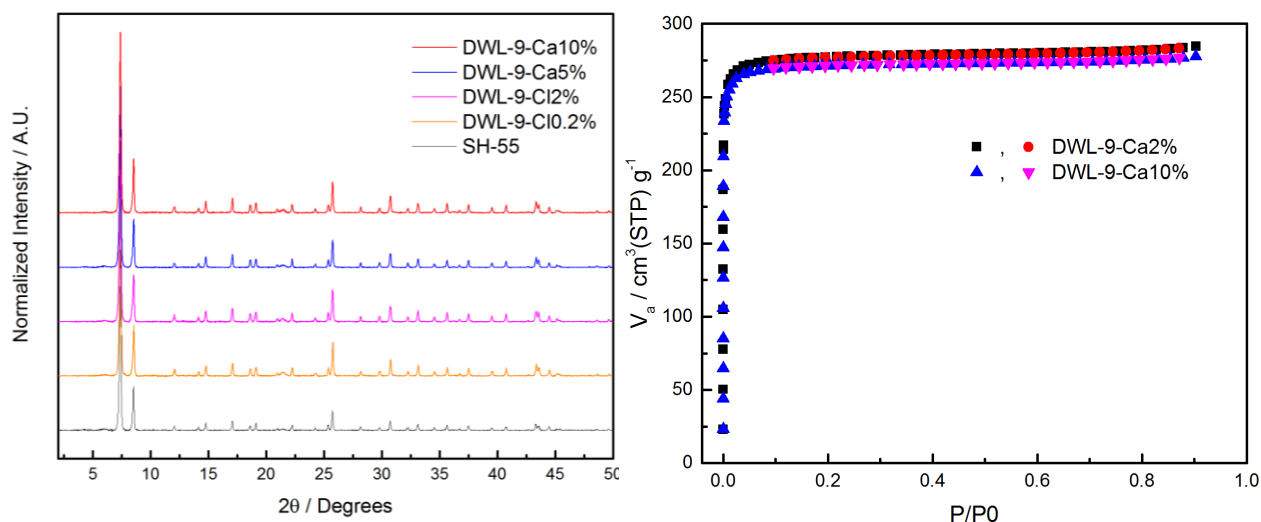


Figure 38: PXRD on UiO-66 powder (SH-55), DWL-9 gelled in gelation bath of different calcium chloride concentrations ranging from 0.2 % (w/v) to 10 % (w/v) (left). Nitrogen sorption isotherm on DWL-9 formulated in 2 % (w/v) and 10 % (w/v) calcium chloride gelation bath (right).

Despite the increasing calcium ion concentration, there is no noticeable change in neither PXRD-pattern nor nitrogen sorption isotherm. It is considered that calcium ions and chloride ions do not affect the MOF properties such as crystallinity and porosity.

Conclusion

Formulation in gelation bath of calcium chloride concentrations of 1-2 % (w/v) resulted in most spherical and robust beads. When the concentration was high (5-10 % (w/v) CaCl₂·6H₂O), beads stayed afloat before they sank. Floating is unfavorable to high throughput. Higher calcium concentration did not result in stronger beads. Lower (less than concentration of 1 % (w/v)) calcium concentration resulted in irregular shaped beads that are weaker. Increasing calcium chloride concentration did not affect the properties of UiO-66.

3.4. Effect of Gelation Time

Aim

Find out what effect gelation time has on the mechanical stability and porosity.

Experimental

Table 18. Main parameters used in this experiment.

MOF batch samples used (dry MOF content)	SH55 (90 wt%)
Alginate type (concentration)	Manugel (2 % (w/v))
Washing time	15 minutes
Drying condition	40 °C overnight (air)
Activation condition	135 °C for 2 hours (vacuum)
Gelation Bath	CaCl ₂ ·6 H ₂ O (2 % (w/v))
Gelation Time [min]	3, 5, 10, 15, 30, 60, 120, 180, 270, 840

Beads with varying gelation time were made (DWL-17). Gelation time was varied from 3 minutes to overnight (ca. 14 hours). Every other parameter was kept constant; as given in **Table 18**. 4 to 5 beads of similar shape and size from each prepared sample were selected for the measurement.

Crushing strength and gas sorption isotherms were measured. EDX measurement was conducted for 3 min, 15 minutes and overnight samples.

Results

The average crushing strengths are shown in **Figure 39**. It was highest for 3 min samples and decreased a little since then. However, 3 min and 5 min samples were not perfectly spherical; they were more flat on the side which touched the floor during the air drying. This indicates that the gelation time was so short that the degree of cross-linking for those samples was not sufficient to maintain the bead framework. Bead samples that were exposed to gelling solution for 10 minutes or longer were more spherical.

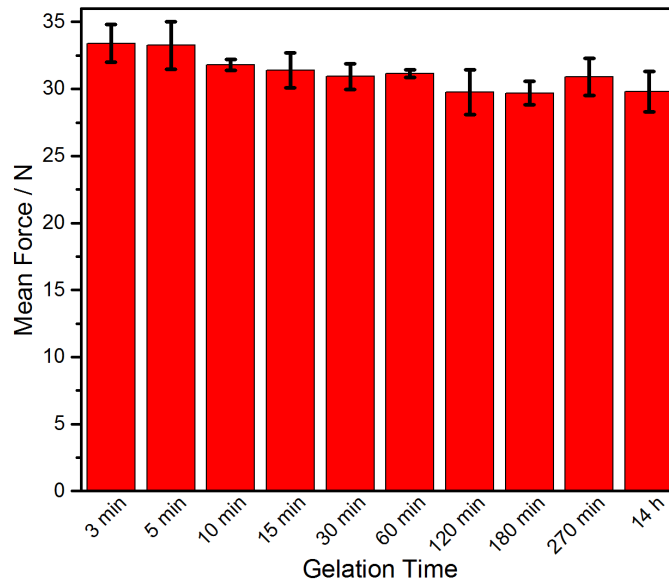


Figure 39. Average applied force before breakdown as a function of time. The effect of gelation time.

3 min and 14 hours beads do not differ much in sorption isotherms. It indicates that higher sodium ions for 3 min beads do not affect anything (see **Appendix 7.5.2**). This is expected since sodium ions have smaller atomic radius than calcium ions.

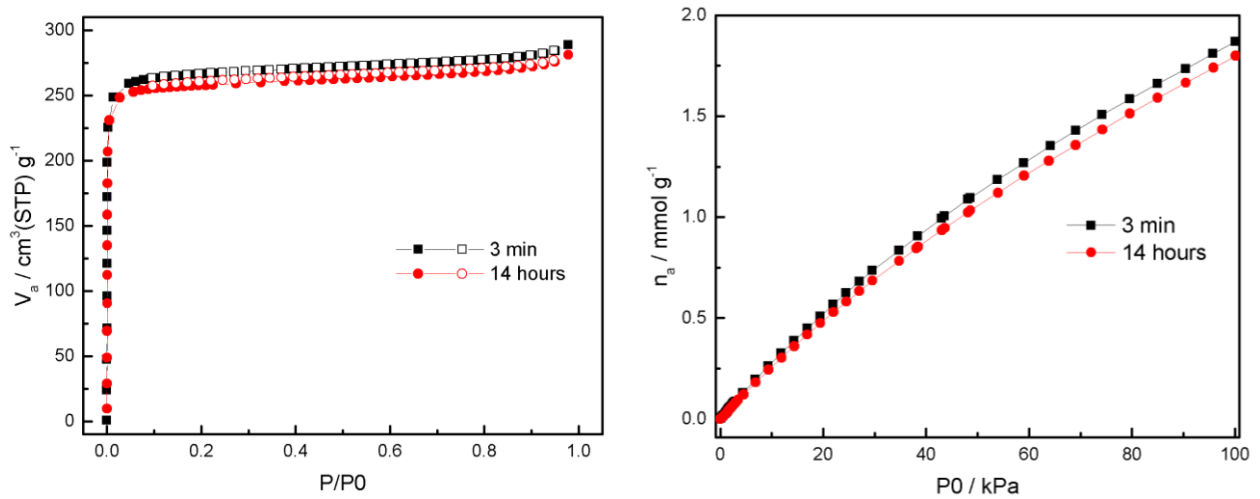


Figure 40: Nitrogen sorption isotherm (left) and CO₂ uptake (right) on DWL-11.

Conclusion

The shape of dried beads depends on the gelation time. The beads that were exposed to the gelation solution (2 % (w/v) of $\text{CaCl}_2 \cdot 6 \text{H}_2\text{O}$ dissolved) for less than 5 minutes, they were more cylindrical whereas other beads with gelation time longer than 10 minutes were more spherical. The contact area of the piston and the cylindrical beads is higher than with a single point in spherical beads. The crushing strength was more or less constant within the time range in this work (10 minutes - 14 hours). Even if there was a difference in composition between beads with varying gelation time as seen in **Section 7.5.2**, the gas sorption isotherm was almost identical. It can be concluded that the gelation time of 10 minutes or longer is sufficient for formulation.

3.5. Effect of Activation Temperature and Time

Aim

Find the optimal activation temperature for MOF beads.

Results and discussion

An IR spectrum of unformulated powder activated at 150 °C was used as a reference.

The IR spectra reported in **Figure 41** summarizes the progressive dehydration of DWL-9-1.8%-Ca2%. Panels (a) and (c) refer to the OH stretching modes.

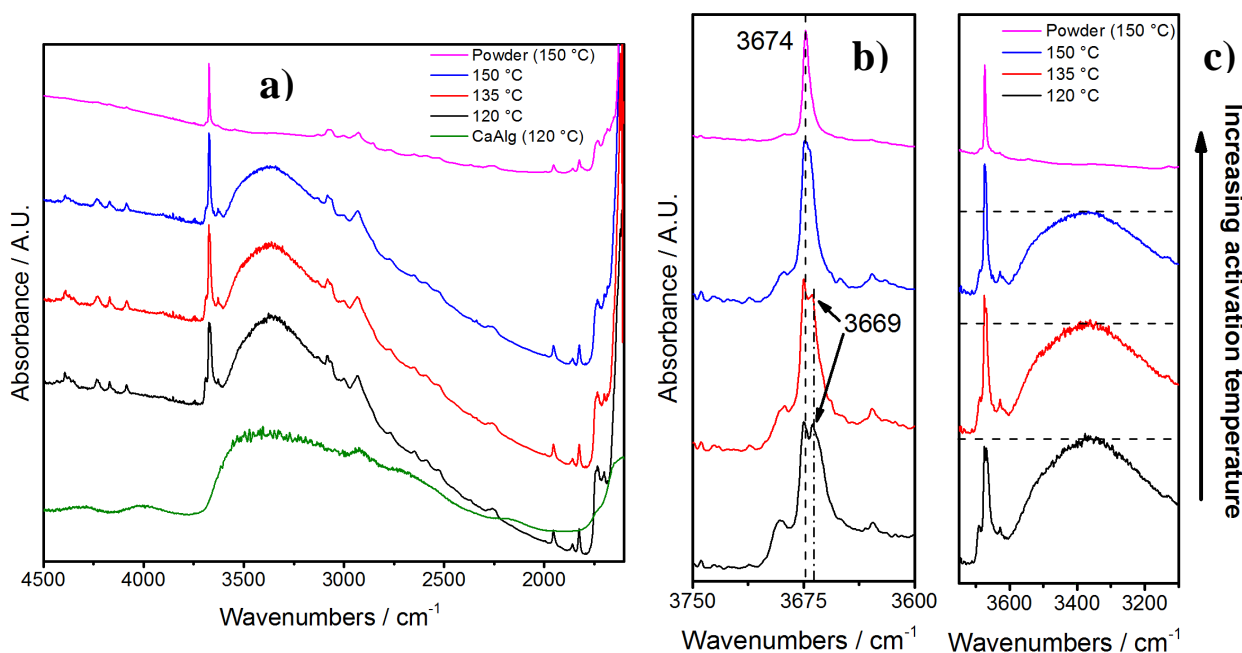


Figure 41: The IR spectrum of batch powder SH-55 (purple), DWL-9-1.8%-Ca2% (black, red and blue) and alginate GP7450 (green).

The spectrum of DWL-9-Ca2% in panels (a) and (c) is dominated by an intense and broad band centered at 3380 cm^{-1} due to OH stretching modes that belong to water and the alginate. For UiO-66, the band in this region refers to the intercrystallite physisorbed water condensed inside the crystal cavities.³⁷ The peak at 3674 cm^{-1} corresponds to a small fraction of isolated OH groups present on the external surfaces of the microcrystals. The effect of higher activation temperature removes more water in the material and results in relative decrease of the broad band centered at 3380 cm^{-1} and an increase in intensity and sharpness of the peak

due to isolated OH groups. Unlike DWL-9-1.8%-Ca2%, the IR spectrum of UiO-66 activated at 150 °C for 2 hours, which is a common activation condition used at inGAP, shows no broad band around 3000-3600 cm^{-1} ; meaning that there is a few OH groups left in the material. However, the formulated bead activated in the same condition (blue curve) still possesses a broad band. This is considered to be due to both water and inherent OH-groups in the alginate molecules. The IR spectrum of alginate (green curve in (a)) has a broad band that overlaps quite well with the band observed in the formulated beads.

In panel (b), the peak at 3674 cm^{-1} becomes sharper upon higher activation temperature. Intense peak signal at 3669 cm^{-1} was observed at 120 °C and 135 °C and disappears at 150 °C. This phenomenon is not observed in the IR spectrum of pure UiO-66. This secondary peak may correspond to stretching mode of OH group in alginate molecules.

Figure 42 shows additional IR spectra of DWL-9-1.8%-Ca2%. The activation duration was varied while the activation temperature was set to 120 °C. The relative decrease upon longer activation duration was observed (dotted line in panel (b)), and is considered to be due to mainly the partial degradation of alginate according to the TGA data in **Figure 45**. Partial degradation of alginate is an exothermic process and it begins at relatively low temperature ~ 75 °C. This is what was observed in **Section 3.1**. The doublet peak, however, remained the same after 17 hours at 120 °C, and it might mean 120 °C was not high enough to desorb/degrade the isolated OH-groups from alginate molecules on the external surfaces of the microcrystals as mentioned above.

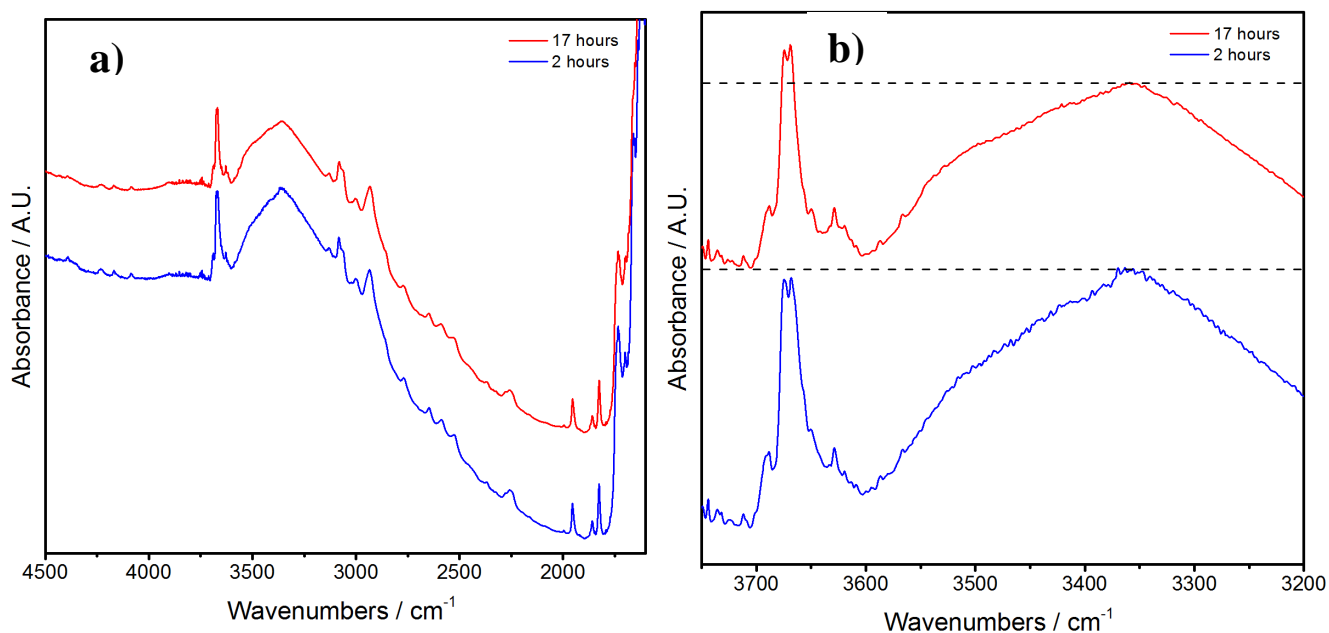


Figure 42: The IR spectrum of DWL-9-1.8%-Ca2% activated at 120 °C. The activation duration was varied in order to investigate the cause of the broad band centered at 3380 cm⁻¹. IR spectrum over the whole measurement range (a) and the ratio between the peak and

The weight loss of DWL-9-1.8%-Ca2% beads over longer period at three different temperatures was investigated. The weight loss after 900 minutes was 5.6 %, 9.0 % and 11.5 % at 120 °C, 135 °C and 150 °C, respectively. Once the measuring temperature was reached in each experiment, the weight loss occurred at a very slow rate. **Table 19** summarizes the results.

However, the weight loss difference between these temperatures seemed quite big compared to a detailed TGA in **Figure 45** which is the same curve (150 °C) in **Figure 43**. The weight loss difference between 120 °C and 150 °C (marked in **Figure 45**) is less than 1 % whereas the separate experiment showed a difference of 5.4 % (**Table 19**). This might be because the total water uptake by every single bead is inhomogeneous even though the beads consist of the same material.

For formulated UiO-66 with Ca-alginate as the binder material, the weight loss observed when heated to a relatively low temperature (~ 200 °C) can be related to:

- 1) Water inside the pores and the polymer matrix is desorbed
- 2) Polymer chain is cleaved (partial decomposition)

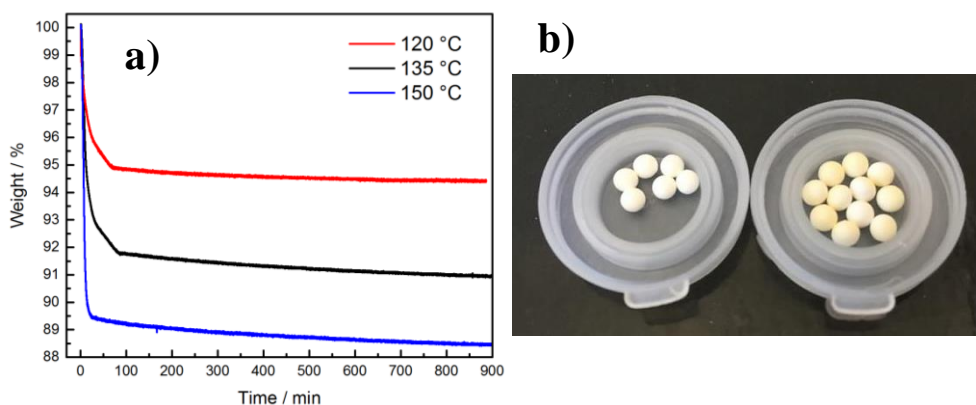


Figure 43: TGA results of DWL-9-1.8%-Ca% at three different activation temperatures (a). DWL-9-1.8%-Ca2% after activation at 150 °C (b): Left: Activated for 2 hours, Right: activation overnight.

Table 19: The weight loss of DWL-9-Ca2% at three different temperatures. Weight loss when the final temperature was reached and 12 hours after that point in each experiment are shown.

	Weight loss at the final temperature. (1)	Weight loss after 12 hrs since (1)
120 °C	5.0 %	0.6 %
135 °C	8.1 %	1.0 %
150 °C	10.4 %	1.2 %

The weight was consistently lost, though it was very slow, during the measurement time the heat was generated (**Figure 45**). The weight loss and positive DSC curve can be interpreted as a result of polymer restructuration; the more water lost the more

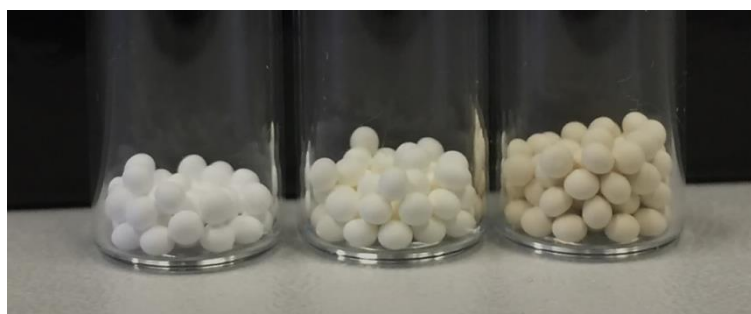


Figure 44: DWL-9-1.8%-Ca2% activated at three different temperatures (from left to right, 120 °C, 135 °C and 150 °C overnight). The color change might indicate the partial degradation of

rearrangements, thus heat generated. The color change in beads changed ((b) in **Figure 43** and **Figure 44**) might be a result of oxidation.

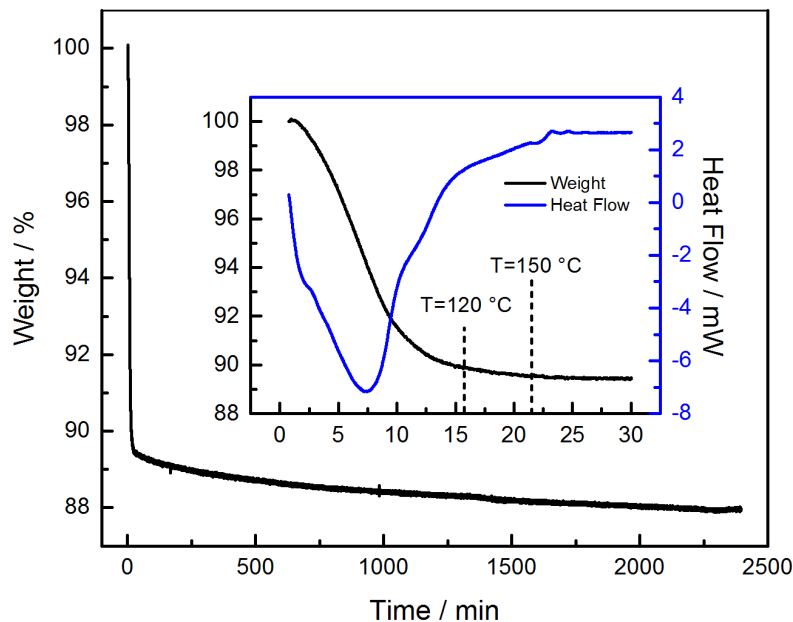


Figure 45: TGA data on DWL-9-1.8%-Ca2%. The beads were heated up to 150 °C and were left overnight. Smaller graph shows the weight loss and the heat flow during the first 30 minutes. The heat flow was lowest at ca. 75 °C and started to increase; exothermic reaction takes place. The time at which the temperature of 120 °C and 150 °C were reached are indicated.

Mechanical crush strength of one identical sample was measured after a set of different activation conditions. Note that the standard deviation in crushing strength of beads activated at 120 °C is bigger than that of beads activated at higher temperatures. That might indicate the sample beads were more structurally flexible (elastic) due to relatively higher water content in the beads. This could mean that activation temperature of 120 °C was too low to remove water. Lower mechanical crushing strength for longer activation time at same temperature might be a result of partial decomposition of the binder material. The difference in the average crushing strength between 120 °C and 135 °C was very small; indicating the alginate is quite thermally stable up to 135 °C. The average crushing strength decreased from 20.9 N to 16.2 N when the activation temperature was increased from 135 °C to 150 °C. This is 22.5 % decrease; more alginate was decomposed.

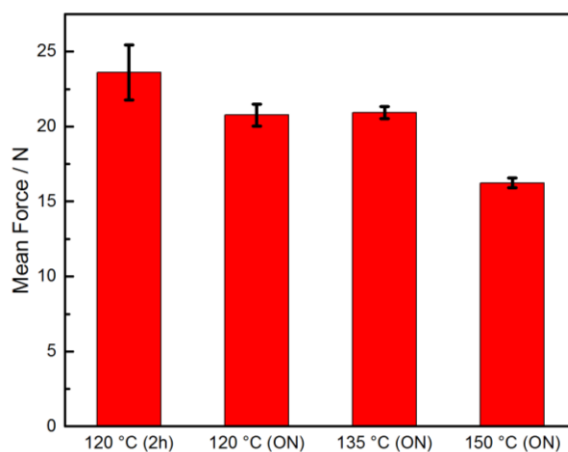


Figure 46: Average mechanical crushing strength of DWL-9-1.8%-Ca2% after 4 different activation conditions. From left: Activation at 120 °C for 2 hours, 120 °C overnight, 135 °C overnight, 150 °C overnight. Red bars illustrate the mean value and the error bars indicate the difference between the

Nitrogen sorption isotherm and CO₂ uptake were measured on DWL-9-1.8%-Ca2% with various activation temperatures. The results are shown in **Figure 47**. Activation time was 3 hours at 120 °C and 150 °C. Batch material SH-55 powder was also measured and is given as a reference value. The volume of nitrogen adsorbed is 303 cm³g⁻¹, 255 cm³g⁻¹, 253 cm³g⁻¹ for SH-55, DWL-9-1.8%--Ca2% (150 °C) and DWL-9 (120 °C), respectively. The decrease in volume is 15.8 % and 16.5 % and fits well with expected value since the dry MOF content in DWL-9-1.8%-Ca2% is 85 wt%. No significant difference between 120 °C and 150 °C was observed; indicating that the water physisorbed in the beads does not affect the porosity of the material. Since nitrogen is an inert gas that does not interact with OH groups in water molecules, CO₂ uptake measurement was conducted. However, the difference in CO₂ uptake between these two activation temperatures was not big (**Figure 47**).

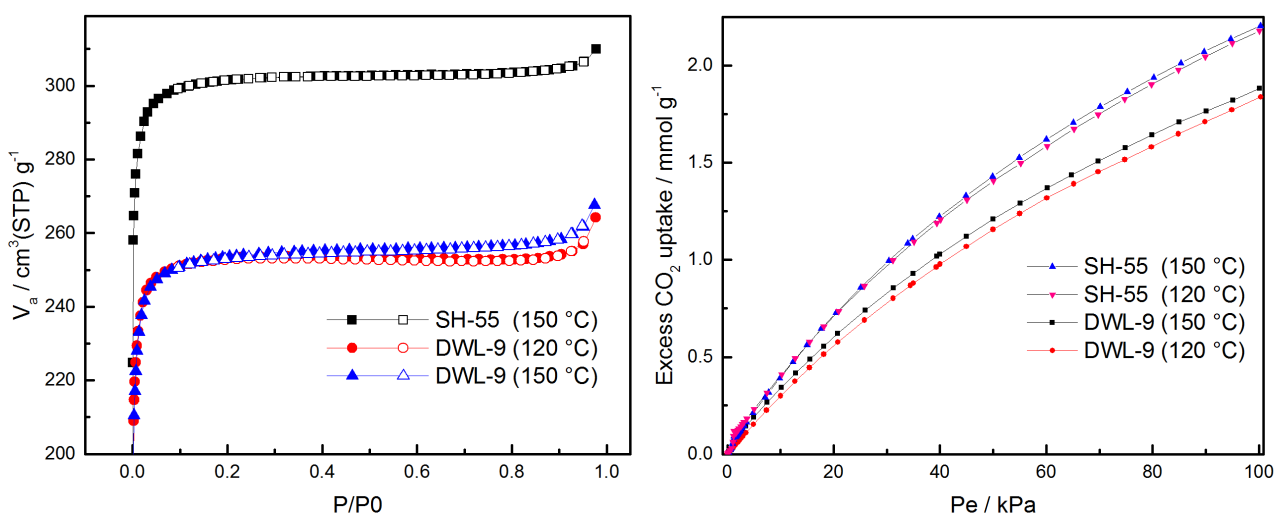


Figure 47: Nitrogen sorption isotherm (left) and CO_2 uptake (right).

Conclusion

The IR spectrum of beads activated at three different temperatures looked a bit different; the ratio between the peak (3674 cm^{-1}) and the broad band ($3000\text{-}3600 \text{ cm}^{-1}$). The shape of the peak was also different. That result suggested investigating the gas isotherms. However, there was no significant difference between samples (DWL-9 activated at $120 \text{ }^\circ\text{C}$ and $150 \text{ }^\circ\text{C}$) in terms of sorption isotherms; meaning that even though the IR spectrum looked different. That broad band was caused mainly by OH groups in alginate molecules that do not block the cavities in UiO-66.

The higher the activation temperature, the weaker the crushing strength of beads becomes. Since there is no difference in crushing strength between $120 \text{ }^\circ\text{C}$ and $135 \text{ }^\circ\text{C}$, the activation temperature of $135 \text{ }^\circ\text{C}$ is favored due to faster desorption of water in the beads. Since beads activated at $120 \text{ }^\circ\text{C}$ for 3 hours showed almost equal values in gas sorption isotherms as $150 \text{ }^\circ\text{C}$ for 3 hours, activation time at $135 \text{ }^\circ\text{C}$ can be lower than that due to faster water desorption at higher temperature..

3.6. Effect of Size of Beads

Aim

Determine what effect the particle size has on the mechanical stability, water removal inside the beads, and total uptake of CO₂.

Results and Discussion

Bead size is shown in **Figure 48**. The size of beads increased as the radius of tip increased as shown in **Table 20**.

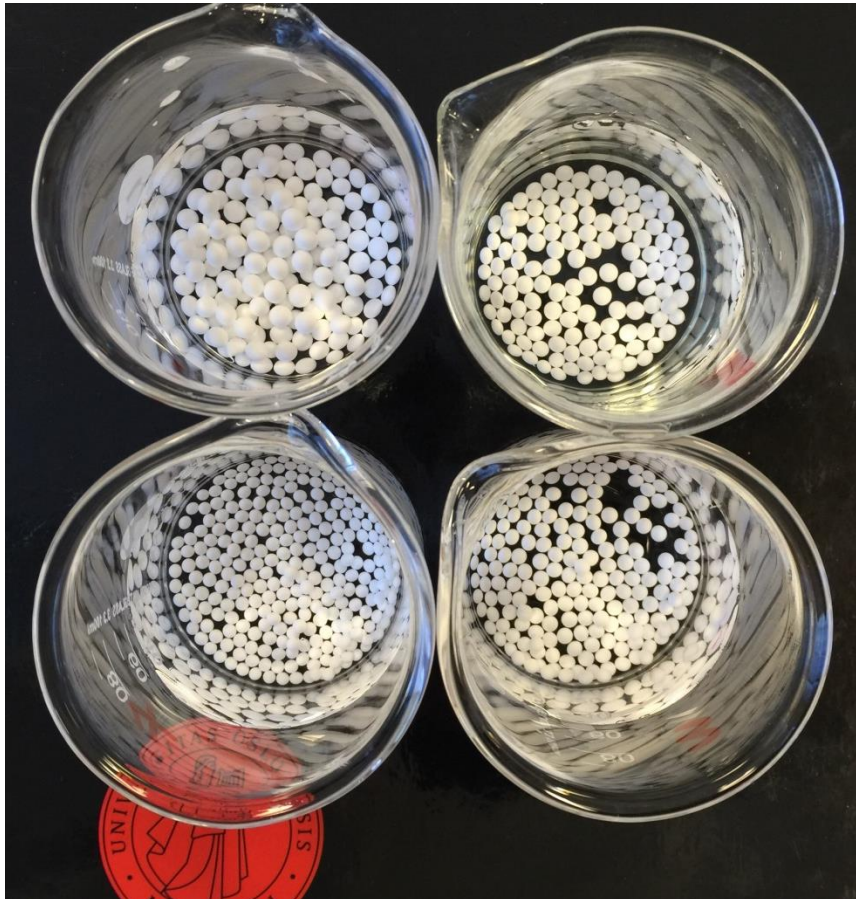


Figure 48: DWL-10 beads in four different sizes. Biggest beads (top-left) and smaller ones in clockwise order:

Table 20: Internal diameter of tip employed and the average size (with standard deviation) of beads produced.

Internal Diameter of the Tip [mm]	Average Size of Dried Beads [mm]
1.97	2.91 ± 0.02
0.98	2.42 ± 0.01
0.68	2.15 ± 0.02
0.35	1.84 ± 0.06

The average crushing strength increased significantly with the size of beads as shown in **Figure 49**. Fundamentally speaking, the contact area between the piston and a perfect sphere is always two points. Since the pressure is spread over a larger particle diameter (or volume), the overpressure in the whole structure is reduced. Hence, larger beads can withstand more force before breakdown.

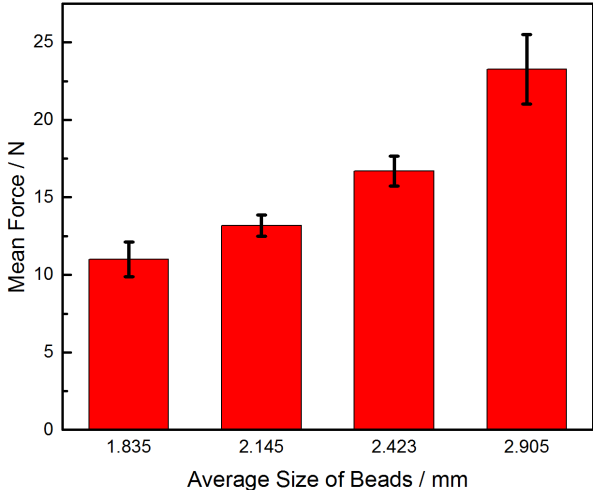


Figure 49: The average force applied on DWL-10 beads with four different sizes.

No noticeable difference in nitrogen and CO₂ isotherms observed between beads in different sizes. This indicates that even though the size becomes bigger so that the distance from the surface and core gets longer, it does not block the pores; the total uptake remains the same within the size range (1.835 mm to 2.905 mm) in this work.

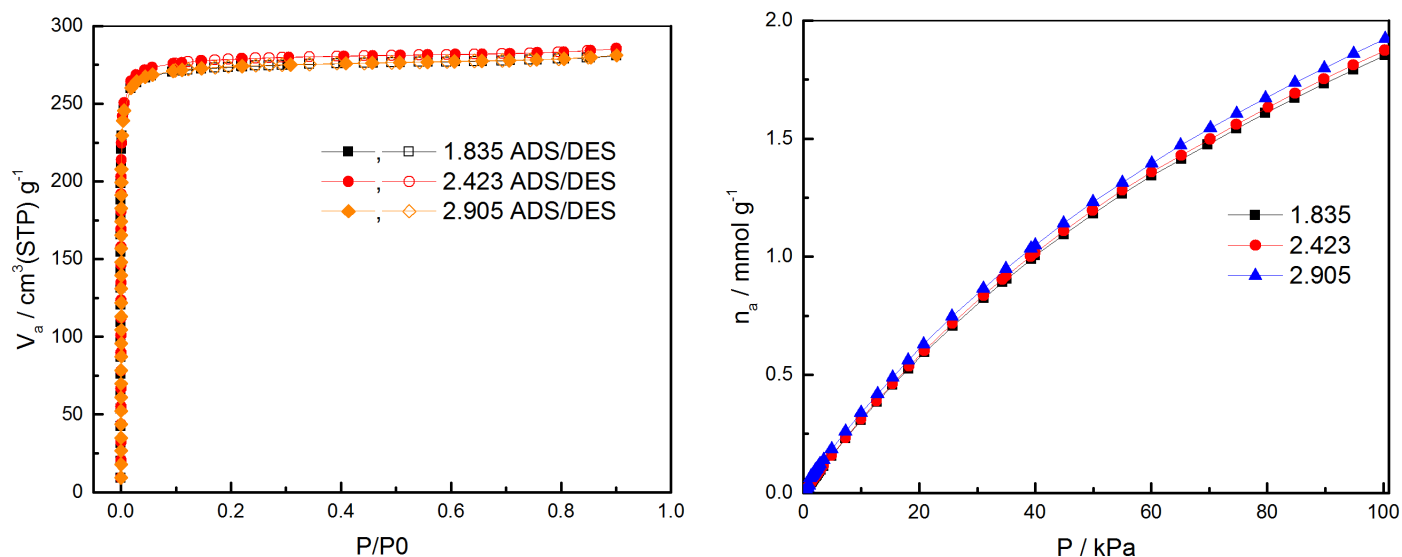


Figure 50: Nitrogen sorption isotherms (left) and CO₂ uptake (right) on beads in different sizes. The numbers correspond to the average diameter of beads used in this work.

Conclusion

Beads that are bigger in size could withstand more force without having to sacrifice the surface area and total CO₂ uptake. Bigger beads are favorable in industrial reactors due to reduced pressure drop. However, it is not clear how bigger size will affect the diffusion limitations. Diffusion limitation study was not conducted in this work due to lack of instruments.

3.7. Effect of Multivalent Cations and pH

Aim

The purpose of this experiment was to investigate how different multivalent cations affect the properties of beads.

Experimental

Table 21: Different cations and its source used in this work.

Ion	Source	Concentration in gelation solution
Ca ²⁺	CaCl ₂ ·6 H ₂ O	2 % (w/v)
Ba ²⁺	Ba(NO ₃) ₂	Corresponding amount of substance
Cu ²⁺	CuSO ₄ ·5 H ₂ O	
Al ³⁺	Al(NO ₃) ₃ ·9 H ₂ O	Corresponding amount of substance multiplied by 2/3
Cr(OH) ²⁺ , Cr ³⁺	Cr(NO ₃) ₃ ·9 H ₂ O	
Zr ⁴⁺	Zr(SO ₄) ₂ ·4 H ₂ O	Corresponding amount of substance multiplied by 1/2
	ZrOCl ₂ ·8 H ₂ O	
	ZrO(NO ₃) ₂ ·x H ₂ O	

All the beads (DWL-13 and DWL-14) in this work were dried at 40 °C in air and activated at 135 °C for 2 hours. N₂ and CO₂ sorption isotherm were measured.

TGA-DSC was performed to investigate the thermal stability of alginates (Manugel) formulated various cations.

Results

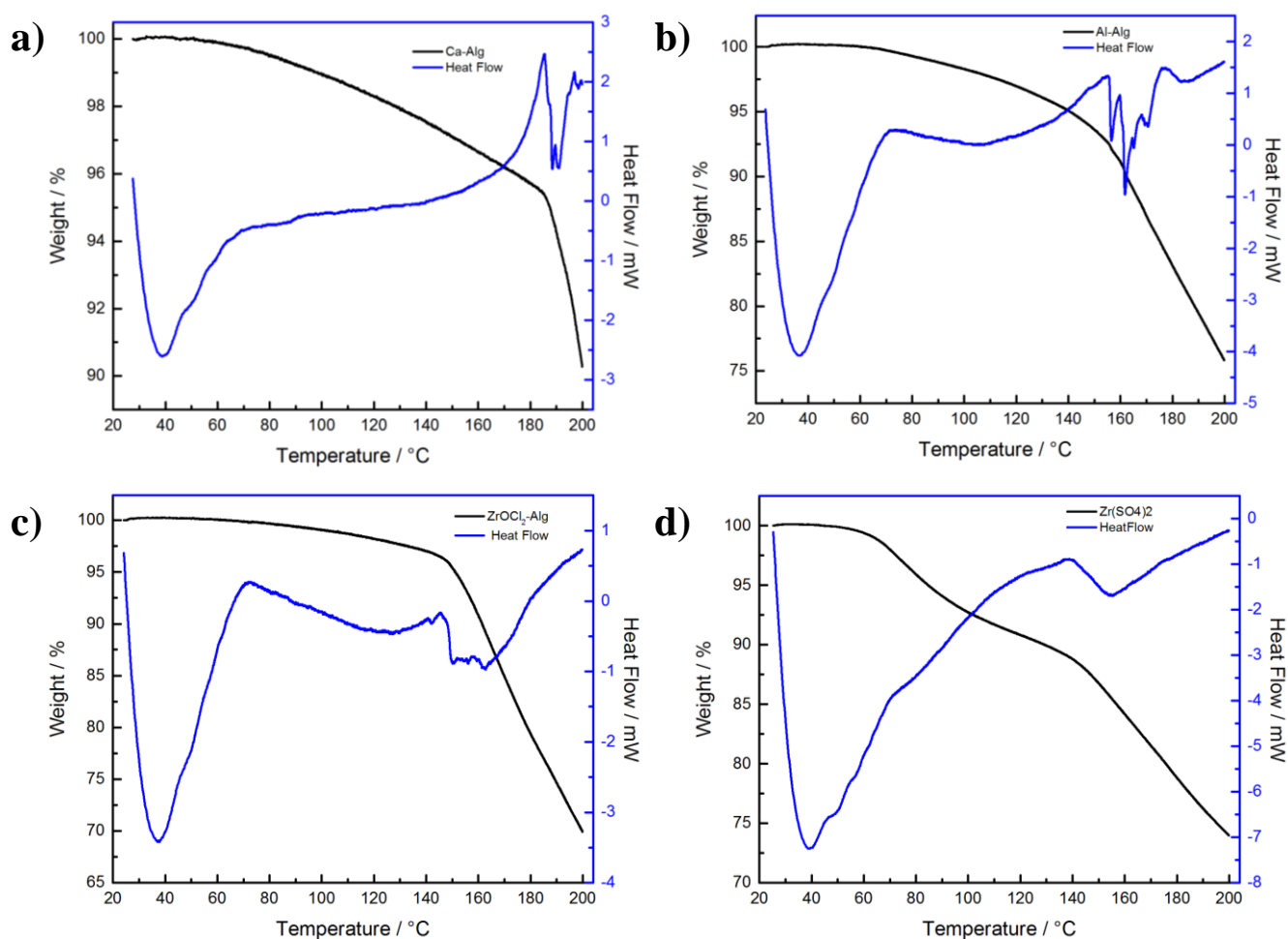


Figure 51: TGA-DSC of alginates crosslinked with different cations; (a) Ca^{2+} , (b) Al^{3+} , (c) Zr^{4+} ion from ZrOCl_2 , (d) Zr^{4+} ion from $\text{Zr}(\text{SO}_4)_2$. Heat rate was at 1°C per minute.

TGA-DSC data are shown in **Figure 51**. Hydrogels gelled using Al^{3+} and Zr^{4+} ions are much less thermally stable than calcium alginate. The % weight loss of alginates at different temperatures is shown in **Table 22**.

Table 22: The weight loss of alginates with various cations at different temperatures.

	% Weight loss at 135 °C	% Weight loss at 150 °C	% Weight loss at 200 °C
Ca^{2+}	2.27	2.91	9.72
Al^{3+}	4.39	6.37	24.17
$\text{Zr}^{4+} / \text{Zr}(\text{SO}_4)_2$	10.59	13.24	26.03
$\text{Zr}^{4+} / \text{ZrOCl}_2$	2.63	4.59	30.07

Cations with high valence (more than 2+) seem to catalyze the thermal degradation of polymers in alginate molecules. Two alginates; Zr-alginate and Ca-alginate before and after TGA-DSC measurement are compared (**Figure 52**). The color of Zr-alginate is black whereas Ca-alginate is less affected by heat (**Figure 51**) and the color is brown. Black color of Zr-alginate may indicate the thermal degradation (pyrolysis).

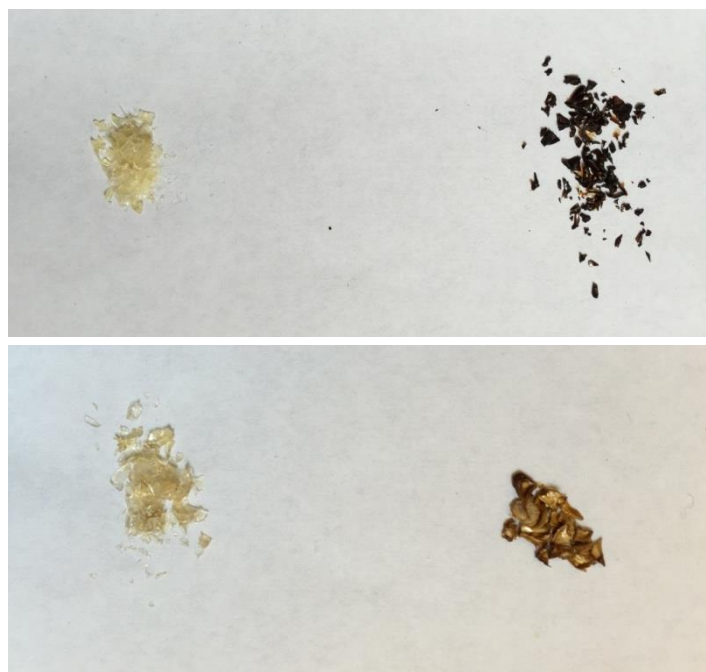


Figure 52: Dried alginate gels before heat treatment (left) and after heat treatment up to 200 °C (right). Alginate crosslinked by Zr^{4+} ions (top) is much less stable than Ca-alginate (bottom) at elevated temperatures and turns almost completely black when heated up to 200 °C.

Beads formulated using Zr^{4+} ions turned to strong yellow color after 2 hours of activation at 120 °C under vacuum. This color change occurred to a lesser extent for Ca-beads and Al-beads (**Figure 53**).

The gelation speed increases with valence of cations; MOF/alginate solution droplet was formed spherical using divalent cations (Ca, Ba, Cu) whereas Al-beads and Zr-beads became more flat at the same gelation distance (Bottom **Figure 53**). The gelation speed in Al- and Zr-gelation bath was so fast that the solution droplet becomes gel during the first deformation stage as illustrated in **Figure 10**.



Figure 53: Top, from left to right: Cu-beads, Al-beads and Zr-beads. After activation at 120 °C for 2 hours under vacuum. Bottom, from left to right: Ca-bead, Cu-bead, Al-bead and Zr-bead. Right after gelation.

Because the shape was not the same for gel beads to be tested in crushing strength, a different strategy was necessary. An intermediate step before the final gelation was added to make Al-beads and Zr-beads; they were gelled in Ca-gelation bath first, and then they were transferred to Al/Zr-gelation bath immediately. The gelation time for Ca^{2+} preformed beads was 90 minutes. In this way it was possible to make spherical Al/Zr-alginate beads.

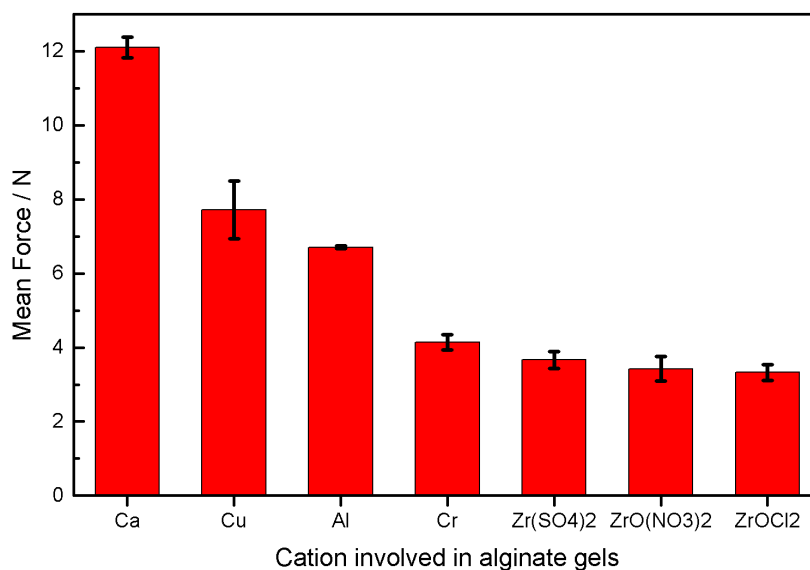


Figure 54: Alginates formed with different cations. Activated at 120 °C for 2 hours.

The average crushing strength decreases rapidly with cations with increasing valence. Interestingly, Cu-alg beads were significantly weaker than Ca-alg beads, and Cr-alg beads were weaker than Al-alg beads even though they have same valence (+2 and +3, respectively). This could mean that the strength of alginate gel depends on two parameters; 1) pH and 2) electron affinity of cation in the gelation bath.

Table 23 summarizes pH measured at room temperature in various gelation baths. The difference in pH between Al and Cr-bath is quite significant and this may have resulted in the difference in strength (**Figure 55**).

Table 23: pH at room temperature in different gelation bath.

pH (23 °C)	
Ca	6.1
Cu	5.6
Al	3.4
Cr	1.7
Zr(SO ₄) ₂	1.3
ZrO(NO ₃) ₂	1.4
ZrOCl ₂	1.3

In order to look at the effect of pH alone, a separate experiment was conducted. DWL-19 beads were gelled with calcium ions, but pH was varied using 0.1 M HCl and 0.1 M NaOH in the gelation bath. Crushing strength of DWL-14 with various pH is shown in **Figure 55**.

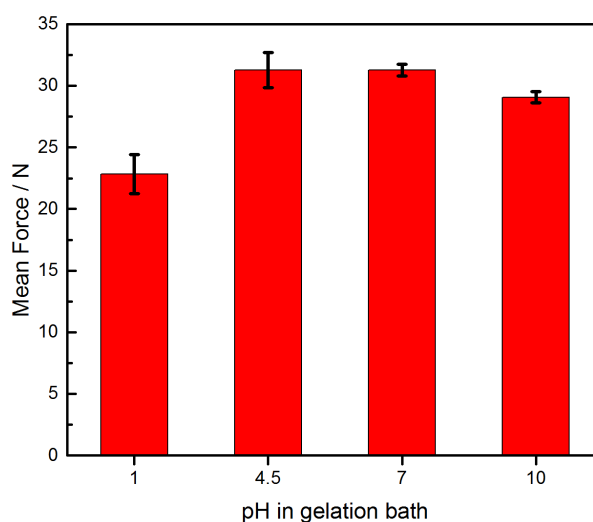


Figure 55: The average crushing force as a function of pH

Alginate gels formed at low pH ((b) **Figure 56**) turned opaque; Carboxylic groups in sodium alginate reacted with H^+ and became alginic acids. Resulting gel consists of Ca^{2+} -crosslinked blocks with alginic acids. This caused a decrease in gel strength. Gel beads in section c) are Zr-beads. They are flat, opaque and smaller in size than Ca-beads at low pH.

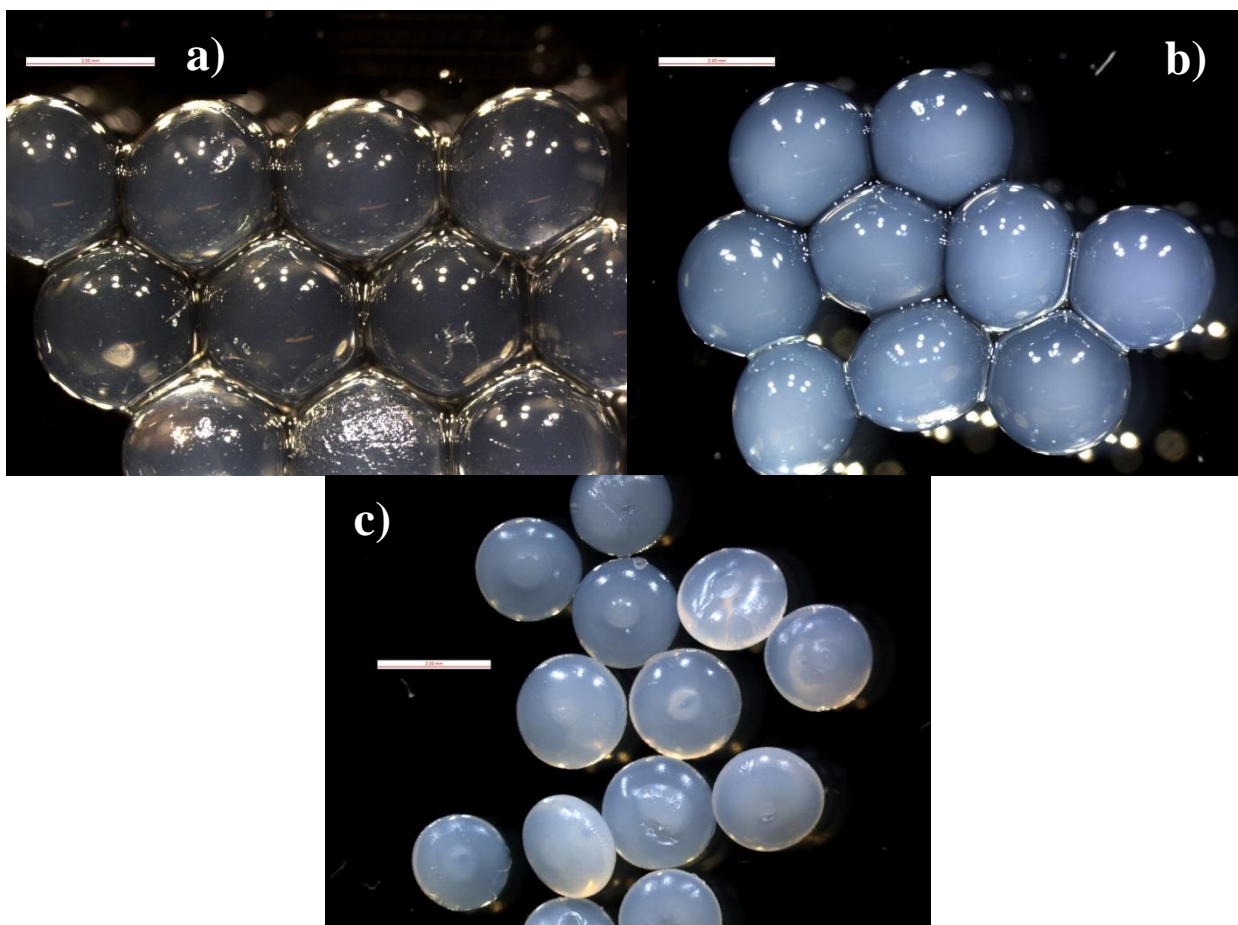


Figure 56: Alginate hydrogels formed at different pH values: a) in Ca-bath, pH = 5.3. b) Ca-bath, pH = 1.6. c) ZrOCl₂-bath, pH = 1.3. White bar corresponds to 2 mm.

Given that the difference in pH between Ca- and Cu-beads is small; their difference in crushing strength can possibly be due to higher electron affinity of Cu²⁺ ions. This might cause a catalyzed degradation effect on alginate polymers at elevated temperatures.

Al^{3+} ions and Zr^{4+} ions did not affect the nitrogen sorption isotherms. The relative ionic radius of Ca^{2+} , Al^{3+} and Zr^{4+} are 1.80 Å, 1.25 Å and 1.55 Å, respectively. These smaller ions cannot block the cavities in MOF.

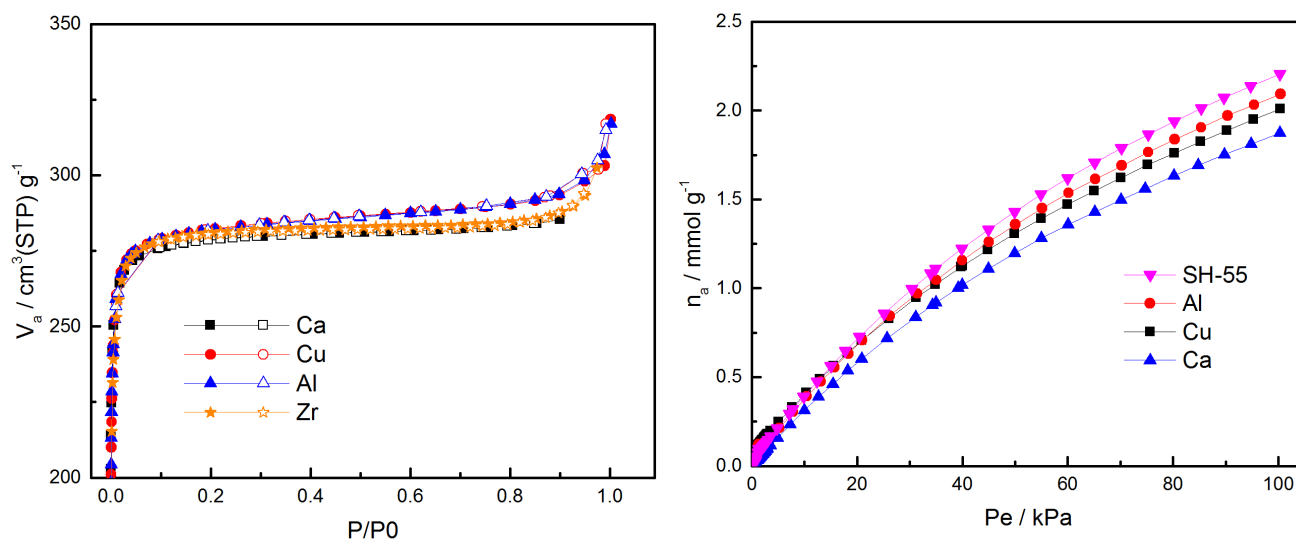


Figure 57: Nitrogen sorption isotherms for beads formulated with different cations (left). CO_2 uptake up to 100 kPa. MOF powder (SH-55) plotted as reference. The dry MOF contents in other beads are 90 wt%.

Interestingly, Cu- and Al-beads showed a slight increase in CO_2 uptake compared to Ca-beads. The dry MOF content in all the MOF-beads used in this work is 90 wt%. This could mean that greater electron affinity of Cu^{2+} and Al^{3+} ions could attract polar molecules such as CO_2 stronger, thus results in higher uptake per mass.

Surprisingly, UiO-66 MOF batch used in this work could tolerate low pH values well, except for one case where it has been exposed to $\text{Zr}(\text{SO}_4)_2$ bath. PXRD data shows that the structure of UiO-66 has almost totally collapsed. As seen from PXRD data, UiO-66 collapses when exposed to low pH and when SO_4^{2-} anions are present at the same time.

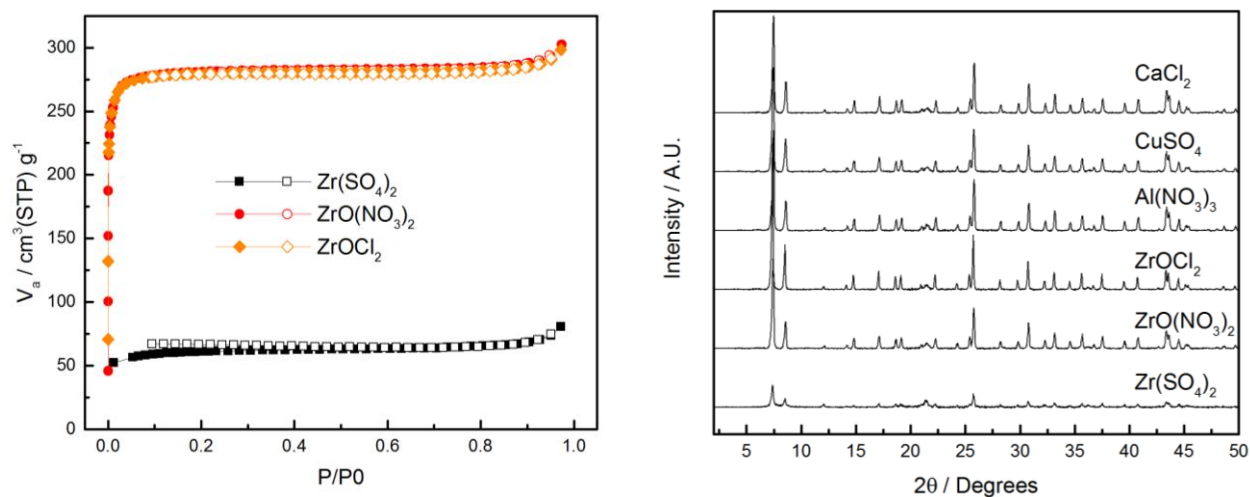


Figure 58: Nitrogen sorption isotherm of three different Zr-beads (left). PXRD data of MOF-bead formulated in gelation bath with different salts dissolved. pH decreases downwards (right).

Figure 59 shows MOF beads gelled with Ca^{2+} and Al^{3+} ions. The morphology of the beads are very similar.

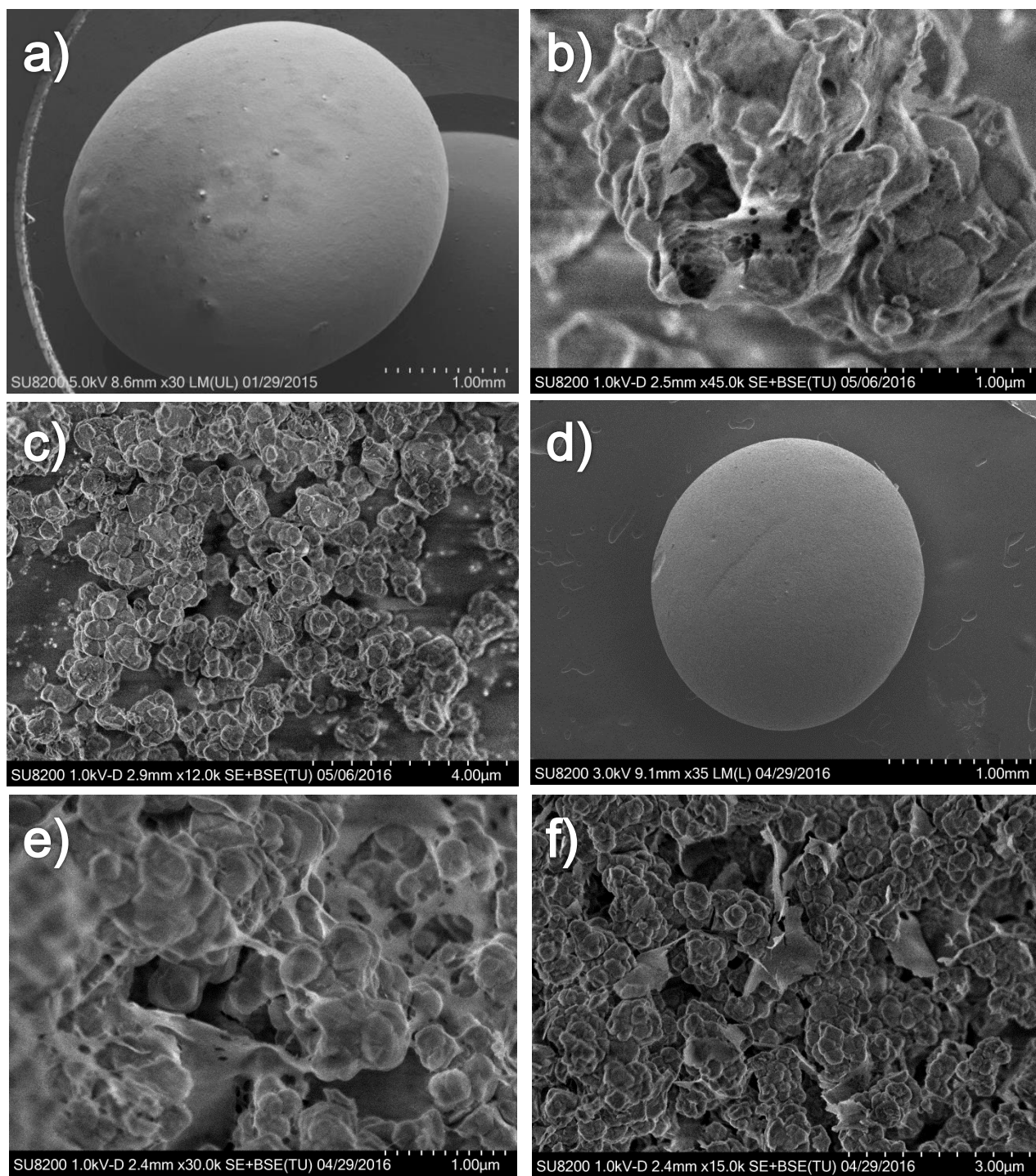


Figure 59: From a) to c): SEM images of a formulated MOF bead (DWL-2). SEM images taken with different magnifications at x30, x45.0k and x12.0k in a), b) and c), respectively. From d) to f); SEM images of DWL-13-Al taken with different magnifications at x35, x30.0k and x15.0k in d), e) and f), respectively.

Conclusion

Higher valent cations seem to be catalyzing the decomposition of alginate upon heating. As seen from Cu-bead example, high electron affinity and ionic radius of cations also affects the resulting crushing strength of alginate beads at elevated temperatures due to degradation.

Low pH decreases gel strength, but it alone did not collapse the UiO-66 MOF structure.

However, cations of higher valence or higher electron affinity seem to increase the total uptake of CO₂ at low pressure level up to 100 kPa.

3.8. Results From The Optimally Formulated Beads

Table 24 shows the optimal formulation formula employed in this work.

Table 24: Optimal formulation formula in this work.

Dry MOF content	90 wt%
Alginate / concentration	Manugel / 2 % (w/v)
Ca²⁺ concentration in gelation bath	2 % (w/v)
Gelation time	10 minutes
Washing time	10 minutes
Drying condition	40 °C overnight
Activation condition	135 °C / 3 hours

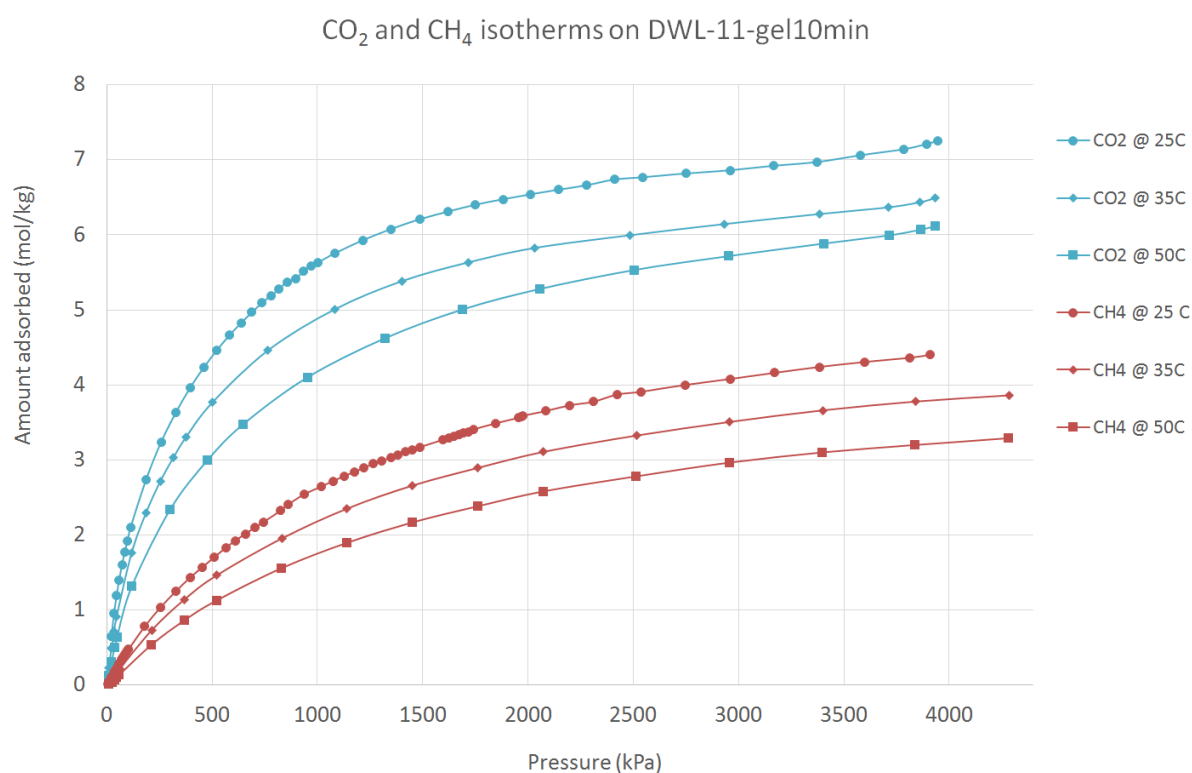


Figure 60: CH₄ and CO₂ uptake measured on formulated MOF-bead using optimal formulation formula.

Final MOF bead formulated using optimal formulation formula was tested for CH₄ and CO₂ uptake. MOF-bead adsorbed almost equal amount of CO₂ at the same temperature (25 °C) compared to reported value on unformulated UiO-66 powder (**Figure 61**). Methane uptake was lower at same temperature (25 °C, ca. 5.0 mol/kg for powder vs 4.4 mol/kg for the bead) at 4000 kPa. This is reasonable since the dry MOF content for bead was 90 wt%. CO₂ molecules are polar, thus may have been attracted to other functional groups (hydroxyl and carboxylic groups) in alginate; resulting in higher uptake per mass.

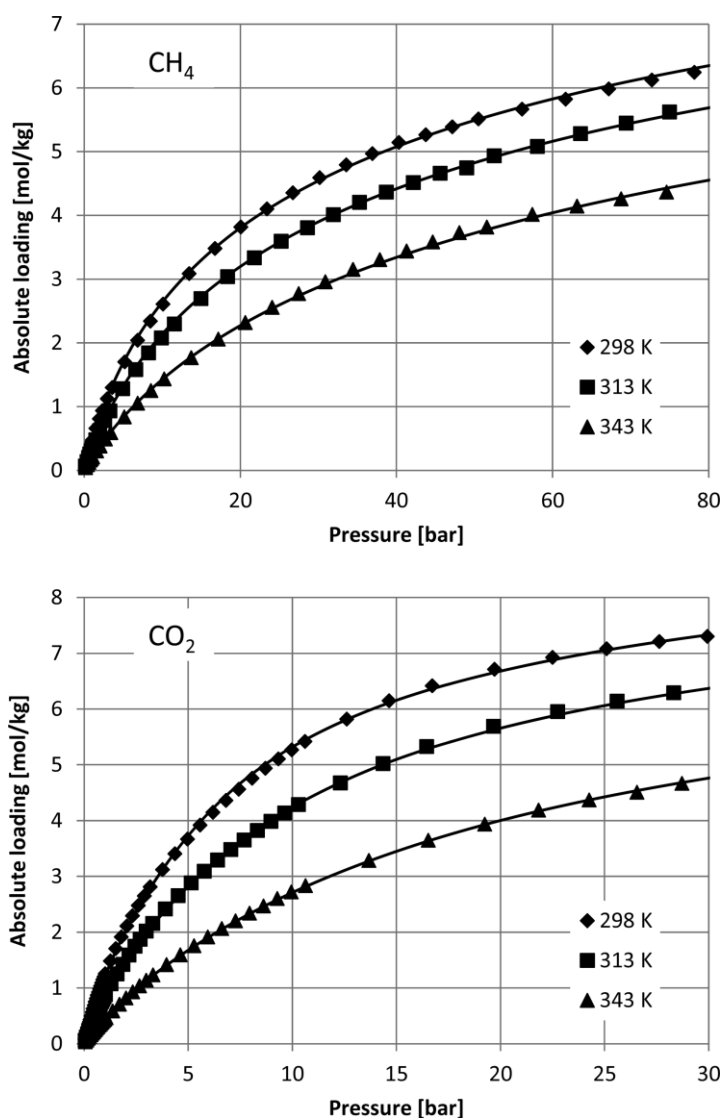


Figure 61: CH₄ and CO₂ uptake on UiO-66 reported in the literature.²

MOF beads formulated with alginate seem to be promising for industrial applications at relatively low temperature.

4. Conclusion

Stronger mechanical strength with increasing alginate concentration was observed. However, as the amount of alginate is increased, the viscosity of the MOF/alginate slurry becomes too high; making it difficult to obtain a homogeneous sample (See **Appendix 7.8**).

Alginates with high G-block content is superior to alginates with low G-block content in terms of gel strength. Molecular weight of alginate is also playing an important role in thermal stability. However, the final comment on this should be postponed until further investigation is done. In this work, alginate Manugel seems to be the best.

Ca-beads seemed to be the strongest compared to beads gelled with other cations (Cu^{2+} , Al^{3+} and Zr^{4+}) due to lower electron and alginate affinity, thus less affected by thermal degradation. 2 %(w/v) calcium chloride concentration in gelation bath was found to be the best for the shape and throughput of MOF-beads. Gelation time above 15 minutes did not increase the gel strength. Washing time of 10 minutes was found to be sufficient.

All of the alginate used in this work start being degraded at relatively low temperature (~70 °C). Air drying prior to the activation should not be above 60 °C. When activation temperature exceeds 150 °C, the gel strength decreases rapidly. It was found that activation temperature of 120 °C - 135 °C was sufficient for the formulation purposes as the thermal damage on alginate was less than 150 °C.



Table 25: Factors found to affect the shape and strength of MOF-beads.

Shape	Strength
<ul style="list-style-type: none">• Cations with various valence• Ca^{2+} concentration in gelation bath• Alginate concentration• Viscosity of MOF/alginate slurry	<ul style="list-style-type: none">• Increasing alginate concentration• Increasing Ca content in gelation bath• Cations with low electron/alginate affinity• Higher G-block content in the alginate.

5. Suggestions for Further Work

Further investigation into other types of alginate with higher G-block content or other types of binders that are more heat-resistant is needed. Also, increasing the gas uptake by modifying alginate structure using other types of cations source would be interesting.

Apply this formulation formula to other types of (water resistant) MOF should be the next step.

Investigate the optimal gelation conditions (viscosity of MOF/alginate slurry, gelation distance, making a multi nozzle head, the pumping rate) to optimize the throughput is also interesting for industrial applications.

6. References

Uncategorized References

1. KIMICA Alginate Chemical Structure. http://www.kimica-alginate.com/alginate/chemical_structure.html (accessed September 16).
2. Cavka, J. H.; Grande, C. A.; Mondino, G.; Blom, R., High Pressure Adsorption of CO₂ and CH₄ on Zr-MOFs. *Industrial & Engineering Chemistry Research* **2014**, *53* (40), 15500-15507.
3. Zhang, J.; Ji, Q.; Shen, X.; Xia, Y.; Tan, L.; Kong, Q., Pyrolysis products and thermal degradation mechanism of intrinsically flame-retardant calcium alginate fibre. *Polymer Degradation and Stability* **2011**, *96* (5), 936-942.
4. Spjelkavik, A. I.; Aarti; Divekar, S.; Didriksen, T.; Blom, R., Forming MOFs into Spheres by Use of Molecular Gastronomy Methods. *Chemistry-a European Journal* **2014**, *20* (29), 8973-8978.
5. Zhou, H.-C.; Long, J. R.; Yaghi, O. M., Introduction to Metal–Organic Frameworks. *Chemical Reviews* **2012**, *112* (2), 673-674.
6. Cavka, J. H.; Jakobsen, S.; Olsbye, U.; Guillou, N.; Lamberti, C.; Bordiga, S.; Lillerud, K. P., A New Zirconium Inorganic Building Brick Forming Metal Organic Frameworks with Exceptional Stability. *Journal of the American Chemical Society* **2008**, *130* (42), 13850-13851.
7. Wu, H.; Yildirim, T.; Zhou, W., Exceptional Mechanical Stability of Highly Porous Zirconium Metal-Organic Framework UiO-66 and Its Important Implications. *J Phys Chem Lett* **2013**, *4* (6), 925-30.
8. A. Grande, C.; I. Águeda, V.; Spjelkavik, A.; Blom, R., An efficient recipe for formulation of metal-organic Frameworks. *Chemical Engineering Science* **2015**, *124*, 154-158.
9. Batten, S. R.; Champness, N. R.; Chen, X.-M.; Garcia-Martinez, J.; Kitagawa, S.; Öhrström, L.; O’Keeffe, M.; Paik Suh, M.; Reedijk, J., Terminology of metal–organic frameworks and coordination polymers (IUPAC Recommendations 2013). *Pure and Applied Chemistry* **2013**, *85* (8).
10. Kinoshita, Y.; Matsubara, I.; Higuchi, T.; Saito, Y., The Crystal Structure of Bis(adiponitrilo)copper(I) Nitrate. *Bulletin of the Chemical Society of Japan* **1959**, *32* (11), 1221-1226.
11. Yaghi, O. M.; Li, H., Hydrothermal Synthesis of a Metal-Organic Framework Containing Large Rectangular Channels. *Journal of the American Chemical Society* **1995**, *117* (41), 10401-10402.
12. Eddaoudi, M.; Moler, D. B.; Li, H.; Chen, B.; Reineke, T. M.; O’Keeffe, M.; Yaghi, O. M., Modular Chemistry: Secondary Building Units as a Basis for the Design of Highly Porous and Robust Metal–Organic Carboxylate Frameworks. *Accounts of Chemical Research* **2001**, *34* (4), 319-330.
13. MacGillivray, L. R.; Subramanian, S.; Zaworotko, M. J., Interwoven two- and three-dimensional coordination polymers through self-assembly of Cu cations with linear bidentate ligands. *Journal of the Chemical Society, Chemical Communications* **1994**, (11), 1325-1326.
14. Farrusseng, D., *Metal-Organic Frameworks: Applications from Catalysis to Gas Storage*. Wiley: 2011.
15. Kondo, M.; Yoshitomi, T.; Matsuzaka, H.; Kitagawa, S.; Seki, K., Three-Dimensional Framework with Channeling Cavities for Small Molecules: {[M₂(4, 4’-

- bpy)₃(NO₃)₄]·xH₂O}_n (M □ Co, Ni, Zn). *Angewandte Chemie International Edition in English* **1997**, *36* (16), 1725-1727.
16. Li, H.; Eddaoudi, M.; Groy, T. L.; Yaghi, O. M., Establishing Microporosity in Open Metal–Organic Frameworks: Gas Sorption Isotherms for Zn(BDC) (BDC = 1,4-Benzenedicarboxylate). *Journal of the American Chemical Society* **1998**, *120* (33), 8571-8572.
 17. Li, H.; Eddaoudi, M.; O'Keeffe, M.; Yaghi, O. M., Design and synthesis of an exceptionally stable and highly porous metal-organic framework. *Nature* **1999**, *402* (6759), 276-279.
 18. Millward, A. R.; Yaghi, O. M., Metal–Organic Frameworks with Exceptionally High Capacity for Storage of Carbon Dioxide at Room Temperature. *Journal of the American Chemical Society* **2005**, *127* (51), 17998-17999.
 19. Chae, H. K.; Siberio-Perez, D. Y.; Kim, J.; Go, Y.; Eddaoudi, M.; Matzger, A. J.; O'Keeffe, M.; Yaghi, O. M., A route to high surface area, porosity and inclusion of large molecules in crystals. *Nature* **2004**, *427* (6974), 523-527.
 20. Zaworotko, M. J., Materials science: Open season for solid frameworks. *Nature* **1999**, *402* (6759), 242-243.
 21. Kitagawa, S.; Kitaura, R.; Noro, S.-i., Functional Porous Coordination Polymers. *Angewandte Chemie International Edition* **2004**, *43* (18), 2334-2375.
 22. Tranchemontagne, D. J.; Mendoza-Cortes, J. L.; O'Keeffe, M.; Yaghi, O. M., Secondary building units, nets and bonding in the chemistry of metal-organic frameworks. *Chemical Society Reviews* **2009**, *38* (5), 1257-1283.
 23. Ferey, G., Hybrid porous solids: past, present, future. *Chemical Society Reviews* **2008**, *37* (1), 191-214.
 24. Garibay, S. J.; Wang, Z.; Tanabe, K. K.; Cohen, S. M., Postsynthetic Modification: A Versatile Approach Toward Multifunctional Metal–Organic Frameworks. *Inorganic Chemistry* **2009**, *48* (15), 7341-7349.
 25. Tanabe, K. K.; Cohen, S. M., Postsynthetic modification of metal-organic frameworks—a progress report. *Chemical Society Reviews* **2011**, *40* (2), 498-519.
 26. Zhang, W.; Hu, Y.; Ge, J.; Jiang, H.-L.; Yu, S.-H., A Facile and General Coating Approach to Moisture/Water-Resistant Metal–Organic Frameworks with Intact Porosity. *Journal of the American Chemical Society* **2014**, *136* (49), 16978-16981.
 27. Park, K. S.; Ni, Z.; Côté, A. P.; Choi, J. Y.; Huang, R.; Uribe-Romo, F. J.; Chae, H. K.; O'Keeffe, M.; Yaghi, O. M., Exceptional chemical and thermal stability of zeolitic imidazolate frameworks. *Proceedings of the National Academy of Sciences of the United States of America* **2006**, *103* (27), 10186-10191.
 28. Devic, T.; Serre, C., High valence 3p and transition metal based MOFs. *Chemical Society Reviews* **2014**, *43* (16), 6097-6115.
 29. Li, J.-R.; Kuppler, R. J.; Zhou, H.-C., Selective gas adsorption and separation in metal-organic frameworks. *Chemical Society Reviews* **2009**, *38* (5), 1477-1504.
 30. Lee, J.; Farha, O. K.; Roberts, J.; Scheidt, K. A.; Nguyen, S. T.; Hupp, J. T., Metal-organic framework materials as catalysts. *Chemical Society Reviews* **2009**, *38* (5), 1450-1459.
 31. Chapman, K. W.; Halder, G. J.; Chupas, P. J., Pressure-Induced Amorphization and Porosity Modification in a Metal–Organic Framework. *Journal of the American Chemical Society* **2009**, *131* (48), 17546-17547.
 32. Hu, Y. H.; Zhang, L., Amorphization of metal-organic framework MOF-5 at unusually low applied pressure. *Physical Review B* **2010**, *81* (17), 174103.

33. Casco, M. E.; Martínez-Escandell, M.; Gadea-Ramos, E.; Kaneko, K.; Silvestre-Albero, J.; Rodríguez-Reinoso, F., High-Pressure Methane Storage in Porous Materials: Are Carbon Materials in the Pole Position? *Chemistry of Materials* **2015**, *27* (3), 959-964.
34. Bosch, M.; Zhang, M.; Zhou, H.-C., Increasing the Stability of Metal-Organic Frameworks. *Advances in Chemistry* **2014**, *2014*, 8.
35. Bai, Y.; Dou, Y.; Xie, L. H.; Rutledge, W.; Li, J. R.; Zhou, H. C., Zr-based metal-organic frameworks: design, synthesis, structure, and applications. *Chem Soc Rev* **2016**.
36. Howarth, A. J.; Liu, Y.; Li, P.; Li, Z.; Wang, T. C.; Hupp, J. T.; Farha, O. K., Chemical, thermal and mechanical stabilities of metal-organic frameworks. *Nature Reviews Materials* **2016**, *1*, 15018.
37. Valenzano, L.; Civalleri, B.; Chavan, S.; Bordiga, S.; Nilsen, M. H.; Jakobsen, S.; Lillerud, K. P.; Lamberti, C., Disclosing the Complex Structure of UiO-66 Metal Organic Framework: A Synergic Combination of Experiment and Theory. *Chemistry of Materials* **2011**, *23* (7), 1700-1718.
38. Wiersum, A. D.; Soubeyrand-Lenoir, E.; Yang, Q.; Moulin, B.; Guillerm, V.; Yahia, M. B.; Bourrelly, S.; Vimont, A.; Miller, S.; Vagner, C.; Daturi, M.; Clet, G.; Serre, C.; Maurin, G.; Llewellyn, P. L., An Evaluation of UiO-66 for Gas-Based Applications. *Chemistry – An Asian Journal* **2011**, *6* (12), 3270-3280.
39. Chen, B.; Ma, S.; Zapata, F.; Fronczek, F. R.; Lobkovsky, E. B.; Zhou, H.-C., Rationally Designed Micropores within a Metal-Organic Framework for Selective Sorption of Gas Molecules. *Inorganic Chemistry* **2007**, *46* (4), 1233-1236.
40. Bae, Y.-S.; Snurr, R. Q., Development and Evaluation of Porous Materials for Carbon Dioxide Separation and Capture. *Angewandte Chemie International Edition* **2011**, *50* (49), 11586-11596.
41. Sumida, K.; Rogow, D. L.; Mason, J. A.; McDonald, T. M.; Bloch, E. D.; Herm, Z. R.; Bae, T.-H.; Long, J. R., Carbon Dioxide Capture in Metal-Organic Frameworks. *Chemical Reviews* **2012**, *112* (2), 724-781.
42. Li, B.; Leng, K.; Zhang, Y.; Dynes, J. J.; Wang, J.; Hu, Y.; Ma, D.; Shi, Z.; Zhu, L.; Zhang, D.; Sun, Y.; Chrzanowski, M.; Ma, S., Metal-Organic Framework Based upon the Synergy of a Brønsted Acid Framework and Lewis Acid Centers as a Highly Efficient Heterogeneous Catalyst for Fixed-Bed Reactions. *Journal of the American Chemical Society* **2015**, *137* (12), 4243-4248.
43. Küsgens, P.; Zgaverdea, A.; Fritz, H.-G.; Siegle, S.; Kaskel, S., Metal-Organic Frameworks in Monolithic Structures. *Journal of the American Ceramic Society* **2010**, *93* (9), 2476-2479.
44. Klimakow, M.; Klobes, P.; Rademann, K.; Emmerling, F., Characterization of mechanochemically synthesized MOFs. *Microporous and Mesoporous Materials* **2012**, *154*, 113-118.
45. Lee, P.; Rogers, M. A., Effect of calcium source and exposure-time on basic caviar spherification using sodium alginate. *International Journal of Gastronomy and Food Science* **2012**, *1* (2), 96-100.
46. Kuo, C. K.; Ma, P. X., Ionically crosslinked alginate hydrogels as scaffolds for tissue engineering: Part 1. Structure, gelation rate and mechanical properties. *Biomaterials* **2001**, *22* (6), 511-521.
47. LeRoux, M. A.; Guilak, F.; Setton, L. A., Compressive and shear properties of alginate gel: effects of sodium ions and alginate concentration. *Journal of biomedical materials research* **1999**, *47* (1), 46-53.
48. Drury, J. L.; Dennis, R. G.; Mooney, D. J., The tensile properties of alginate hydrogels. *Biomaterials* **2004**, *25* (16), 3187-3199.

49. Jodra, Y.; Mijangos, F., Ion exchange selectivities of calcium alginate gels for heavy metals. *Water science and technology : a journal of the International Association on Water Pollution Research* **2001**, *43* (2), 237-44.
50. Haug, A., Fractionation of Alginic Acid. *Acta Chemica Scandinavica* **1959**, *13*, 601-603.
51. George, M.; Abraham, T. E., Polyionic hydrocolloids for the intestinal delivery of protein drugs: Alginate and chitosan — a review. *Journal of Controlled Release* **2006**, *114* (1), 1-14.
52. Senkovska, I.; Kaskel, S., Ultrahigh porosity in mesoporous MOFs: promises and limitations. *Chemical Communications* **2014**, *50* (54), 7089-7098.
53. Wikipedia Infrared spectroscopy. https://en.wikipedia.org/wiki/Infrared_spectroscopy (accessed 15 April).
54. Wikipedia Infrared spectroscopy correlation table. https://en.wikipedia.org/wiki/Infrared_spectroscopy_correlation_table (accessed 15 April).
55. Kamal, I. M.; Adam, G. A.; Getta, H. K. A., The effect of molecular weight on the thermal stability of polyvinyl chloride. *Thermochimica Acta* **1983**, *62* (2), 355-359.
56. Adam, G. A.; Hay, J. N.; Parsons, I. W.; Haward, R. N., Effect of molecular weight on the thermal properties of polycarbonates. *Polymer* **1976**, *17* (1), 51-57.
57. Vreeker, R.; Li, L.; Fang, Y.; Appelqvist, I.; Mendes, E., Drying and Rehydration of Calcium Alginate Gels. *Food Biophysics* **2008**, *3* (4), 361-369.

7. Appendices

7.1. Detailed Synthesis of UiO-66 (SH-55)

SH-55 batch sample was synthesized by sequentially adding 3.78 g ZrCl_4 (16.2 mmol), 2.86 ml 35 % HCl (32.4 mmol), and 5.39 g H_2BDC (32.4 mmol) to a 250 ml conical flask containing 97.4 ml of N,N'-dimethyl formamide (1260 mmol). BDC:Zr molar ratio in the synthesis solution was 2:1. The synthesis mixture was stirred until the solution was completely transparent before being transferred to 200 mL Teflon liners and sealed in stainless steel autoclaves where it was heated to 200 °C for 20 hours. The resulting microcrystalline powder was separated from the solvent by centrifugation and dried overnight in an oven set to 60 °C.

7.2. Calculation of the decrease in N₂ isotherms

The decrease in nitrogen isotherms is calculated as follows:

For DWL-5:

$$\frac{302.77 - 288.13 \text{ cm}^3(\text{STP})\text{g}^{-1}}{302.77 \text{ cm}^3(\text{STP})\text{g}^{-1}} \times 100 \approx 4.8 \%$$

The decrease for DWL-2 and DWL-9-1.8%-Ca2% is found to be 6.9 % and 16.1 %, respectively.

7.3. Calculation of Ca:Zr ratio

Calculation of Ca:Zr ratio is as follow:

$$n_{Zr} = \frac{m_{\text{UiO-66}}}{M_{\text{UiO-66}}} \times 24 = \frac{0.9 \text{ g}}{6704.56 \frac{\text{g}}{\text{mol}}} \times 24 = 3.22 \text{ mmol}$$

$$n_{\text{Na}} = \frac{m_{\text{NaAlg}}}{M_{\text{NaAlg}}} = \frac{0.1 \text{ g}}{216.12 \frac{\text{g}}{\text{mol}}} = 0.46 \text{ mmol}$$

$$n_{\text{Ca}} = \frac{1}{2} n_{\text{Na}} = 0.23 \text{ mmol}$$

$$\frac{n_{\text{Ca}}}{n_{\text{Zr}}} = \frac{0.23 \text{ mmol}}{3.22 \text{ mmol}} \approx \mathbf{0.0718}$$

Where:

n_{Zr} is the mol of Zr atoms

$m_{\text{UiO-66}}$ is the mass of UiO-66

$M_{\text{UiO-66}}$ is the molar mass of UiO-66

n_{Na} is the mol of Na atoms

n_{Ca} is the mol of Ca atoms

7.4. The amount of calcium ions needed in the gelation

For DWL-9, the amount of calcium ions needed in the gelation is calculated as follow:

$$\frac{m_{NaAlg}}{M_{NaAlg}} = \frac{0.36 \text{ g}}{216.12 \frac{\text{g}}{\text{mol}}} = 1.67 \cdot 10^{-3} \text{ mol}$$

Chemical formula of sodium alginate is $C_6H_9NaO_7$. If we assume that the complete ion exchange takes place (2 Na^+ ions exchange by 1 Ca^{2+} ion):

$$n_{Ca} = \frac{1}{2} n_{Na} = \frac{1}{2} * 1.67 \cdot 10^{-3} \text{ mol} = 8.33 \cdot 10^{-4} \text{ mol}$$

Since the alginate was dissolved in 20 mL MOF/water mixture, the resulting calcium concentration in 0.02 L MOF/alginate mixture is:

$$[Ca^{2+}] \text{ in 20 mL MOF/alginate mixture} = \frac{8.33 \cdot 10^{-4} \text{ mol}}{0.020 \text{ L}} = 4.16 \cdot 10^{-2} \frac{\text{mol}}{\text{L}}$$

The average diameter of hydrated beads (measured immediately after gelling) was ca. 4 mm; totaling around 597 beads out of 20 mL MOF/alginate mixture:

$$V_{bead} = \frac{4}{3} \pi r_{bead}^3 = \frac{4}{3} \pi \left(\frac{0.4 \text{ cm}}{2} \right)^3 \approx 3.35 \cdot 10^{-2} \text{ cm}^3$$

$$\frac{20 \text{ cm}^3}{3.35 \cdot 10^{-2} \text{ cm}^3} \approx 597$$

This means that the concentration of calcium ions per Ca^{2+} ion-saturated MOF bead is $6.97 \cdot 10^{-5} \frac{\text{mol}}{\text{L}}$:

$$\frac{4.16 \cdot 10^{-2} \frac{\text{mol}}{\text{L}}}{597 \text{ beads}} \approx 6.97 \cdot 10^{-5} \frac{\text{mol}}{\text{L}} \text{ per bead}$$

When 2 % (w/v) of calcium chloride is dissolved in the gelation bath, the concentration of calcium ions is:

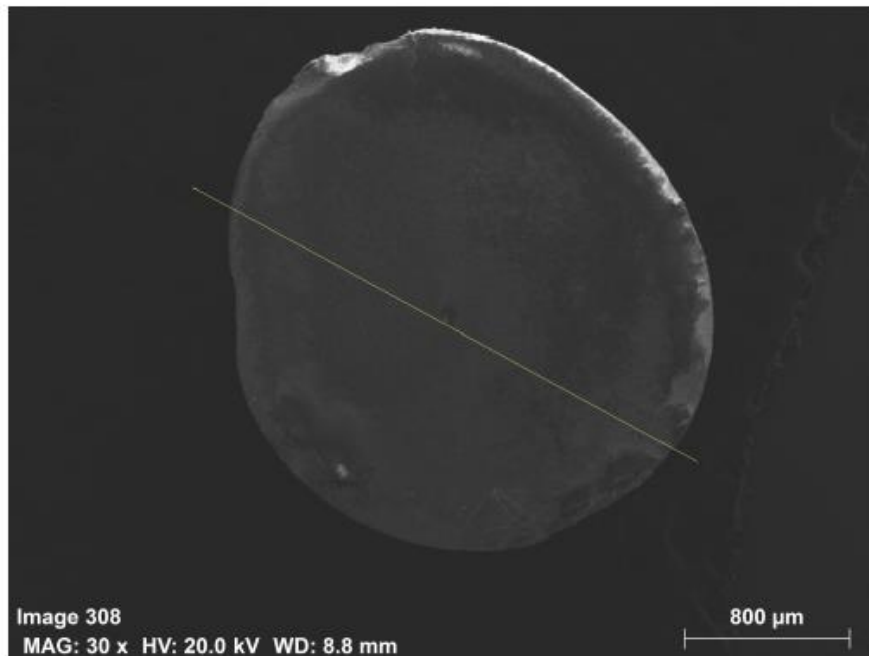
2.0 g of $\text{CaCl}_2 \cdot 6 \text{H}_2\text{O}$ was dissolved in 100 mL water:

$$n_{\text{Ca}^{2+}} = \frac{m_{\text{CaCl}_2 \cdot 6 \text{H}_2\text{O}}}{M_{\text{CaCl}_2 \cdot 6 \text{H}_2\text{O}}} = \frac{2.0 \text{ g}}{219.08 \frac{\text{g}}{\text{mol}}} \approx 9.13 \times 10^{-3} \text{ mol}$$

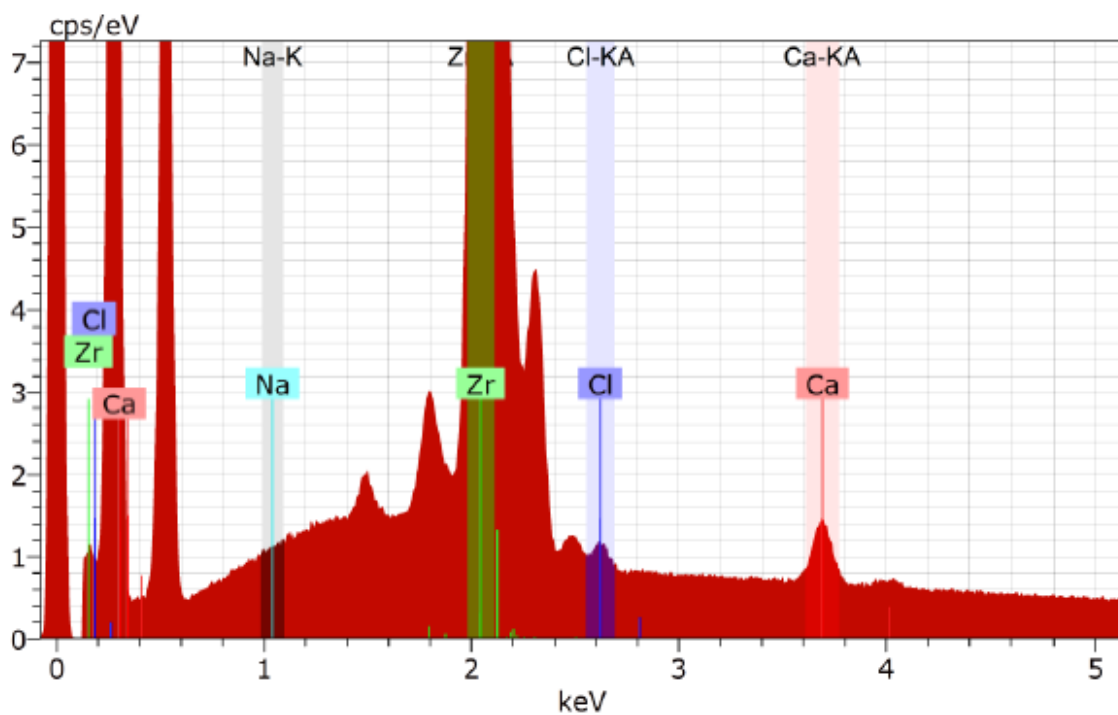
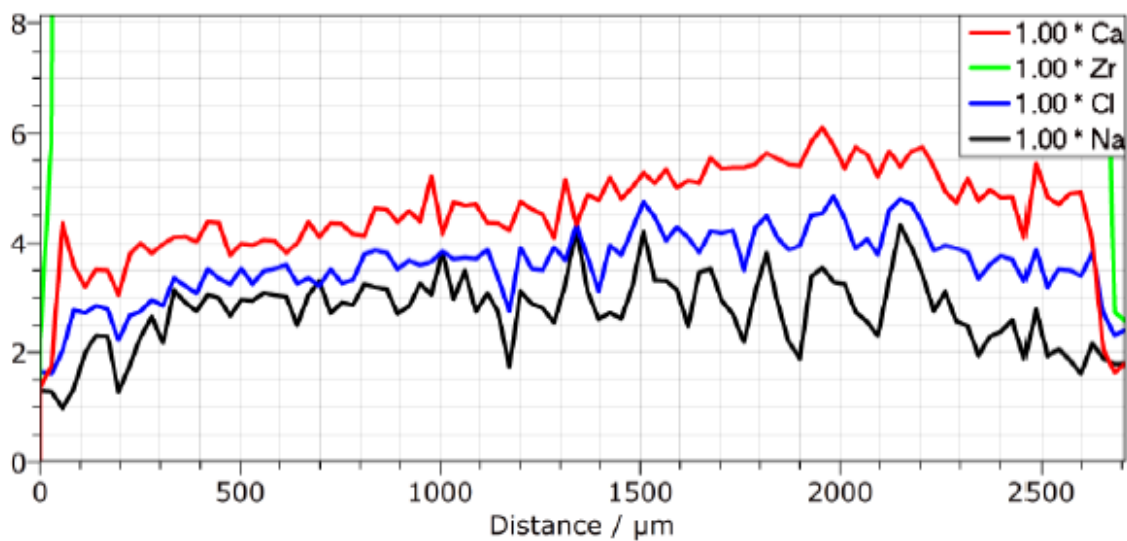
$$\frac{n_{\text{Ca}^{2+}}}{\text{Water}} = \frac{9.13 \times 10^{-3} \text{ mol}}{0.1 \text{ L}} = 9.13 \times 10^{-2} \frac{\text{mol}}{\text{L}}$$

7.5. EDX

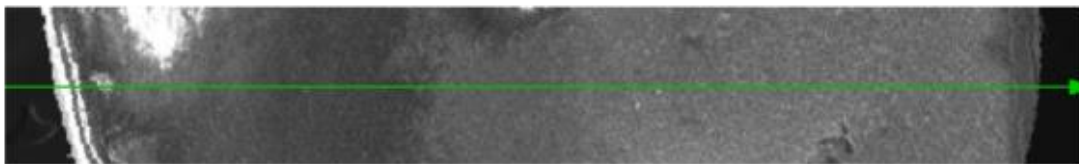
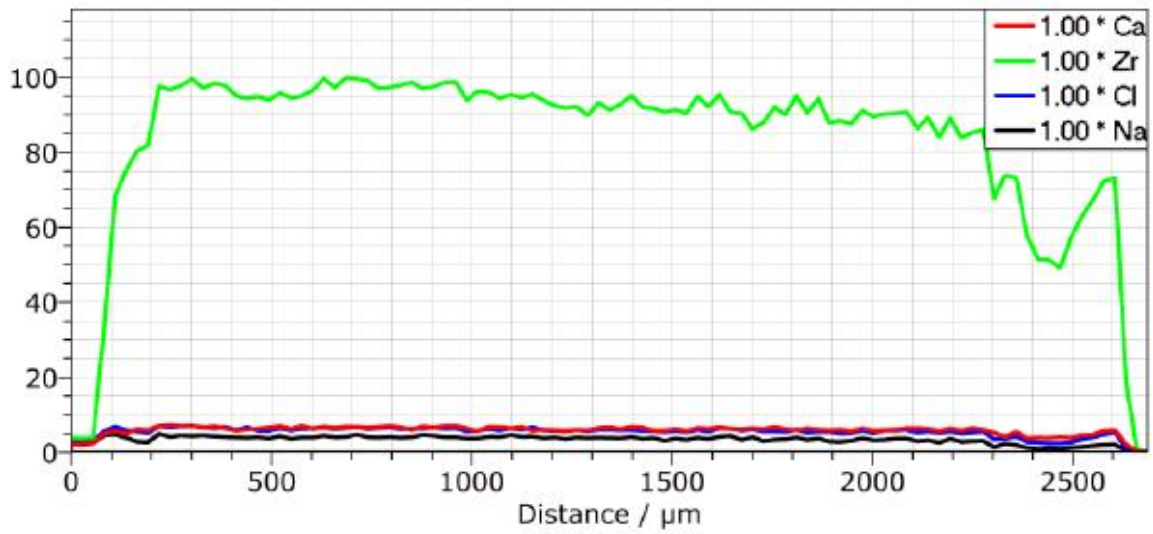
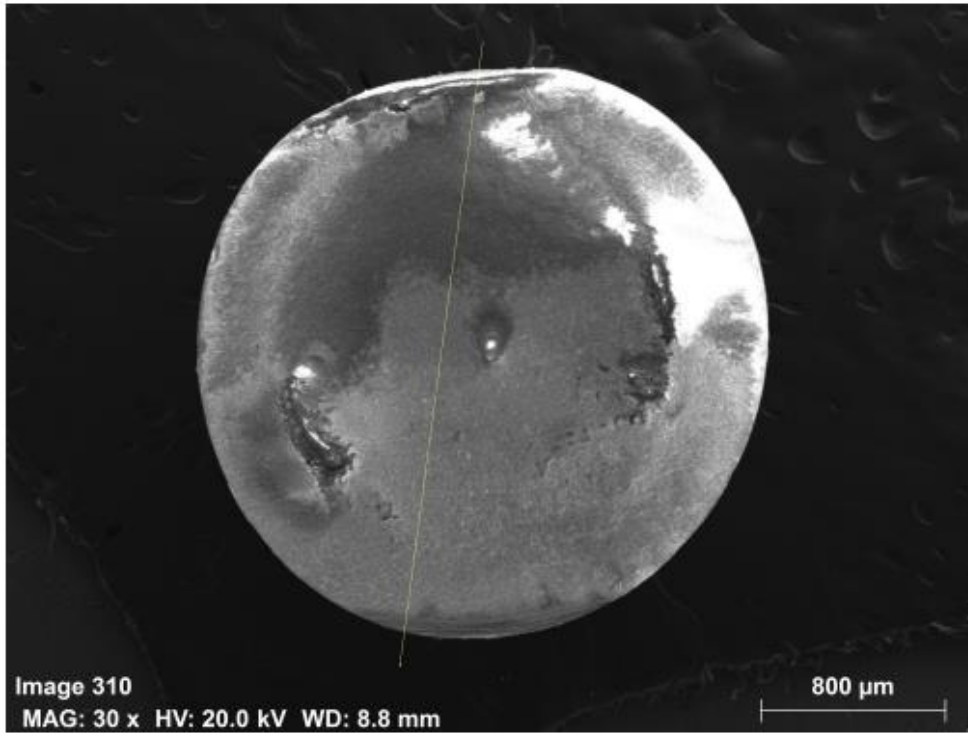
7.5.1. EDX on samples with various washing times



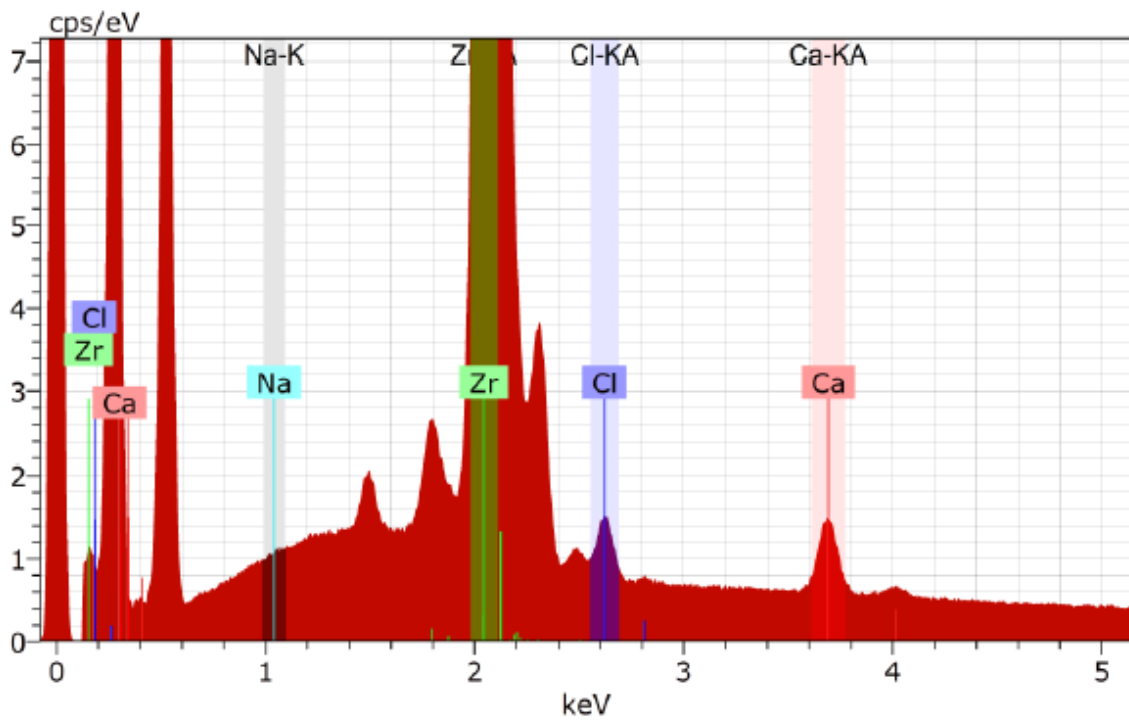
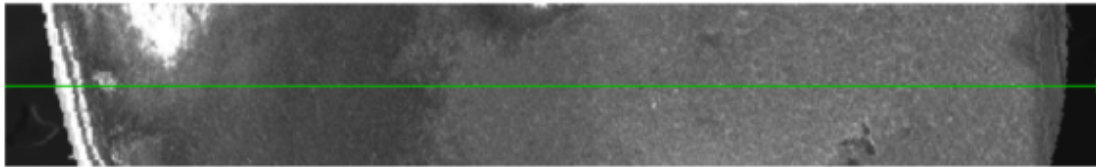
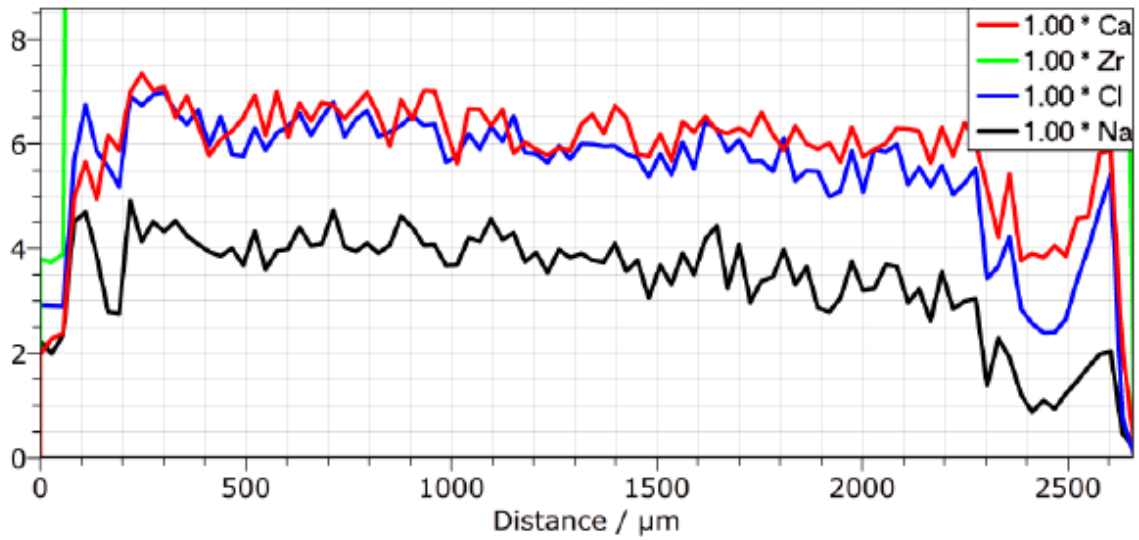
A bead washed for 90 minutes.



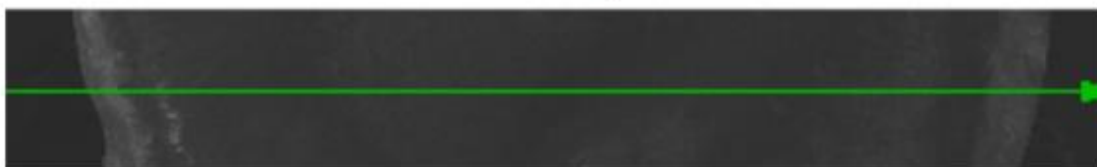
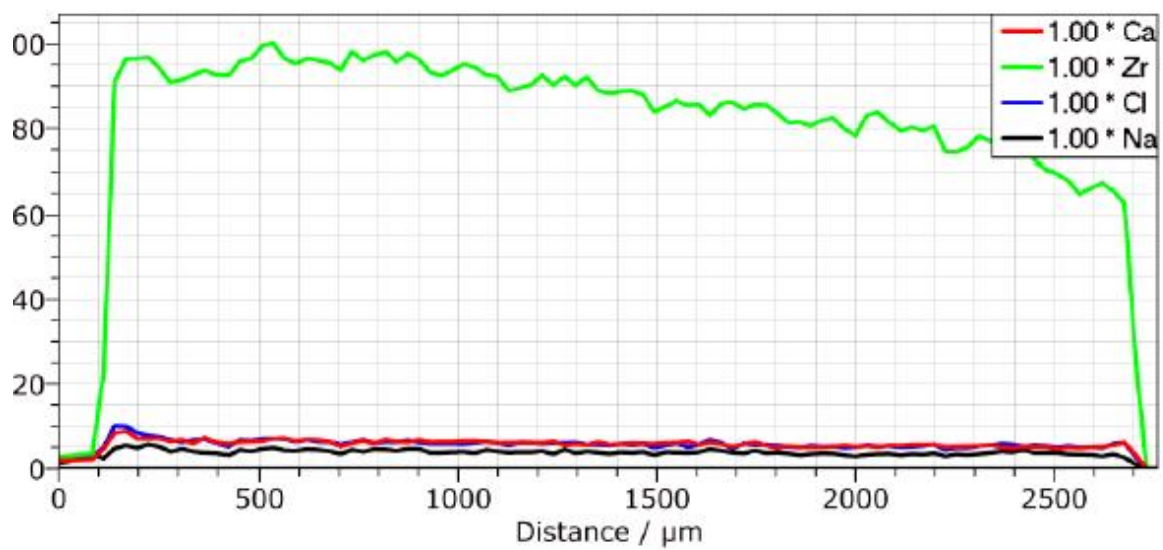
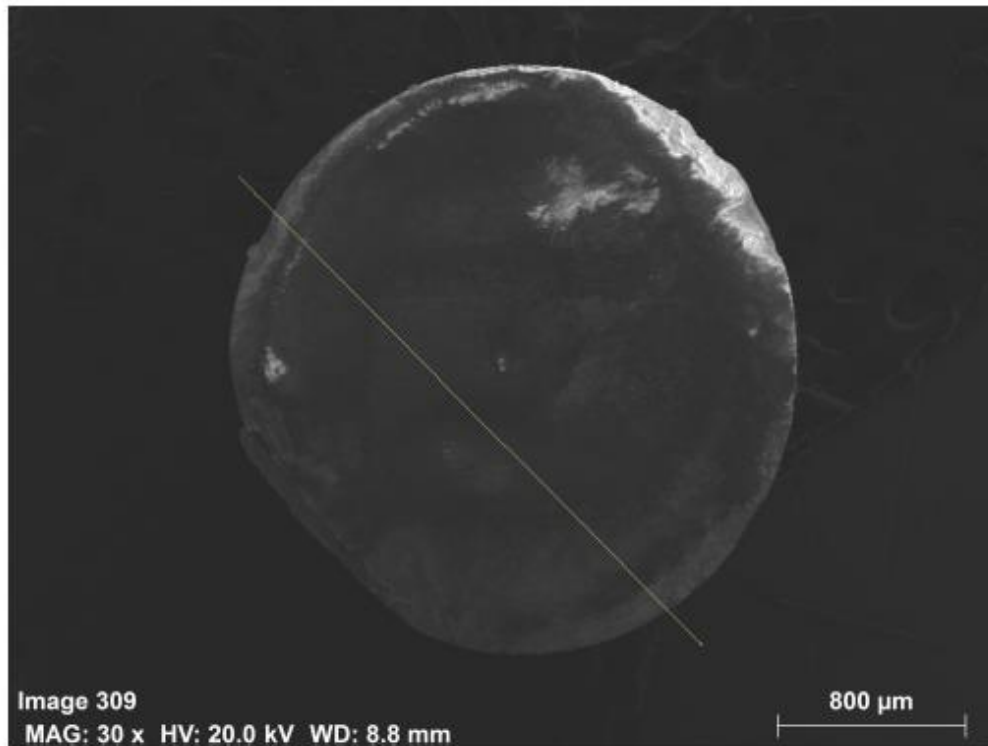
Some of chloride ions and sodium ions still present after washing for 90 minutes. Lower calcium ion concentration than in a bead (washed for 15 minutes).



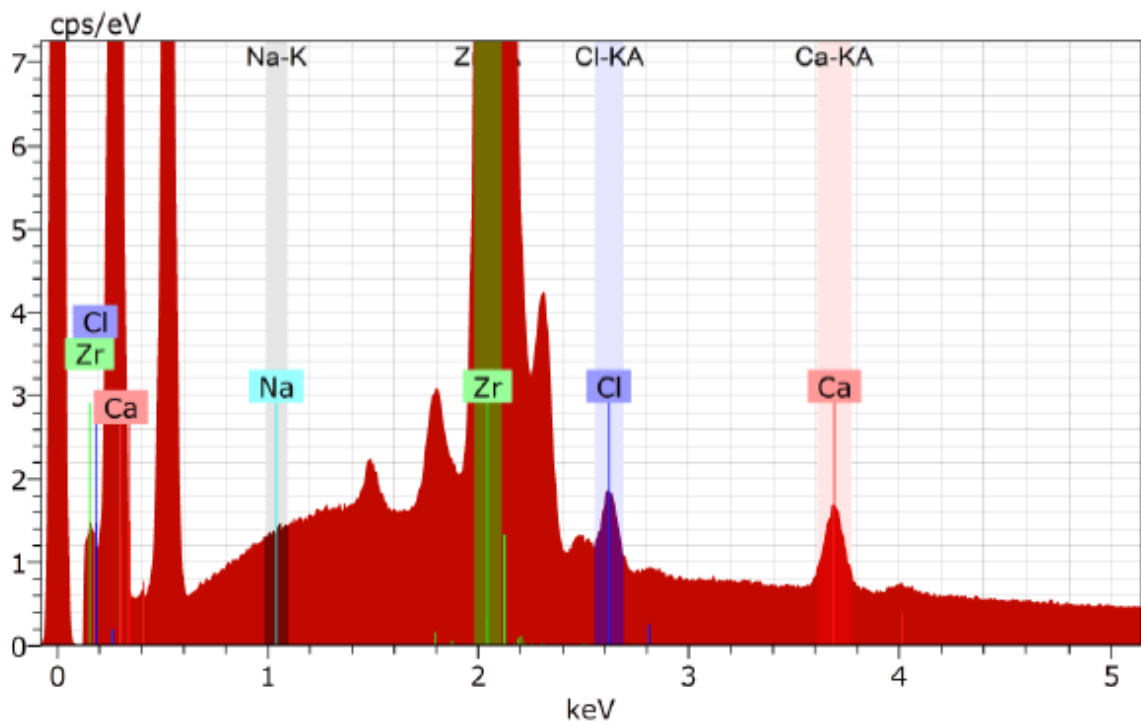
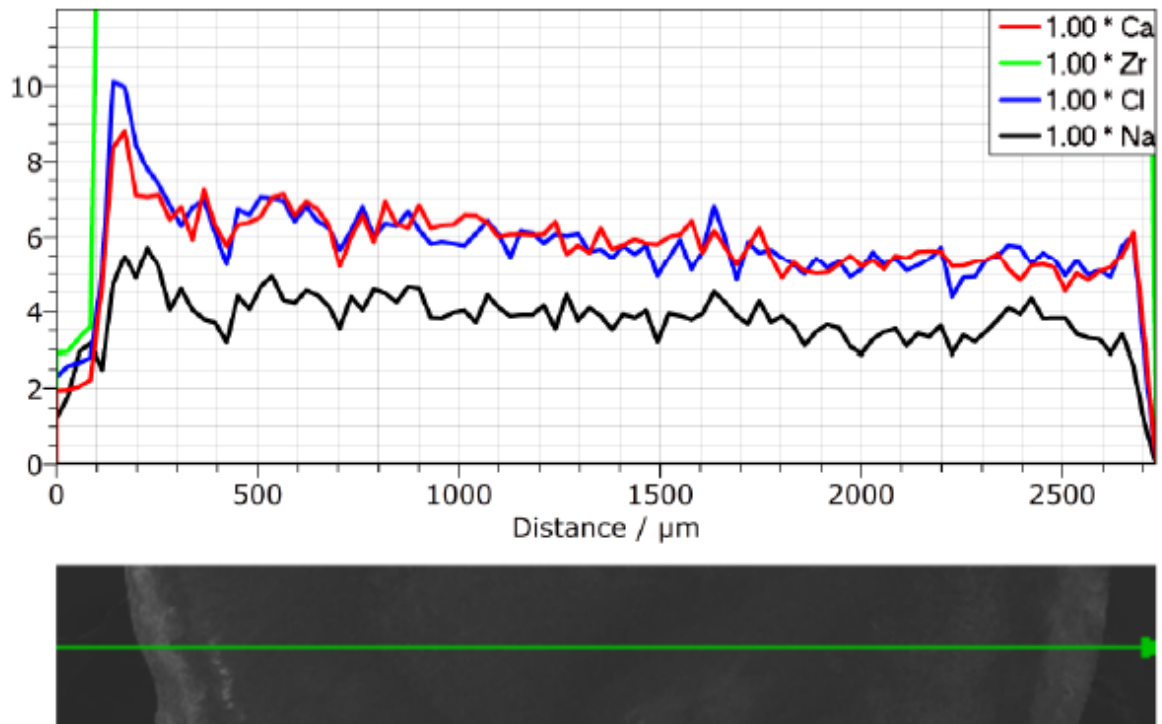
A bead washed for 15 minutes.



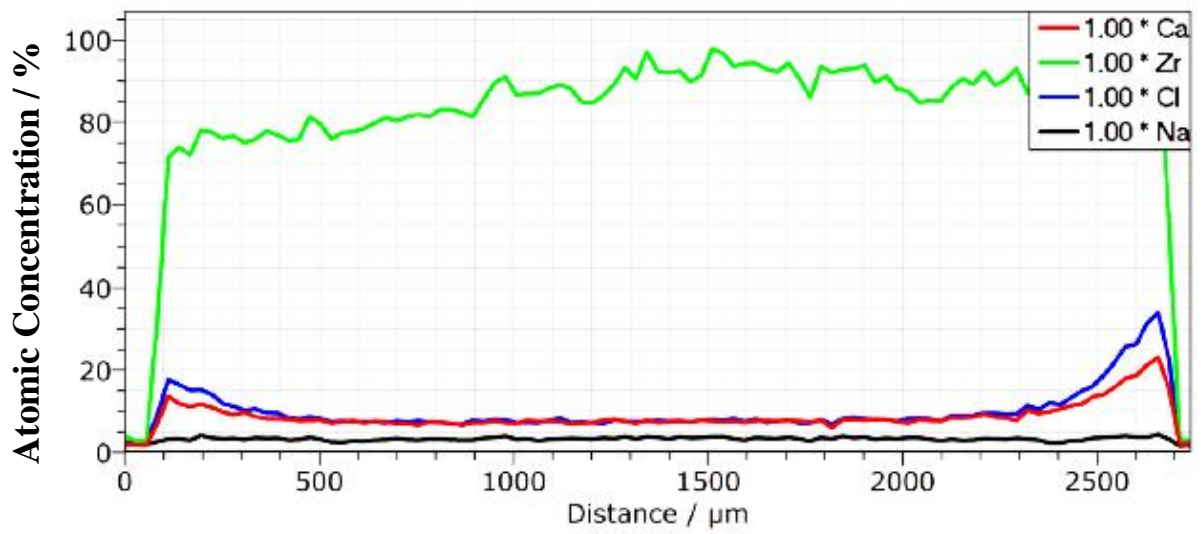
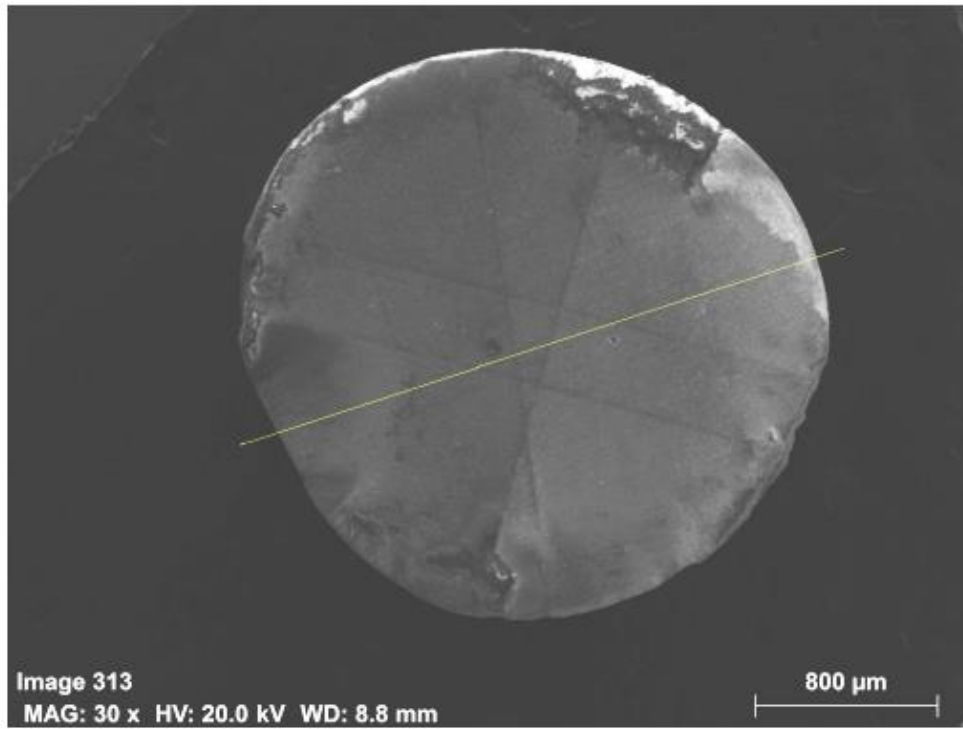
No signs of accumulated Ca and Cl ions at the edge as observed in a bead washed for 10 minutes.



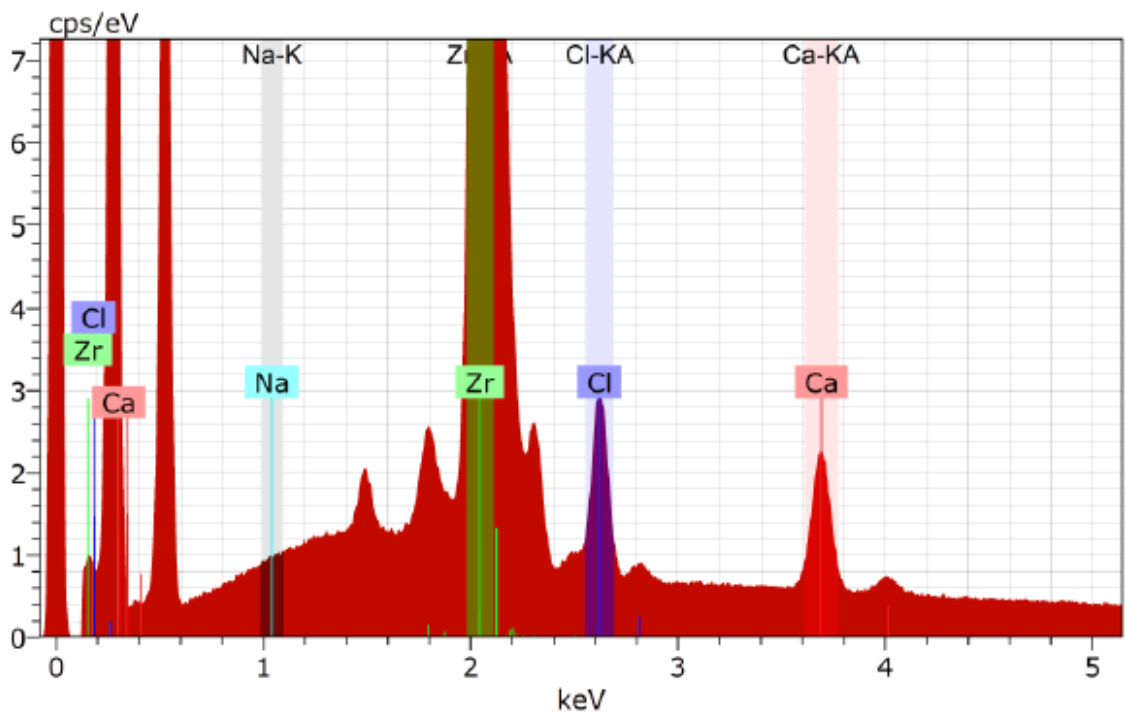
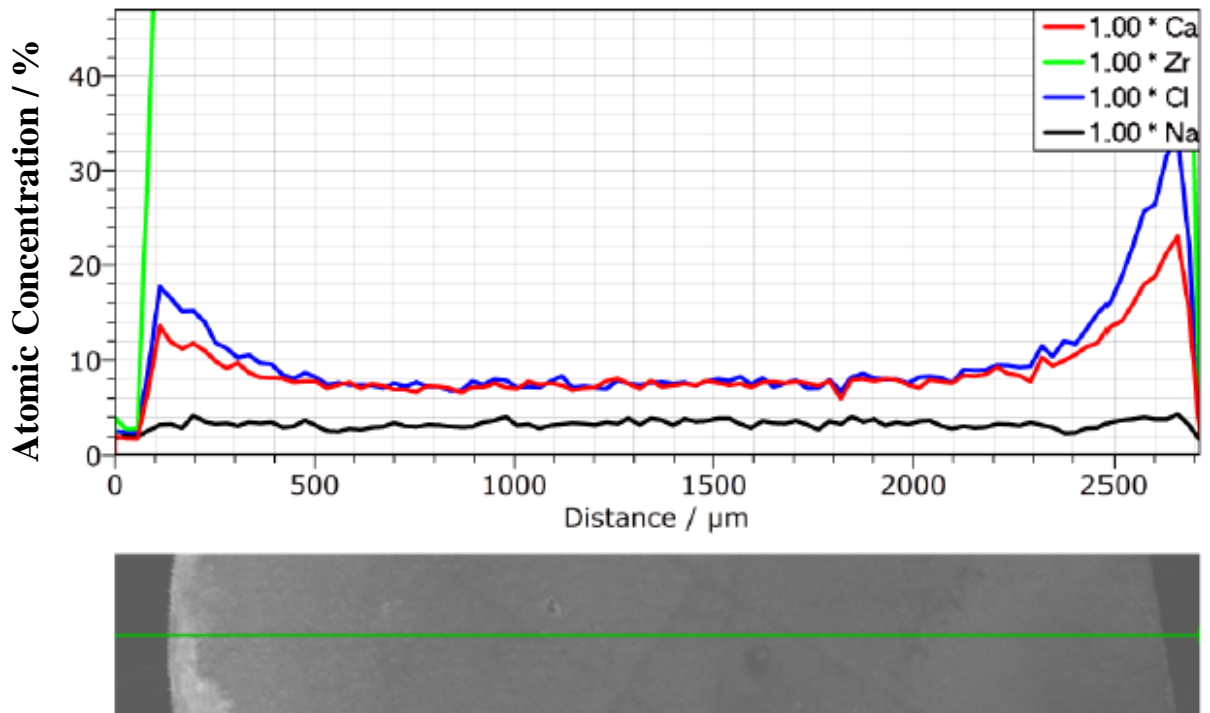
A bead washed for 10 minutes



The concentrations of Ca and Cl ions are slightly higher at the edge whereas the Zr concentration is more or less constant. This indicates the accumulation of Ca and Cl ions.

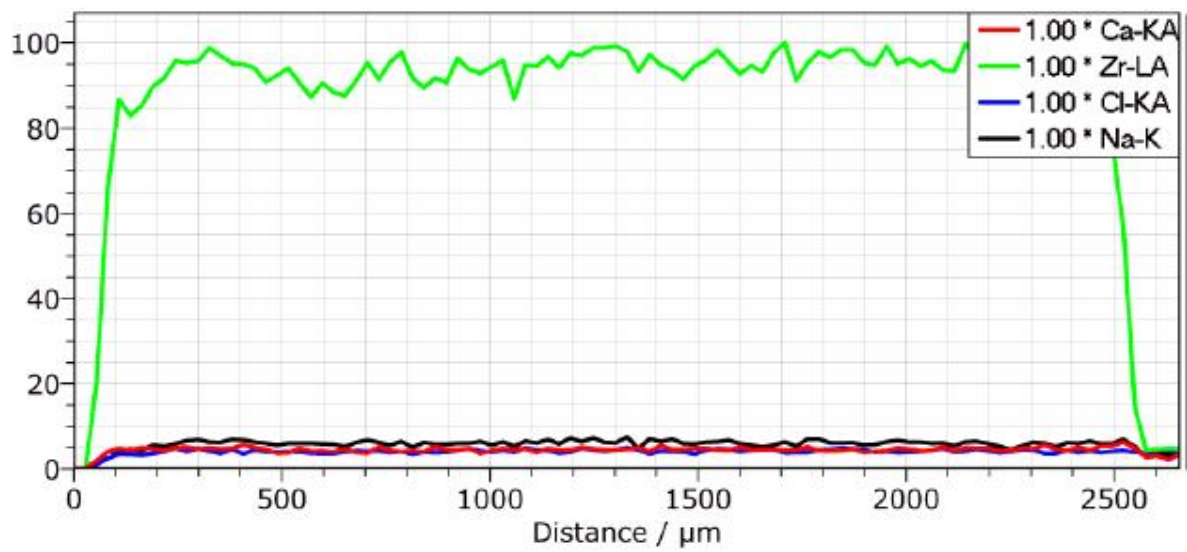
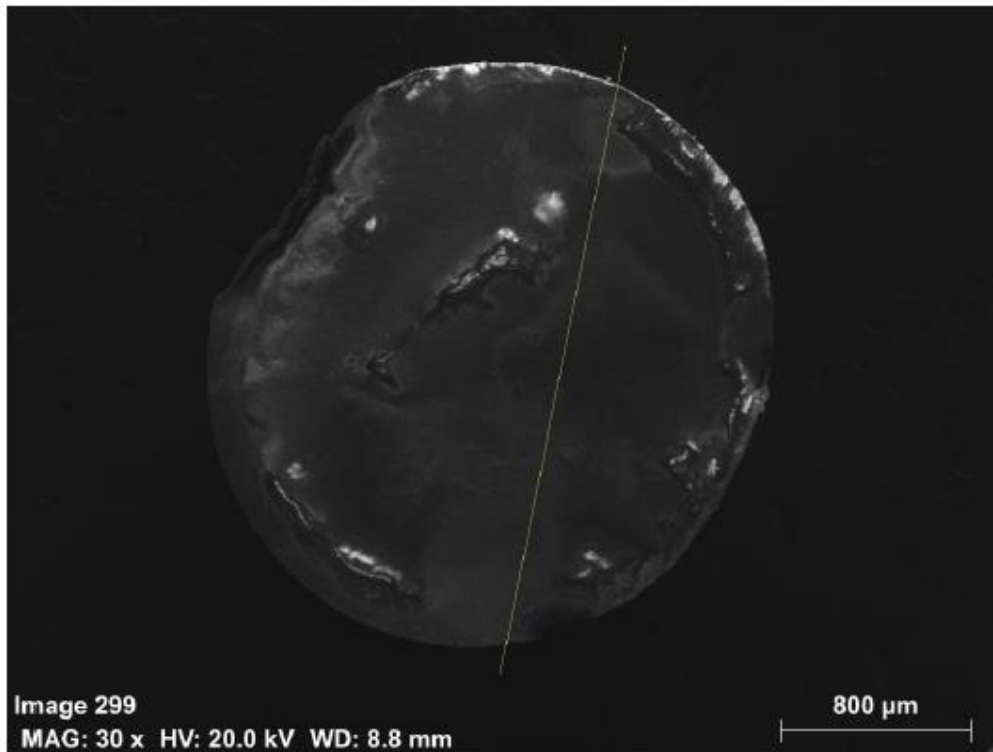


Non-washed bead.

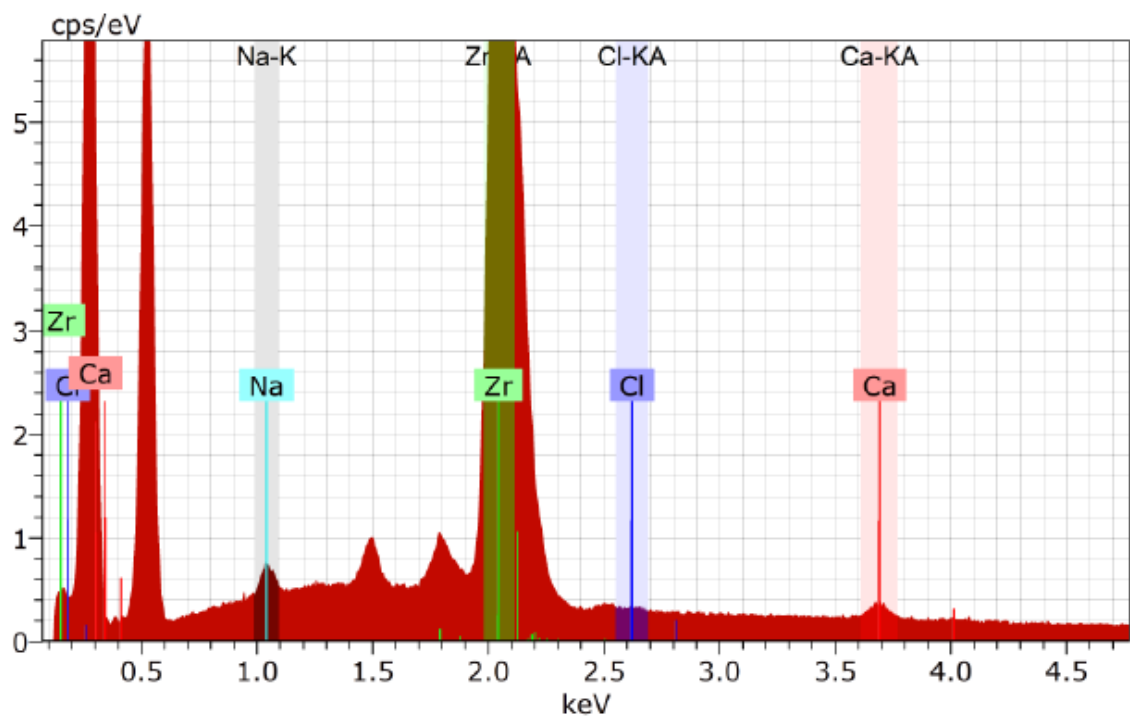
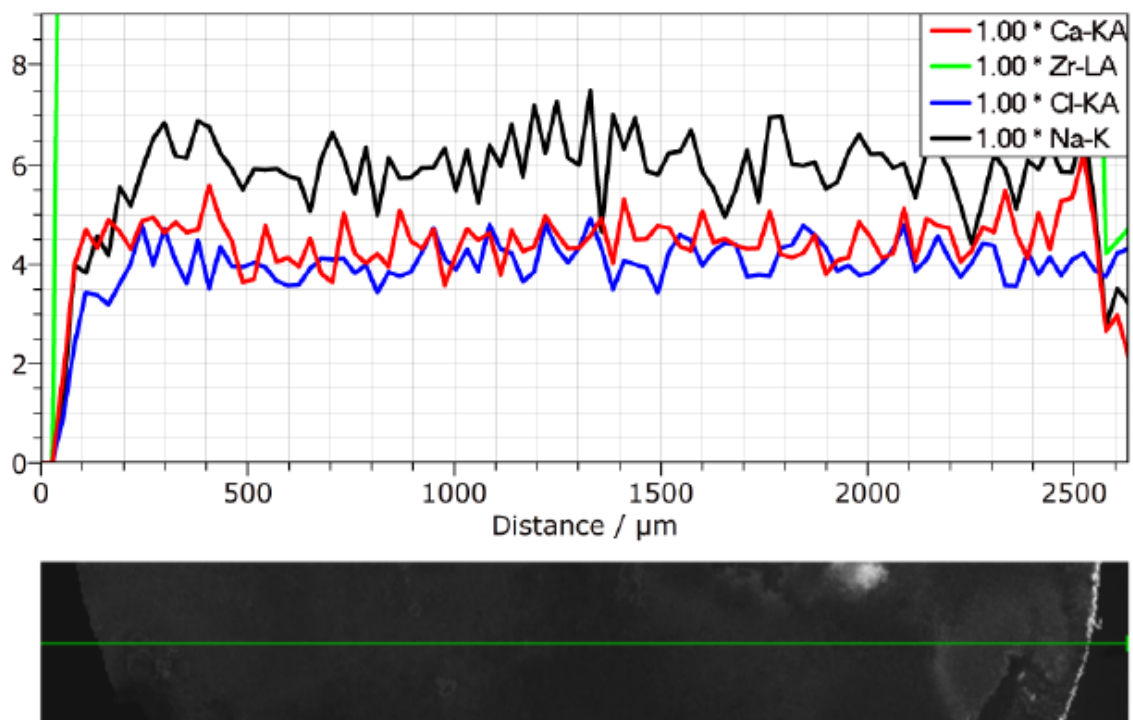


Significantly higher concentrations of calcium and chloride ions. Accumulated Ca and Cl ions at the outer layer is observed.

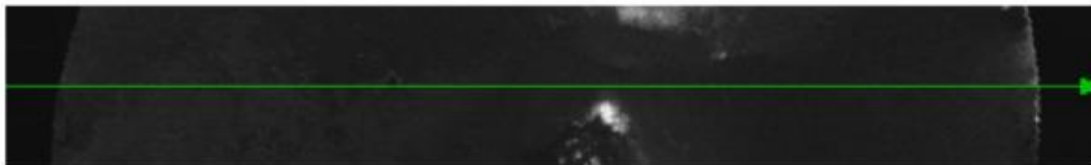
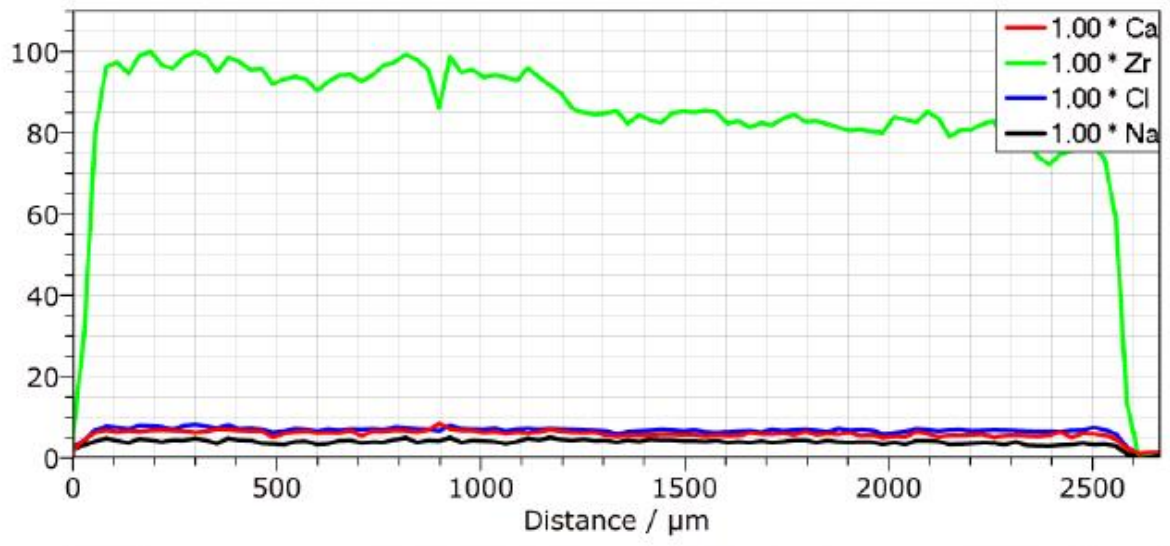
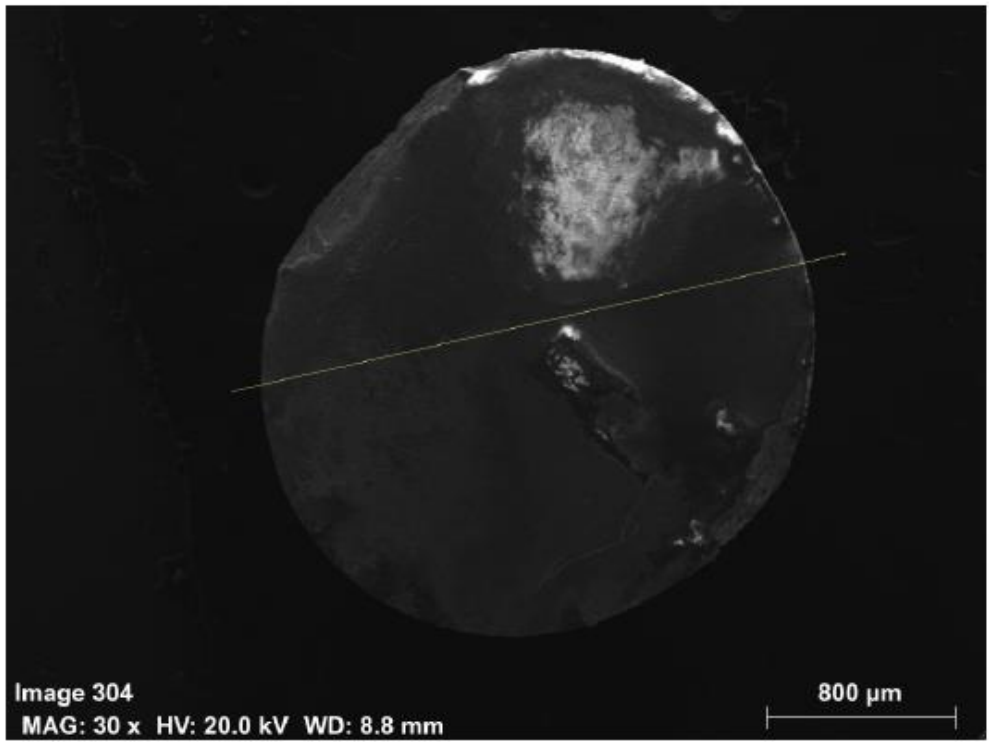
7.5.2. EDX on samples with varying gelation time



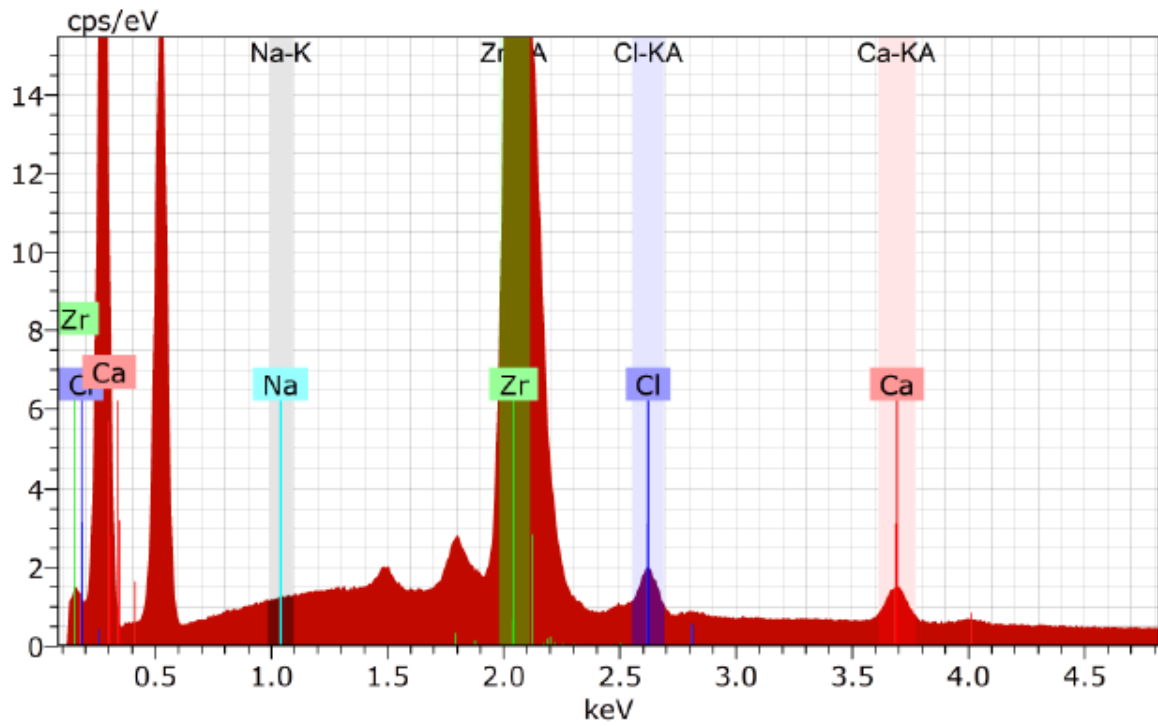
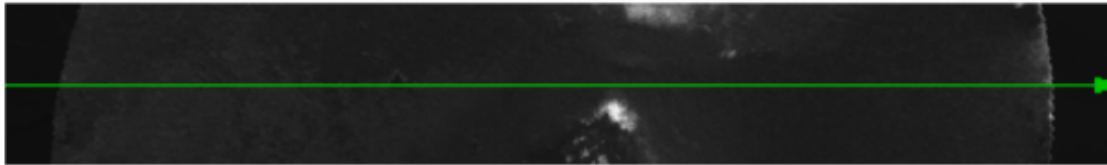
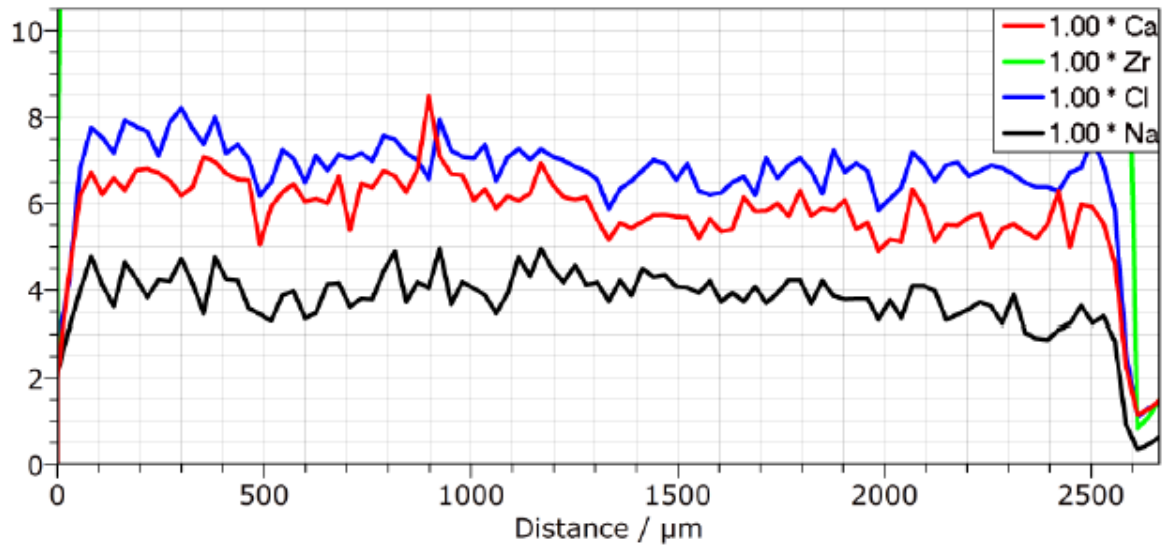
Gelation for 3 minutes.



The atomic concentration of sodium atoms is higher than calcium and chloride ions. This indicates that alginic acids are not saturated by calcium ions yet at this point.

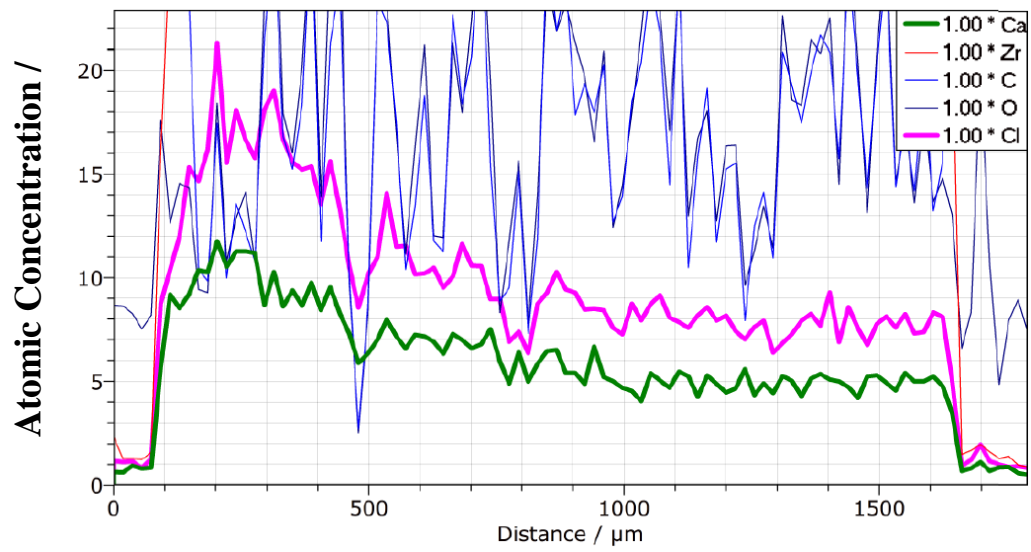
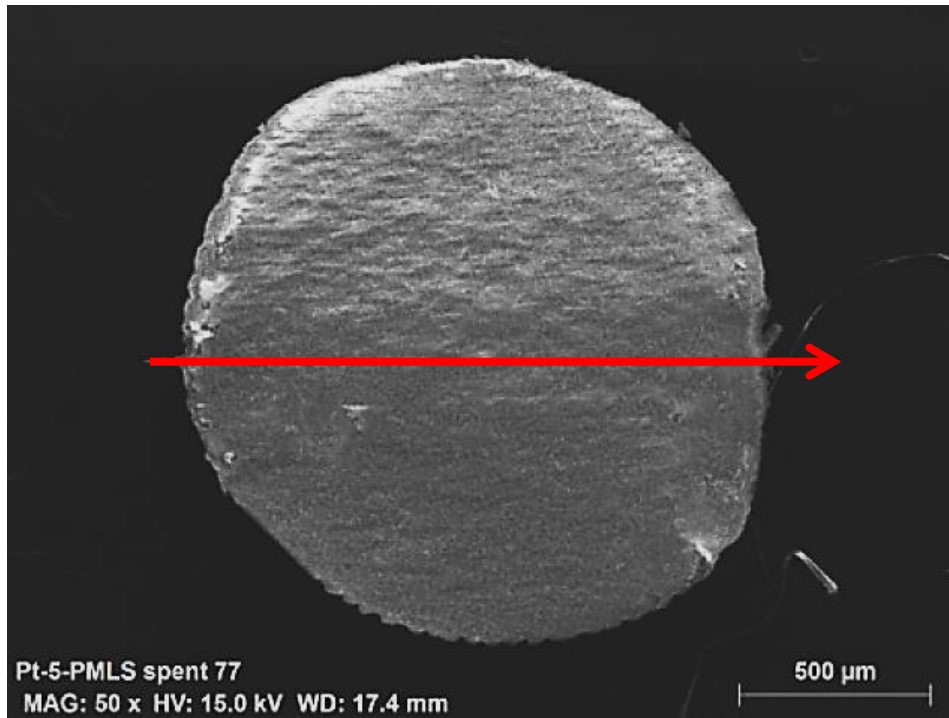


Gelation for 15 minutes

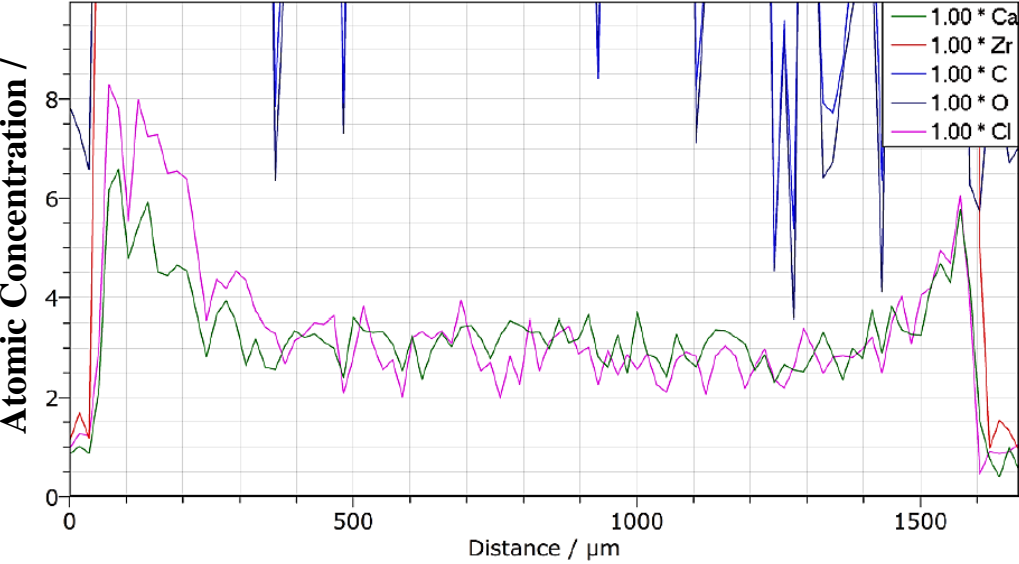
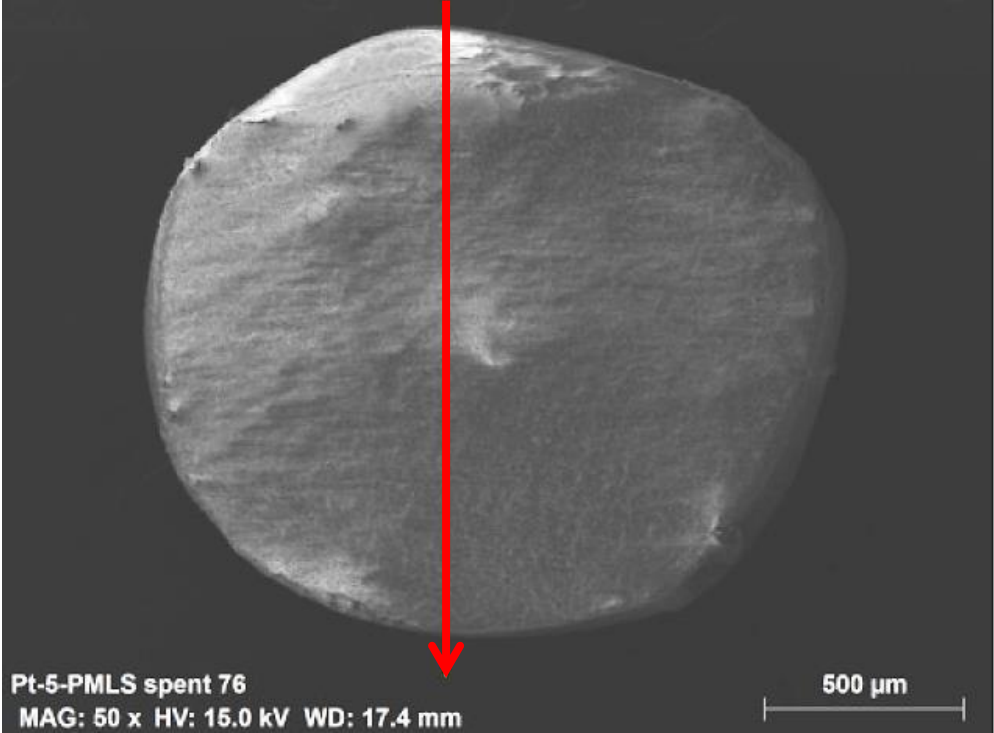


Higher atomic concentrations of calcium and chloride atoms than sodium atoms.

3



CaCl₂ samples were examined because chlorine ion is a heavier element than nitrogen, thus easier to quantize.



7.6. Calculation of Isostatic Heat of Adsorption

The isosteric heat of CO₂ adsorption (Q_{st}) is calculated to assess the strength of the interaction between CO₂ and the formulated UiO-66 samples.

In accordance with the linearized Clausius-Clapeyron equation, the isosteric heat of CO₂ adsorption, Q_{st} , was obtained by extracting the slope from a plot of $\ln(p)$ against $\frac{1}{T}$:

$$\ln(p) = \frac{Q_{st}}{R} \cdot \left(\frac{1}{T}\right) + C$$

Where:

R is the gas constant (8.314462 JK⁻¹mol⁻¹).

T is the absolute temperature at which the isotherm was obtained. Herein, the isotherms were obtained at three different temperatures (303.15 K, 313.15 K and 343.15 K). There are 3 data points in each linear plot.

p is the pressure (in mbar) at which the CO₂ adsorption loading N (in mmol·g⁻¹) is reached, according to the following rearrangement of the Langmuir adsorption model:

$$p = \left(\frac{N}{kN_{sat}}\right) - kN$$

Where N_{sat} and k were extracted from the isotherms fits

Inserting the above into the Clausius-Clapeyron equations allows one to calculate the evolution of Q_{st} as a function of CO₂ loading (N):

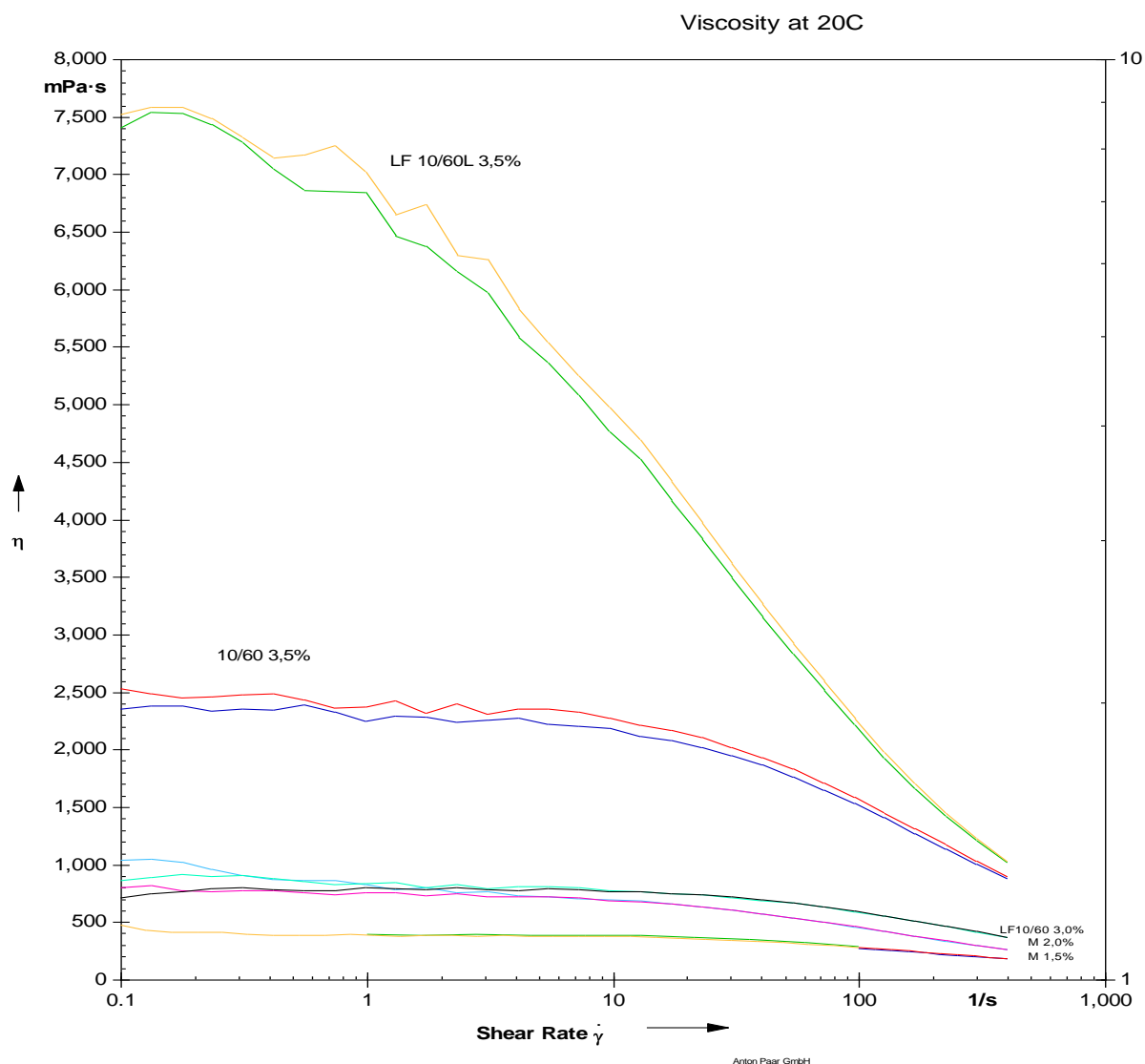
$$\ln\left(\left(\frac{N}{kN_{sat}}\right) - kN\right) = \frac{Q_{st}}{R} \cdot \left(\frac{1}{T}\right) + C$$

The reported Q_{st} values were calculated at a CO₂ loading (N) of 0 mmol·g⁻¹.

7.7. Sample Overview

Attached as a separate pdf file.

7.8. Viscosity Measurement of Alginates



It appeared that solutions were neither Newtonian nor non-Newtonian. These solutions were tested with different cutting intervals and viscosity of all of them plunged when the shear rate was approaching 400 s^{-1} . All samples were run twice consecutively. Initially, dissolved alginates were thought to be thixotropic, but by running it again right after the first run, similar pattern was observed; the viscosity decreased with increasing shear rate. The samples appear to be shear thinning.



Figure 62: Highly viscous alginate solution due to high alginate concentration makes it harder to produce MOF-beads